

# **Momentum and Mass Transfer from Atmosphere to Rough Surfaces: Improvement on Drag Partition Theory and Dry Deposition Model**

Inaugural-Dissertation  
zur  
Erlangung des Doktorgrades  
der Mathematisch-Naturwissenschaftlichen Fakultät  
der Universität zu Köln

vorgelegt von  
Zhuoqun Li  
aus Hubei, China  
2014

Berichterstatter: Prof. Dr. Y. Shao  
Prof. Dr. M. Kerschgens  
Tag der mündlichen Prüfung: 14. Jan. 2015

# Abstract

The transfers of momentum and mass from the atmosphere to rough surfaces are fundamental scientific problems for meteorology, environment and industry. The transfer of momentum is crucial for the transfer of mass, heat, etc., in the boundary layer. The mass transfer, e.g., dust dry deposition, is a key process of the dust cycle. Both processes are closely related, but not well understood, particularly on rough surfaces or in unsteady conditions. Momentum and mass flux have been found to be associated with the geometric dimensions of the wake behind roughness elements. The dimensions of these wakes can be determined by the geometry of the obstacles on rough surfaces and wind speed. The objective of this thesis is to improve the theories of momentum transfer and drag partition between roughness elements and the exposed underlying surface, as well as the parameterization of particle deposition by means of numerical simulations of the air flow and dust flux over rough surfaces.

To investigate the transfer of momentum and mass to rough surfaces, both two-dimensional Reynold Stress Model (2D RSM) simulations and three-dimensional Large Eddy Simulations (3D LES) are carried out. A rough surface in the simulation refers to a flat surface with regularly distributed identical roughness elements. The wind profile, surface drag, and the geometric dimensions of the wake are determined from the simulation results. Friction velocity ( $u_*$ ) and a friction coefficient ( $u_*/u_h$ ) are estimated as functions of roughness density ( $\lambda$ ), threshold roughness density ( $\lambda_a$ ), and wind speed ( $u_r$ ). The dimensions of the wake, which influence the drag and are controlled by wind speed, are subject to the roughness density and the dimensions of the elements. Hence, it is important to repeat the numerical experiments for various element heights ( $h$ ), roughness densities and wind speeds. To study dust dry deposition, particle injections are included in the 3D simulation. It allows for particle tracking in the turbulent flow; thereby, the deposition velocity can be determined under different wind speeds, particle diameters and roughness densities.

The 2D simulation consists of 260 runs on 13 distinctive surfaces ( $1/30 < \lambda < 2/3$ ,  $h = 5$ , 7.5 and 10 mm) at 20 different wind speeds (1 - 20 ms<sup>-1</sup>). The purpose of the 2D simulation is to analyze the geometric dimensions of the wake in the absence of spanwise disturbance. 2D

## Abstract

---

simulations limit the possible mutual sheltering of elements in the streamwise direction. Without these disturbances, the length of the wake behind isolated element is presented as a function of wind speed. The height-to-length ratio of the wake ( $\lambda_w = h_w/L_w$ ) is analyzed and found to be independent of element height. When the wake is a full wake,  $\lambda_w$  is also independent from wind speed, and  $\lambda_w = \lambda_a$ . The relation among the dimensions of roughness elements, the wake and the drag are estimated.

A physical model of drag and drag partition is proposed, based on a resistance method. The drag and drag partitions are expressed as functions of  $\lambda$ , and  $\lambda_a$ , without empirical parameters. The estimation of the new model are analyzed and compared to classical experimental results and a 3D simulations results. The 3D simulation for air flow over rough surface are conducted for 11 distinctive surfaces ( $1/30 < \lambda < 1/2$ ) with identical elements of 10 mm height, at 6 different wind speeds ( $1-25 \text{ ms}^{-1}$ ). In the resistance method for the momentum flux, the resistances of the element ( $R_r$ ), and the underlying surface ( $R_s$ ) in the canyon layer are respectively determined. The threshold roughness density ( $\lambda_a$ ) is introduced in the expressions of resistances. This threshold is defined as the roughness density of the surface which has equal momentum flux on the element and on the underlying surface. This threshold can be determined by the length of the wake ( $L_w$ ) on rough surfaces and helps to distinguish elements of different length-to-height ratios ( $b/h$ ). New expressions of friction velocity and drag partitions ( $\tau_r + \tau_s$ ) are derived without any empirical parameter. The friction coefficient is determined empirically. Classical wind tunnel data of drag for rough surfaces with various roughness densities, and results from the 3D simulation are successfully reproduced, and in response to different length-to-height ratios of roughness elements. Thus, the new expressions of drag and drag partition on rough surfaces are validated.

The discrepancy between the estimation of existing dry deposition model and field measurements reaches 2 orders of magnitude. In the existing models of dust dry deposition, the rough surfaces are treated as a single cylinder. Sensitivity tests show that the possible uncertainty on the deposition velocity generated by this method can reach 337%. To investigate dust dry deposition in more details, 3D simulations of deposition on rough surfaces are conducted and 15 groups of particles with different diameters ( $0.1 \mu\text{m} < d_p < 10 \mu\text{m}$ ) are injected into the simulation domain. Deposition velocity is deduced by counting trapped particle on the surfaces, in fully developed flow. Regression analysis is applied to fit the deposition velocity as functions of wind speed, roughness density or particle size from simulation results. The resulting prediction of the deposition velocity is consistent with field measurements and explains the discrepancies among existing field measurements and previous model estimations.

The measurement of deposition process in the natural flow is also studied. The aim of this part is to examine the influence of unsteady dust flux on the measurement of deposition velocity and errors caused by field measuring method. An existing vertical dispersion framework is introduced to simulate the one-dimensional deposition velocity. Intermittent dust flux data from a well-known field measurement during a dust event, as input data. The resulting estimations of deposition velocity are consistent with field measurements. The understanding of momentum and mass transfer on rough surfaces could thereby be improved.

# Zusammenfassung

Der Impuls- und Massenfluss zwischen Atmosphäre und Bodenoberfläche stellt ein wichtiges wissenschaftliches Problem dar, das von entscheidender Bedeutung für Meteorologie, Umwelt und Industrie ist. Der Transfer von Impuls ist entscheidend für den Transport von Masse, Wärme, etc. in der Grenzschicht und der Transfer von Masse, z.B. die trockene Deposition von Staubpartikeln, ist ein Schlüsselprozess des Staubkreislaufs. Beide Prozesse sind eng miteinander verknüpft, aber insbesondere auf rauen Oberflächen oder in ungleichförmigen Strömungsbedingungen noch nicht gut verstanden. Impuls- und Massenflüsse konnten mit den geometrischen Dimensionen der Nachlaufströmung hinter Rauigkeitselementen in Zusammenhang gebracht werden. Die Dimension dieser Nachlaufströmung hängt mit der Geometrie der rauen Oberfläche sowie der Windgeschwindigkeit zusammen. Das Ziel dieser Arbeit ist es, die Theorien zu Impulsfluss und dessen Partitionierung zwischen Rauigkeitselementen und exponierten Oberflächen sowie die Parametrisierung der Partikeldeposition mit Hilfe von numerischen Simulationen der Strömung und des Staubflusses auf rauen Oberflächen zu verbessern.

Um den Transport von Impuls und Masse auf raue Oberflächen zu untersuchen, werden sowohl zweidimensionale Simulationen mit dem sogenannten „Reynolds Stress Model“ (2D RSM) als auch dreidimensionale „Large-Eddy“ Simulationen (3D LES) durchgeführt. Die Bezeichnung „raue Oberfläche“ bezieht sich in den Simulationen auf eine flache Oberfläche auf der identische Rauigkeitselemente gleichmäßig verteilt sind. Das Windprofil, die Bodenschubspannung und die geometrischen Dimensionen der Nachlaufströmung werden an Hand der Simulationsergebnisse bestimmt. Die Schubspannungsgeschwindigkeit ( $u_*$ ) und der Schubspannungskoeffizient ( $u_*/u_h$ ) werden in Abhängigkeit von Rauigkeitsdichte ( $\lambda$ ), Grenzwert der Rauigkeitsdichte ( $\lambda_a$ ) und Windgeschwindigkeit ( $u_r$ ) bestimmt. Die Dimensionen der Nachlaufströmung hängen von der Windgeschwindigkeit ab und beeinflussen

die Schubspannung. Sie werden durch die Rauigkeitsdichte sowie Form und Größe der Rauigkeitslemente bestimmt. Daher ist es wichtig die numerischen Experimente für unterschiedliche Elementhöhen ( $h$ ), Rauigkeitsdichten und Windgeschwindigkeiten zu wiederholen. Zur Untersuchung der trockenen Staubdeposition wird die 3D Simulation um eine Partikelinjektion erweitert. Dies ermöglicht die Verfolgung der Partikelbahn in der turbulenten Strömung. Dadurch kann die Depositionsgeschwindigkeit für verschiedene Windgeschwindigkeiten, Partikeldurchmesser und Rauigkeitsdichten bestimmt werden.

Die 2D Simulation besteht aus 260 Läufen für 13 bestimmte Oberflächen ( $1/30 < \lambda < 2/3$ ,  $h = 5$ , 7.5 und 10 cm) bei 20 Windgeschwindigkeiten (1 - 20 m/s). Der Zweck der 2D Simulation ist die Analyse der geometrischen Dimensionen der Nachlaufströmung in Abwesenheit einer Störung quer zur Strömungsrichtung. 2D Simulationen begrenzen die gegenseitige Abschirmung der Rauigkeitslemente in Strömungsrichtung. Ohne diese Störungen kann die Größe der Nachlaufströmung als Funktion der Windgeschwindigkeit beschrieben werden. Die Analyse des Verhältnisses zwischen Höhe und Länge der Nachlaufströmung ( $\lambda_w = l/L_w$ ) zeigt keine Abhängigkeit zur Höhe der Rauigkeitelemente und der Windgeschwindigkeit. Und  $\lambda_w = \lambda_a$ . Der Zusammenhang zwischen den Dimensionen der Bodenoberfläche, der Nachlaufströmung und der Schubspannung wird bestimmt.

Ein physikalisches Modell für Schubspannung und Schubspannungspartitionierung wird basierend auf einer Widerstandsmethode erstellt. Schubspannung und Schubspannungspartitionierung werden als Funktionen von  $\lambda$  und  $\lambda_a$  ohne empirische Parameter dargestellt. Die Ergebnisse des neuen Modells werden analysiert und verglichen mit denen klassischer Experimente und eines 3D Simulationsmodells. Die 3D-Simulationen werden für 11 Oberflächen ( $1/30 < \lambda < 1/2$ ) mit identischen Elementen von 10 mm Höhe für 6 Windgeschwindigkeiten (1 - 25 m/s) durchgeführt. In der Widerstandsmethode für den Impulsfluss werden die Widerstände des Elementes ( $R_e$ ) und der Bodenoberfläche ( $R_s$ ) in den Elementzwischenräumen bestimmt. Der Grenzwert der Rauigkeitsdichte ( $\lambda_a$ ) wird zur Beschreibung der genannten Widerstände genutzt. Der Grenzwert ist definiert als die Rauigkeitsdichte des Bodens, bei dem der gleiche Impulsfluss auf das Rauigkeitelement und die Bodenoberfläche vorherrscht. Der Grenzwert kann durch die Länge der Nachlaufströmung ( $L_w$ ) auf rauen Oberflächen bestimmt werden und dient der Unterscheidung von Elementen mit unterschiedlichem Verhältnis Länge/Höhe. Neue Ausdrücke für den Schubspannungskoeffizienten und die Schubspannungspartitionierung ( $\tau_r + \tau_s$ ) konnten ohne empirische Parameter bestimmt werden. Der Reibungskoeffizient wurde empirisch bestimmt. So konnten klassische Windtunneldaten für raue Oberflächen mit unterschiedlichen Rauigkeitsdichten und verschiedenen Elementlänge/-höhe Verhältnissen erfolgreich reproduziert werden. Dadurch konnten die neuen Ausdrücke für Schubspannung und Schubspannungsunterteilung auf rauen Oberflächen validiert werden.

Die Diskrepanz zwischen bestehenden Depositionsmodellen und Feldmessungen beträgt bis zu zwei Größenordnungen. In existierenden Modellen der trockenen Deposition werden rauere Oberflächen als separate Zylinder behandelt. Sensitivitätstests zeigen, dass die durch diese Methode bestimmte Depositionsgeschwindigkeit mit einer Unsicherheit von bis zu 337% behaftet ist. Zur detaillierteren Untersuchung der trockenen Deposition werden in dieser Studie 3D Simulationen der Deposition auf rauen Oberflächen durchgeführt. Hierzu werden 15

Gruppen von Partikeln mit unterschiedlichen Durchmessern ( $0.1\mu\text{m} < d_p < 10\mu\text{m}$ ) in die Simulationsdomäne injiziert. Rückschlüsse auf die Depositionsgeschwindigkeit können mit Hilfe der Anzahl der Partikel gezogen werden, die sich auf der Oberfläche bei vollentwickelter Strömung niederschlagen. Die Depositionsgeschwindigkeit kann schließlich durch Regression als Funktion von Windgeschwindigkeit, Rauigkeitsdichte oder Partikelgröße an Hand der Simulationsergebnisse bestimmt werden. Die daraus folgende Vorhersage der Depositionsgeschwindigkeit ist konsistent mit Feldmessungen und erklärt den Unterschied zwischen Beobachtungen und Ergebnissen bestehender Modelle.

Der Einfluss der natürlichen Strömungen auf den Depositionsprozess wird ebenfalls untersucht. Ziel davon ist es den Einfluss des unstetigen Staubflusses auf die gemessene Depositionsgeschwindigkeit sowie Fehler durch die Methode bei Feldmessungen zu prüfen. Hierzu wird eine existierende Beschreibung der vertikalen Dispersion zur Simulation der eindimensionalen Depositionsgeschwindigkeit genutzt. Input hierfür ist der intermittierende Staubfluss eines weitbekannten Feldexperimentes während eines Staubereignisses. Die damit geschätzte Depositionsgeschwindigkeit ist konsistent mit den Feldmessungen. Somit konnte das Verständnis von Impuls- und Massenfluss auf rauen Oberflächen verbessert werden.



# 1. Table of Contents

<b>Abstract .....</b>	<b>i</b>
<b>Zusammenfassung .....</b>	<b>i</b>
<b>1. Introduction .....</b>	<b>1</b>
1.1 Thesis rationale .....	1
1.2 Existing theories on airflow over rough surfaces .....	2
1.2.1 Surface parameters for a geometric method.....	2
1.2.2 Definition of drag and drag partition .....	4
1.2.3 Wind profiles over smooth and rough surfaces.....	6
1.2.4 The wake behind roughness elements.....	8
1.3 Existing theories on dry deposition.....	10
1.3.1 Definition of deposition velocity .....	11
1.3.2 Dry deposition models .....	12
1.3.3 Applications of dry deposition models .....	14
1.3.4 A two layer model of dry deposition .....	15
1.4 Summary of scientific problems .....	16
1.5 Thesis outline .....	17
<b>2. The wakes on rough surfaces .....</b>	<b>21</b>
2.1 Introduction .....	21
2.2 Setup of the 2D Simulation .....	22
2.3 2D Flow over isolated elements .....	24
2.3.1 Results of 2D flow over isolated elements.....	24

2.3.2 Discussion on the types of wakes .....	25
2.3.3 Result on the length of wakes .....	27
2.3.4 Discussion on the length of wakes .....	29
2.4 2D Flow over regularly-arranged rough surfaces.....	30
2.4.1 Results of 2D flow over rough surfaces.....	30
2.4.2 The model of wake on rough surfaces .....	31
2.5 Parameters of 2D air flow over rough surface.....	33
2.5.1 Friction coefficient.....	33
2.5.2 Drag partition $\tau_r/\tau$ .....	35
2.5.3 Wind profile over rough surfaces .....	36
2.6 Conclusion .....	41
<b>3. Drag on rough surfaces .....</b>	<b>43</b>
3.1 Introduction.....	43
3.2 Existing theory of drag on rough surfaces.....	44
3.3 The new drag and drag partition theory .....	47
3.3.1 Total Resistance to the momentum flux .....	47
3.3.2 Resistances of $R_f$ and $R_s$ to the momentum flux .....	48
3.3.3 Determine the resistances .....	49
3.3.4 The new expression of drag and drag partitions .....	50
3.4 Setup of 3D simulation of flows over ridges.....	52
3.5 Results and discussion.....	53
3.5.1 3D simulation results of flow over rough surfaces .....	53
3.5.2 Discussion on 3D simulation results .....	58
3.6 Parameters of wind profile in 3D simulation .....	62
3.7 Conclusion .....	64
<b>4. Deposition on rough surfaces.....</b>	<b>67</b>
4.1 Modeling particle deposition.....	67
4.2 Definition of deposition velocity in the simulation .....	68
4.3 Sensitivity tests of parameters in deposition models.....	68
4.3.1 Critical parameters for dry deposition .....	68
4.3.2 A sensitivity test of $r_b$ .....	69
4.3.3 A sensitivity test of $d_c$ .....	70
4.3.4 Sensitivity of the deposition velocity over high canopies.....	70
4.4 Setup of 3D Simulation of particle laden flow .....	72
4.5 Results and discussion.....	73
4.5.1 Steady state particle flux .....	73
4.5.2 Results of Deposition Velocity .....	74

---

## Table of contents

4.5.3 Estimations versus field measurements .....	81
4.6 Conclusion .....	83
<b>5. Deposition in natural conditions.....</b>	<b>85</b>
5.1 Intermittent deposition process .....	85
5.2 A framework of the vertical dispersion.....	86
5.3 Deposition in the intermittent condition.....	88
5.3.1 Experimental data of Gallagher (1997).....	88
5.3.2 Numerical experiment.....	89
5.3.3 Deposition velocity in natural condition.....	90
5.4 Discussion and Conclusion .....	92
<b>6. Conclusion and recommendations.....</b>	<b>93</b>
6.1 The wake and the parameter of $\lambda_a$ .....	93
6.2 The new drag and drag partition theory .....	94
6.3 Deposition velocity on rough surfaces .....	96
6.4 The momentum flux and the mass flux .....	97
6.5 Relationship between the 2D and 3D simulation .....	97
6.6 Outlook .....	98
<b>References .....</b>	<b>I</b>
<b>Appendix .....</b>	<b>X</b>
<b>Acknowledgements .....</b>	<b>XV</b>
<b>Erklärung.....</b>	<b>XVI</b>



# 1. Introduction

## 1.1 Thesis rationale

Momentum and mass transfer from the atmosphere to rough surfaces are fundamental scientific problems of meteorological, environmental and industrial importance (Davies, 2012; Garratt, 1977; Welty et al., 2009). In neutral conditions, these processes can be described as a flux through three layers, i.e., the inertial layer, the roughness layer and the canopy layer<sup>1</sup>. (Owen & Thomson, 1963; Prandtl, 1963; Slinn & Slinn, 1980; Thom, 1972a). The resistances to momentum and mass transfers through these layers are dependent on the geometry of the surface roughness (Owen & Thomson, 1963; Raupach et al., 1980; Shao & Yang, 2005; Thom, 1967; Wooding et al., 1973). The resistance to momentum transfer is related to that of mass transfer and has been shown in laboratory experiments (Chamberlain, 2012; Owen & Thomson, 1963).

Momentum transfer from the atmosphere to rough surfaces can be quantified by surface drag (Schlichting & Gersten, 2000). The surface drag is usually represented by shear stress ( $\tau$ ), friction velocity ( $u_*$ ) or drag and friction coefficient ( $C_d = u_*^2/u_h^2$ ,  $c_d = u_*/u_h$ ), depending on their applications. Drag on a flat smooth surface is well understood. Placing roughness elements on a smooth surface generally increases the total drag (Cheng et al., 2007; Raupach, 1992; Shao & Yang, 2008). For certain types of rough surfaces, when the density of roughness elements ( $\lambda$ ) on a rough surface exceeds a certain threshold ( $\lambda_a$ ), the surface turns from a sparse surface ( $\lambda < \lambda_a$ ) to a dense surface ( $\lambda > \lambda_a$ )<sup>2</sup>, and the drag starts to decrease due to mutual sheltering of the

---

<sup>1</sup> The canopy layer is also known as the canopy layer.

<sup>2</sup>  $\lambda$  is defined as the roughness density, as  $\lambda = b/l$  for all surfaces. It equals to the square root of frontal area index when the length and height of element are equal, i.e.,  $b = h$ .

$\lambda_a$  is (a) The threshold roughness density, which distinguishes dense and sparse surfaces (Chap. 2); (b) The roughness density of the surface with  $F_r(\lambda_a) = F_s(\lambda_a)$ . (Chap. 3); (c) The height-to-length ratio of the wake behind isolated

wake behind the roughness elements (Shao & Yang, 2008). A similar trend in the roughness length  $z_0$  changing with  $\lambda$  has also been observed (Macdonald et al., 1998a, 1998b). However, the mutual sheltering effect has not been systematically studied nor parameterized. The existing theories of drag on rough surfaces do not sufficiently validate the mechanism of the drag changing with  $\lambda$ , particularly on dense surfaces (Shao & Yang, 2005; Walter et al., 2012). The lack of experiment and simulation data regarding dense surface limits the understanding of the threshold roughness density ( $\lambda_a$ ) and the dimensions (length and height) of the wake under the influence of mutual sheltering effect, and the trend of drag changing with the roughness density need to be studied. To understand the physical meaning of  $\lambda_a$ , and express the drag and drag partition as functions of  $\lambda$ , and  $\lambda_a$  is the first aim of this thesis.

Mass transfer from the atmosphere to rough surfaces, in term of dry deposition, can be quantified by deposition velocity (Seinfeld & Pandis, 2012). The estimations of deposition velocity have discrepancies up to two orders of magnitude against measurements on natural surfaces with high canopies (Gallagher et al., 1997b; Kouznetsov & Sofiev, 2012). For decades, such discrepancies are common between estimation and field measurements but not well understood (Gallagher et al., 1997a; Kouznetsov & Sofiev, 2012; Zhang & He, 2013). Thus, existing models focus mainly on deposition onto smooth surface and surfaces with low roughness (Kouznetsov & Sofiev, 2012; Petroff et al., 2008; Zhang & He, 2013). With better understanding of momentum transfer over rough surfaces, particle deposition onto dense surfaces can be better predicted, and further consideration of complex natural conditions can be undertaken. Therefore, the second aim of this thesis is to understand the mechanism of deposition on rough surface and explain the results of field measurements.

Both aims of this thesis are closely related. As there are insufficient experimental data for analyzing the wake, drag and deposition on rough surface, hundreds of runs of numerical simulation are conducted for air flow and dust flux over rough surfaces. Multiple conditions of roughness densities, wind speeds and particle sizes are considered. Both theoretical study and analyzing of the simulation data are carried out to achieve these aims.

Necessary knowledge regarding the air flow over rough surfaces are introduced in Section 1.2. The definitions of deposition velocity, introduction of deposition models and their applications are introduced in Section 1.3. Section 1.4 lists the scientific problems addressed in this thesis and the thesis outline is provided in Section 1.5.

## 1.2 Existing theories on airflow over rough surfaces

### 1.2.1 Surface parameters for a geometric method

Micrometeorological methods can be used to measure wind profile and deduce drag on surfaces. But, field measurements are expensive. A geometric method can determine the drag on surface with only the dimension of surface roughness and a reference wind speed, without expensive towers and instruments. The geometric methods use algorithms to calculate aerodynamic

---

elements (Chap. 2); (d) A function of  $b/h$  of roughness element (Chap. 3); and, (e) a new parameter in the drag partition theory (Chap. 3).

parameters based on the measurements of surface geometry (Grimmond & Oke, 1999), and it is needed in the modeling of atmospheres for estimation of the flow condition near the surface (Shao, 2008). A good understanding of the shear flow over rough surfaces is required to make a correct estimation of the properties of the flow and build a geometric method. The parameters which characterize the rough surfaces is the most important parameter in a geometric method.

The existing geometric methods describe the surfaces with a quantity known as the frontal area index<sup>3</sup>,

$$\lambda_f = \frac{nA_f}{S} \quad (1.1)$$

where  $n/S$  is the number density of the roughness elements (number of roughness elements  $n$  per unit area  $S$ ) and  $A_f$  is the frontal (silhouette) area of a roughness element. For elements with rectangular frontal areas,  $\lambda_f$  can be expressed as<sup>4</sup>

$$\lambda_f = \frac{nbh}{S} = \frac{bh}{l^2} \quad (1.2)$$

Here  $h$  is the height of the roughness elements.  $l$  is the distance between elements, which is measured from the frontal edge of an element to the frontal edge of the adjacent element. As only the elements with equal length and width or ridge-like elements are considered in this thesis,  $b$  represents both the length and width of the elements.

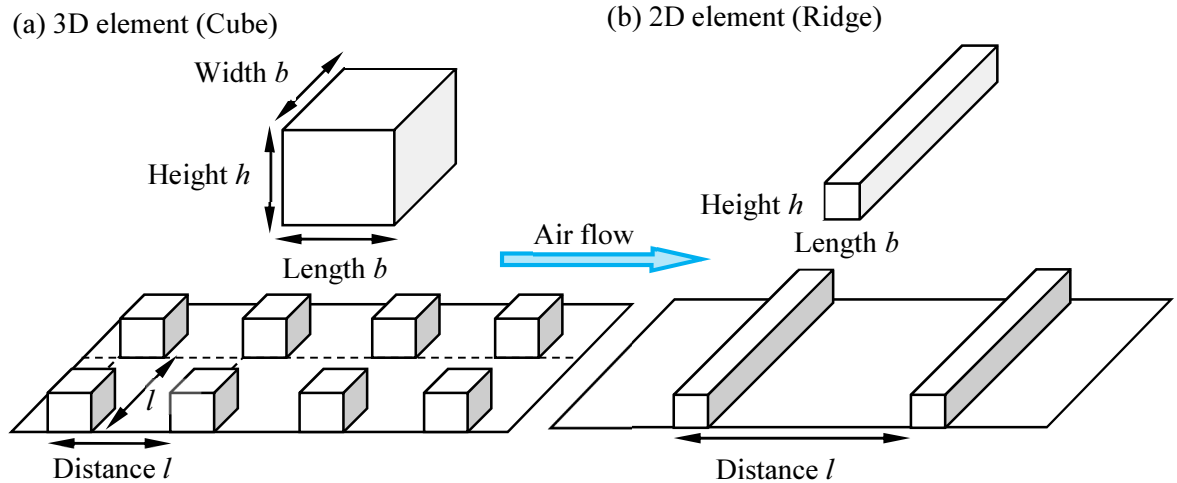


Figure 1.1 Geometry of rough surfaces. (a) Rough surface with 3D cube elements;  
(b) Rough surface with 2D ridge elements.

There are mainly two kinds of roughness elements considered in this thesis, the 3D elements, i.e., cubes or cylinders, and 2D elements, i.e., ridges which lies perpendicular to the streamwise direction. Generally, roughness elements with identical heights were considered in each of

<sup>3</sup> Frontal area index is equal to the square of roughness density when the height and length of elements are equal.

<sup>4</sup> In this thesis, only the surface with 3D elements of equal width and length or 2D elements of ridges with infinite width are considered. The width of element is rarely discussed in this study. Hereafter, if not specified, the parameter  $b$  refers to the length of elements.

previous experiments (Marshall, 1971; O'Loughlin, 1965; Raupach et al., 1980). Therefore, a roughness density is defined for these elements as the ratio of the horizontal projection area of one element,  $A_s$ , to its occupied area,  $S$ :

$$\lambda = \frac{nA_s}{S} \quad (1.3)$$

Note that, for all cases, elements are considered to be cubes for 3D elements or ridges for 2D elements. For 3D roughness elements (Cubes),  $A_s = b^2$ , their roughness density is:

$$\lambda = \frac{b^2}{l^2} \quad (1.4)$$

For 2D roughness elements (Ridges),  $A_s = bl$ , their roughness density is:

$$\lambda = \frac{b}{l} \quad (1.5)$$

For convenience, Equation (1.5) is used as definition for roughness density for all cases in this thesis, while  $\lambda^2$  is referred to the roughness density of 3D elements. The relationship between roughness density in this thesis and frontal area index, when  $b = h$ , is

$$\lambda = \sqrt{\lambda_f} \quad (1.6)$$

For the geometric method, a database of the flow properties as functions of continuous  $\lambda$  helps to estimate these properties on any rough surfaces (Grimmond & Oke, 1999a).

The most important new parameter introduced in this thesis is the threshold roughness density, i.e.,  $\lambda_a$ . It has multiple physical meanings, these meanings are introduced in the theoretical study and the analysis of the first three chapters. Here, it is firstly defined as the threshold roughness density for sparse surface ( $\lambda < \lambda_a$ ) and dense surface ( $\lambda > \lambda_a$ ). The details of its other physical meaning are discovered and applied in Chapter 2 and 3, and concluded in Chapter 6.

### 1.2.2 Definition of drag and drag partition

The surface drag is the main concern in the study of fully-developed turbulent shear flow (Schlichting, 1936), e.g., in the atmospheric boundary layer or for engineering applications. There are a wide range of measurements and theories of drag on rough surfaces. The most complete early work, on sand-roughened pipes, was conducted by Nikuradse (1933). His work stemmed from the concept of 'equivalent sand-grain roughness height', which also was the basis of Von Karman - Prandtl's resistance law, valid at large Reynolds numbers (Prandtl, 1963). Many drag problems involve surfaces unlike Nikuradse's sand-roughness study. The drag on riveted ship hulls led to the consideration of regular arrays of roughness elements with simple geometry, which became and remains a standard method of approaching a rough surface (Macdonald et al., 1998a; Raupach et al., 1980; Stone & Shen, 2002; Thom, 1972a; Walter et al., 2012a; Wooding et al., 1973).

Schlichting (1936) defined the drag and drag partitions on a rough surface as:

$$\tau = \tau_r + \tau_s \quad (1.7)$$

where  $\tau$  is the total shear stress on the rough surface,  $\tau_r$  and  $\tau_s$  are the shear stresses on the roughness elements and the shear stress on the underlying surfaces, respectively. The total shear stress,  $\tau$  can be expressed as a function of friction velocity,  $u^*$ :

$$\tau = \rho u_*^2 \quad (1.8)$$

where  $\rho$  is the density of air. To relate  $\tau$  with the reference wind speed at the height of roughness elements,  $u_h$ , the drag coefficient  $C_d$  and the friction coefficient  $c_d$  are introduced:

$$C_d = \frac{u_*^2}{u_h^2}, \quad c_d = \frac{u_*}{u_h} \quad (1.9)$$

Raupach (1992) developed a theory of drag and drag-partition to estimate the surface drag. His estimation of total drag and friction coefficient are based on hypotheses, while the expressions of drag partition is a simple function of frontal area index  $\lambda_f^5$ :

$$\frac{\tau_r}{\tau} = \frac{\beta \lambda_f}{1 + \beta \lambda_f} \quad \frac{\tau_s}{\tau} = \frac{1}{1 + \beta \lambda_f} \quad (1.10)$$

where  $\beta = C_r/C_s$ , where  $C_s$  is the drag coefficient for the unobstructed ground surface, and  $C_r$  is the drag coefficient for single roughness element. Equation (1.10) fits well with experimental data (Marshall, 1971; Raupach et al., 1980). It is determined that  $\tau_r/\tau$  increases as  $\lambda_f$  increases,  $\tau_s/\tau$  decreases as  $\lambda_f$  increases. When  $\tau_r = \tau_s$ ,  $\lambda_f = 1/\beta$ . However, this theory (Raupach, 1992) is limited to sparse surface and it does not distinguish the shape of elements. Shao and Yang (Shao & Yang, 2008) inherited the idea of Raupach and extended the model to dense surface without changing or validating the hypotheses. The lack of laboratory measurements of drag on dense rough surfaces is the main reason that hypotheses must be used rather than facts in the drag and drag partition theory (Raupach, 1992; Shao & Yang, 2008).

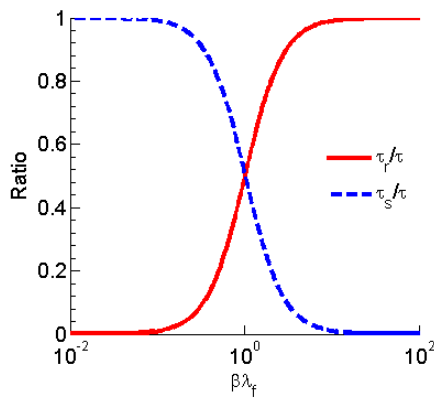


Figure 1.2 Theoretical drag partition from Equation (1.10).

<sup>5</sup> Frontal area index is equal to the square of roughness density when the height and length of elements are equal. Thus, in this thesis Frontal area index can be replaced by  $\lambda^2$ .

### 1.2.3 Wind profiles over smooth and rough surfaces

#### 1.2.3.1 Universal velocity profile

Schlichting (1936), proposed the universal velocity profile (logarithmic wind profile), for fluid flow in the boundary layer, as

$$\frac{u(z)}{u_*} = \frac{1}{\kappa} \ln \left( \frac{z - d}{z_0} \right) \quad (1.11)$$

where  $\kappa$  is the von Karman constant,  $z_0$  is the roughness length,  $d$  is the zero-plane displacement and  $u_*$  is the friction velocity. The universal profile has been used as the framework for analyzing the fluid and meteorological boundary layer (Garratt, 1994; Stull, 1988). Although the universal wind profile is semi empirical, it provides accurate wind profile estimation in inertial layer over rough and smooth surfaces (Cowan, 1968; Holmes, 2001; Simiu & Scanlan, 1996; Sini et al., 1996).

Series of studies were conducted to assess each of these parameters in Equation (1.11). Wind tunnel experiments and numerical simulations were conducted to measure the wind profile and the surface drag. The roughness length, friction velocity together with the zero-plane displacement were deduced by fitting the wind profile with the universal wind profile (Ahmadi & Chowdhury, 1991; Chung & Pullin, 2009; Grant & Nickling, 1998; Macdonald et al., 1998a; Yang & Shao, 2008). In the simulation of this thesis, these important parameters are acquired for various surfaces and flow conditions by this method.

#### 1.2.3.2 Corrected wind profile over rough surfaces

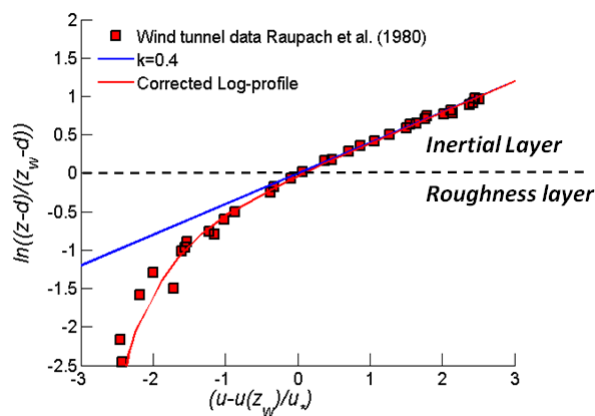


Figure 1.3 Wind profile in the inertial layer and the roughness layer (Raupach, 1992)

Inside a fully developed turbulent flow, although the flow in the inertial layer follows the logarithmic law, the wind profile in the roughness layer is influenced by the shear flow induced by the roughness elements (O'Loughlin, 1965; Thom, 1975). Raupach et al. (1980) proposed a model for wake diffusion and provided an analytic form for the velocity profile in the layer of

wake diffusion, i.e. the roughness layer. The enhanced diffusivity in this layer was modeled by holding the diffusivity constant below the height of roughness layer,  $z_w$ ,

$$K(z) = \begin{cases} \kappa u_*(z - d) & z > z_w \\ \kappa u_*(z_w - d) & z \leq z_w \end{cases} \quad (1.12)$$

where  $K(z)$  is the turbulent diffusivity. The drag was assumed to be constant throughout the boundary layer. Accordingly, the shear stress is

$$\tau = \rho K(z) \frac{du}{dz} \quad (1.13)$$

Raupach et al. (1980) studied the details of the wind profile near the surface in a wind tunnel experiment, and corrected the wind profile, when the logarithmic profile does not fit near the surface (Figure 1.3 ).

$$\frac{\kappa u(z)}{u_*} = \frac{1}{\kappa} \ln \left( \frac{z - d}{z_0} \right) + \psi \left( \frac{z - d}{z_w - d} \right) \quad (1.14)$$

Equation (1.14) is an analytic model for the effect of wake diffusion in the roughness layer. It also can be written as velocity difference:

$$\frac{u(z) - u(z_w)}{u_*} = \begin{cases} \frac{1}{\kappa} \ln \left( \frac{z - d}{z_w - d} \right) & z > z_w \\ \frac{1}{\kappa} \frac{z - z_w}{z_w - d} & z \leq z_w \end{cases} \quad (1.15)$$

References	Methods	Surface types	$z_w$
O'Loughlin & Annambhotla (1997)	Water tunnel	Cubic array	$z_w < 2h$
Mulhearn & Finnigan (1969)	Wind tunnel	Random gravel surfaces	$z_w = 2l$
Raupach et al. (1980)	Wind tunnel	Cylinder Array	$z_w < 2.5h$
Raupach (1992)	Wind tunnel	Cylinder Array	$z_w = c_w(h-d) + d$ $1.3 < c_w < 1.8$
Cheng & Castro (2002)	Wind tunnel	Cubic array Random height surface	$z_w = 1.8 h$ $z_w = 2.5 h$
This thesis <sup>6</sup>	2D Simulation	2D Cubic array	$1.4 < z_w/h < 2.6$
This thesis <sup>7</sup>	3D Simulation	Ridge array	$1 < z_w/h < 1.6$

Table 1.1 Experimental measurements of the height of the roughness layer ( $z_w$ ) and the values of  $z_w$  determined in this thesis

<sup>6</sup> 2D Simulation result of  $z_w$  in Section 2.5.3.3

<sup>7</sup> 3D Simulation result of  $z_w$  in Section 3.6

This equation shows the relationship among the velocity difference, the friction velocity and the dimensionless term on the right of equation. This relationship is used in Chapter 3 for the parameterization of momentum flux.

In Equation (1.15), the term,  $z_w$ , is an empirical parameter, although it is important for determining the wind profile and the resistance of the roughness layer (Kastner-Klein & Rotach, 2004; Nikora et al., 2004; Sellers et al., 1997). The depth of the roughness layer,  $z_w$ , is unknown in most of wind tunnel experiments of flow over rough surfaces and no systematic study of it has been presented in the literatures. Practically,  $z_w$  is assumed to be dependent on the dimensions of rough surface, some of measured  $z_w$  in experiments and simulations are shown in Table 1.1.

O'Loughlin & Annambhotla (1969) conducted experiments in a water channel, and their results suggested that the upper limit of roughness layer occurs at  $z_w = 2h$  for sparse surface with cubic elements. Mulhearn and Finnigan (1978) examined wind tunnel flow over random gravel surfaces in a wind tunnel, and they assumed that  $z_w = 2l$ . Raupach et al. (1980) concluded that wake diffusion is effective below  $z = h + 1.5b$ ; and the horizontal inhomogeneity is not negligible below  $z = h + l$ . The roughness layer is a region of horizontal inhomogeneity, so a safe criterion is then introduced for measurement and simulation, which ensured that both effects were avoided, i.e.  $z > h + 1.5b$ . When the elements are cubes, the height, length and width of an element are the same, the estimated roughness layer is then  $z_w < 2.5h$ . Raupach (1992) proposed a drag partition theory and assumed that the  $z_w - d = c_w(h - d)$ , where  $c_w$  is a value between 1.3 and 1.8. More recently, Cheng and Castro (2002) showed that  $z_w$  is  $1.8h$  for regular cubic array and  $2.5h$  for certain surfaces with random height of elements and a roughness density  $\lambda = 0.25$ . In this case,  $h$  is the average height of elements. In this thesis, the value of  $z_w$  is determined for both 2D and 3D simulation.

### 1.2.4 The wake behind roughness elements

On rough surfaces, when the mainstream encounters a roughness element, the streamlines separates from the element and reattaches the surface at a distance. Thus, a wake is formed behind the element. In a time averaged flow field, the length of the wake can be determined by the flow conditions and the surface properties. The flow condition can be categorized into three types in term of the roughness density (Grimmond & Oke, 1999), i.e.,

- (1) Flow obstructed by isolated elements ( $\lambda < \lambda_a$ );
- (2) Flow disturbed by densely distributed elements ( $0.5 > \lambda > \lambda_a$ ); and
- (3) Skimming flow over a highly dense surface ( $\lambda > 0.5$ ).

The corresponding wakes can be distinguished into the wake behind the isolated element, the suppressed wake on the dense surface, and the undeveloped wake on the highly-dense surface. However, the wake on a highly-dense surface is suppressed by the elements by a mechanism that is similar to that of mutual sheltering on a dense surface (Shaw & Pereira, 1982). In addition, skimming flow over a highly dense surface is similar to the flow over a smooth surface. Therefore, the wake on highly dense surface is not discussed in this thesis; rather the focus is on the first two types of wakes, i.e., the wake behind an isolated element and the wake on a dense surface (Figure 1.4).

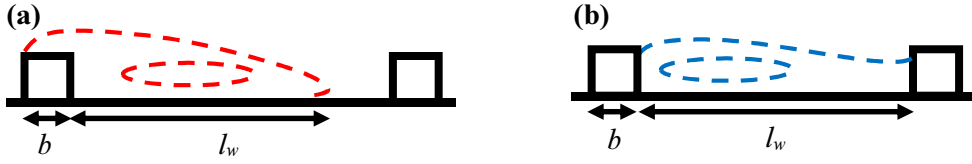


Figure 1.4 Illustration of the flow and wake on rough surfaces. (a) surface with isolated elements or sparse surface; (b) dense surface. The surface and the elements are in black line, and the imagined wake and the vortices are represented by the dashed line in different colors.

The length of the wake is the key to distinguish these two types of surfaces, as shown in Figure 1.4. Previous simulations of flow over ridges (or ribs) measured the reattachment length, i.e.,  $l_w$ , which is the distance from the back of the element to the reattachment point:

For sparse surfaces, the separation of the flow occurs at the front edge of the element and the reattachment is on the underlying surface. In this case, the wake is a larger circulation area including the vortices that over the top of the element and the vortices that behind the elements. The length of the wake is the attachment length plus the length of the element, i.e.,  $L_w = l_w + b$ .

For dense surfaces, the separation of the flow may occur at the front edge or the back edge (tailing edge) and the reattachment is on the front edge of adjacent element. In this case the wake is a circulation region with some secondary vortices. The length of the reattachment point determines the length of the wake, i.e.,  $L_w = l_w$ .

In the previous studies, Liu et al. (1966) reported a reattachment length of  $5h$  for  $l/h = 7$  and  $l/h = 11$ , and  $6h$  for  $l/h = 23$ , based on a flow visualization technique. Le et al. (1997) performed DNS of a turbulent flow over a backward facing step, they showed that the averaged instantaneous reattachment is  $6.3h$ . In the DNS simulation of Leonardi et al. (2003), the reattachment length is  $5.8h$  for  $l/h = 19$ . However, there is no systematical study of reattachment length or the length of wake to parameterize them as function of roughness density.

To relate the dimension of the wake to surface drag, Raupach (1992) defined the wake behind each element as sheltering area/volume, and brought it to the drag and drag partition theory. The dimensions of wake was assumed to be related to the friction coefficient. In the attempt of Shao and Yang (2008) to extend the theory of Raupach to denser surfaces, the effect of mutual sheltering was discussed. They assumed that the transverse sheltering of the wake was limited when the vortices are overlapped on a dense surface. However, it has not been proven experimentally or theoretically whether the transverse sheltering or the streamwise sheltering among wakes is more important. Since the streamwise length of a wake is larger than its spanwise length, this study focus on the streamwise sheltering. Ridges are used as roughness elements in the simulation, which eliminate the possibility of transverse mutual sheltering. And the stream-wise lengths of the wakes were considered important for determining the drag and drag partition.

### 1.3 Existing theories on dry deposition

Dry deposition is the transfer of particles from the atmosphere to surface in the absence of precipitation (Petroff et al., 2008). It is an important link in dust cycle and has been studied extensively for mineral and bacteria transfer, radioactive fallout contamination, pollution, and dispersion of industrial chemicals (Holsen & Noll, 1992; Kreutzkam et al., 2012; Lai, 2002; McLaughlin, 1989; Ruijrok et al., 1995; Sehmel, 1980; Uematsu et al., 2010; Volkov, 2004; Zender, 2003; Zhang & Li, 2008).

The dry deposition process onto smooth surfaces is well understood (Kouznetsov & Sofiev, 2012). However, the estimation and the measurements of deposition velocity on rough surfaces have discrepancies up to two orders of magnitude, and these discrepancies are not well understood (Gallagher et al., 1997a; Kouznetsov & Sofiev, 2012). The formulations for dry deposition processes are usually needed to couple to atmospheric dispersion models (Gong & Bartie, 1997; Uno et al., 2006; Zender, 2003). When a deposition model is used in a large-scale atmospheric dispersion model, the error in the estimation of the deposition velocity affects the calculation of particle flux and concentration, thereby further increases the systematic error in the estimation of dust cycle. Therefore, better understanding and better parameterization of this process is needed.

The deposition process can be divided into the processes of eddy diffusion, gravitational transfer, molecular diffusion, interception, impaction and rebound (Giorgi, 1986; Kouznetsov & Sofiev, 2012; Slinn, 1982b; Zhang et al., 2001a). Other processes like thermophoresis and electrophoresis are also considered in some models (Petroff et al., 2008). These processes respond to different diameter range of particles or different external forces that acted on the particles.

The most extensively used dry deposition models are based on a series of assumptions and idealized conditions (Slinn & Slinn, 1980). Such simplifications of the actual physical processes result in uncertainties in the determination of the deposition velocity (Sehmel, 1980). For example, the collection of medium-sized ( $0.1 < d_p < 1\mu\text{m}$ ) particles by interception process is parameterized based on the experiment results of particles colliding with a cylinder, rather than intercepting with a flat plate with roughness elements (Fuchs, 1964; Giorgi, 1986); the concentration of particles is assumed to be zero in the roughness layer, while some particles may remain there before they are deposited; and the vertical flux is generally assumed to be constant, but this may be accurate only in a short range of height (Kouznetsov & Sofiev, 2012). The reliability of these simplifications is susceptible because unreasonable assumptions are made, and because we do not have a sufficient explanation of deposition on rough surfaces (Gallagher et al., 1997; Kouznetsov & Sofiev, 2012). We urgently need an effective operational deposition model.

This study improves the physical understanding of the deposition process and develops a new model for predicting of deposition on rough surfaces. Deposition processes are described in more detail in the following sections.

### 1.3.1 Definition of deposition velocity

Chamberlain (1953) defined the most important concept in dry deposition, i.e., the deposition velocity  $v_d$ , as the downward flux divided by the atmospheric concentration of the matter being deposited at a height,  $z$ ,

$$v_d(z) = \frac{F}{C(z)} \quad (1.16)$$

where  $F$  is the mass flux and  $C(z)$  is the concentration of the particles at height  $z$ .  $F$  is defined positive downwards. The Equation (1.16) states that  $v_d$  is downward flux divided by local concentration. It is assumed that the concentration at the surface is almost zero, i.e.,  $C(0) \rightarrow 0$ , since the surface is considered to be a perfect sink for particles.

Laboratory measurements of deposition velocity on smooth surfaces and sparse surfaces had provided interpretable datasets, and they were well reproduced by existing models (Chamberlain et al., 1966; Kouznetsov & Sofiev, 2012; Liu & Agarwal, 1974; Slinn, 1982b; Zhang et al., 2001a). However, Figure 1.5 shows that the value of the deposition velocity can shift by two orders of magnitude when it is measured in natural condition.

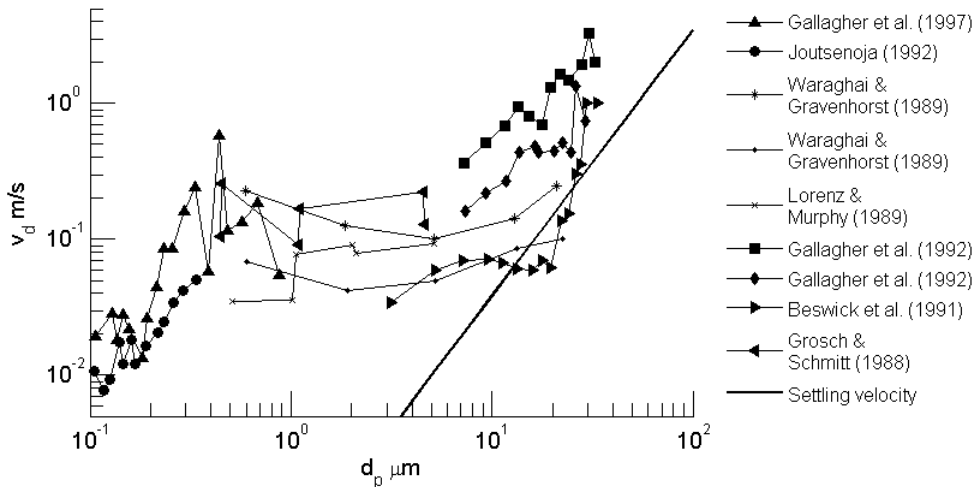


Figure 1.5 Deposition velocity measured in natural conditions: The experimental data have different markers and the settling velocity of the particles is shown for comparison (Beswick et al., 1991; Gallagher et al., 1997a; Gallagher et al., 1992; Grosch & Schmitt, 1988; Joutsenoja, 1992; Lorenz & Murphy Jr, 1989; Waraghai & Gravenhorst, 1989).

The experimental data in Figure 1.5 were collected over high canopies, and existing models do not provide satisfactory estimation of deposition velocity over these dense surfaces (Gallagher et al., 1997b; Kouznetsov & Sofiev, 2012). The expressions used in these models cannot estimate the deposition velocity as high as these measurement. In the natural condition, air flow is unsteady, turbulent flow with intermittent phenomena (Mahrt, 1989; Paradisi et al., 2012). The wind speed changes from time to time, and the concentration of dust and the dust flux are

also unsteady due to the complexity of the surface roughness and unsteady air flow (Gallagher et al., 1997). These are the possible causes of the discrepancies.

The following sections introduce the evolution of the existing dry deposition models, from the first theory to current models that are used for smooth and rough surfaces.

### 1.3.2 Dry deposition models

	Surfaces	Turbulence transfer	Bounce -off	Brownian diffusion	Interception	Inertial impaction	Sedimentation
Slinn, 1977	Smooth	Y					Y
	Vegetation	Y					Y
Bache, 1979	Vegetation	Y				Y	Y
Sehmel & Hodgdon, 1980	Vegetation	Y		Y	Y	Y	Y
Legg & Price, 1980	Crop	Y				Y	Y
Slinn and Slinn, 1980	Water	Y		Y	Y	Y	Y
Slinn, 1982	Forest	Y	Y	Y	Y	Y	Y
Davidson, 1982	Grass	Y		Y	Y	Y	Y
Wiman & Argen, 1985	Forest	Y		Y		Y	Y
	Smooth	Y	Y	Y		Y	Y
	Bluff	Y	Y	Y		Y	Y
	Ocean	Y		Y		Y	Y
Peter & Eiden, 1992	Vegetation	Y	Y	Y	Y	Y	Y
	Forest	Y		Y		Y	Y
	Any	Y	Y	Y	Y	Y	Y
Petroff, 2008	Vegetation	Y		Y	Y	Y	Y
Kouznetsov, 2012	Smooth	Y					Y
	Vegetation	Y	Y	Y	Y	Y	Y

Table 1.2 Dry particle deposition models mentioned in this paper

The pioneer scientist Chamberlain (Chamberlain, 1967; Chamberlain et al., 1966) defined and measured the deposition velocity of fine particles. He illustrated the advantage of specifying the trapping efficiency in terms of a deposition velocity, and a Stanton number was used to identify the differences between momentum and mass transfer. His results showed that the wind speed and the drag coefficient were related to deposition velocity.

In an important paper, Slinn (1977) presented a semi-empirical formula for the particle dry deposition of particles on smooth surfaces. On such surfaces, his model excludes the 'free-flight' model of Friedlander and Johnstone (1957), and its variations (Chamberlain et al., 1966; Davis,

1969); instead, the model incorporated Owens' (1969) suggestion that the particles finally reach the surface as a result of the convection created by bursts of turbulence in the roughness layer. Consistent with the model of Brutsaert (1975). The physical picture envisioned by Slinn (1977) that the particles being advected through the roughness sublayer by randomly renewing eddies, is similar to the consideration of wake in this paper. The particles are carried by the inrushing branch of the eddies, and they impinge on the wall with an efficiency that is analogous to the collection efficiency for a jet impinging on a flat plate, which Slinn expressed by a semi-empirical formula obtained from a fit to the deposition data of Liu and Agarwal (1974). Then the collection of particles by a surface depends on the collection efficiency, considering that the aerodynamic effect is determined by the Stokes and Schmidt numbers.

Slinn (1982) presented an improved theoretical framework for the dry deposition of particles on vegetation. This framework is similar to that used for the momentum transferred to vegetative canopies and approximate analytical solutions are sought. The result is illustrated for different collection efficiencies based on wind tunnel data obtained by Chamberlain (1967).

The results suggest that dry deposition velocities for particles in the size range of 0.1-1.0 $\mu\text{m}$  are typically about an order-of-magnitude smaller than many air quality models. But the comparison with available field measurements does not provide a reliable test of their validity. Zhang et al. (2001) simplified Slinn's model (1982) and applied this model to 15 Land-use categories (LUCs) and Zhang & He (2013) used his model to analyze the deposition velocity of specific size ranges of PM<sub>2.5</sub>, PM<sub>2.5-10</sub>, and PM<sub>10+</sub> onto 26 LUCs. Many of these data were based on the study of Wesely et al. (1985) who used empirical expressions for the surface resistance to sulfate deposition that were based on micro-meteorological field measurements. Slinn's model (1982) is introduced in this chapter, and the model of Zhang et al. (2001) is used in Chapter 4.

The movement of particles is assumed to follow the air flow completely, but Giorgi (1986) allowed the deposition velocity of particles to be collected with an efficiency greater than the deposition of momentum, even before gravitational settling becomes dominant. This is an important difference between this model and Slinn's earlier model, in which particles are never transferred to the surface more efficiently than momentum in non-sedimentation-dominant regimes. The importance of including this feature in the model was emphasized. For example, by the numerical calculations of Belot et al. (1976), which showed that the deposition of high inertia particles at high wind speeds on a pine forest can be faster than the transfer of momentum. In Gallagher's experiment (Gallagher et al., 1997) measurements of the deposition velocity on high canopies were much larger than terminal settling velocity. These feature of deposition will be addressed for large particles in this thesis.

Kouznetsov & Sofiev (2012) developed a vertical dispersion framework that accounted for a vertical inhomogeneity of the diffusion coefficient and the regular vertical velocity. In this model, deposition onto a smooth surface was well reproduced, and no empirical parameters were used in the expression of the deposition velocity. The model's prediction was in good agreement with experimental results for a smooth surface and a lower canopy, but discrepancies still exist for a high canopy. This model is introduced and used in Chapter 5 for studying the deposition in natural flow.

The other dry deposition models are listed in Table 1.2 (Bache, 1979; Davidson & Wu, 1990; Peters & Eiden, 1992; Petroff et al., 2008; Ruijrok et al., 1995; Sehmel & Hodgson, 1978; Wiman & Ågren, 1985).

### 1.3.3 Applications of dry deposition models

Model Name	Original Dry deposition model	Dry deposition Model	Reference
CEMSYS5	Raupach (1992)	Single Layer Model	Shao (2003)
CFORS	Chamberlain (1967)	Constant value	Uno (2003)
COAMPS	Stull (1998)	$v_d = u^*/u_r$	Liu (2003)
DEAD	Wesely (1985)	Wesely (1985)	Zender (2003)
DREAM	Slinn (1982)	Giorgi (1986)	Nickovic (2001)
ECHAM5-HAM	Wesely (1985)	Wesely (1985)	Stier (2003)
GOCART	Slinn (1982)	$v_d = 3u^*$	Ginoux (2004)
ITR	Chamberlain (1967)	$v_d = v_g$	Tagen (2003)
HCM	Wesely (1985)	Seinfeld (1998)	In and Park (2003)
MASINGAR	Wesely (1985)	Seinfeld (1998)	Tanaka (2003)
NRL	Wesely (1985)	Walcek (1986)	Christensen (1997)
NARCM	Slinn (1982)	Zhang (2001)	Gong (2003)

Table 1.3 Dry deposition models used in globe scale dust models.

After decades of development, there are two main types of dry deposition models that are used in global dust models, i.e., the empirical model (e.g. Wesely 1985, 1989) and the process oriented model (Kouznetsov & Sofiev, 2012; Slinn, 1982; Zhang et al., 2001). The process oriented model is based on the physical process of dry deposition, and introduced in the previous section; the empirical model is based on field measurements. Both models well reproduce certain field and wind tunnel experimental data. The process oriented models consider detailed physical processes, so they can be used for different particle sizes, surfaces and atmospheric conditions. The empirical models can be applied only to conditions of the measurements they are based on (Petroff et al. 2008; Pryor et al. 2008; Zhang et al. 2001).

Although the process oriented models are considered to be more accurate, many large scale dust models are empirical models or simplified process-oriented models, due to their simplicity. Hence, the influence of a complex terrain on the deposition process is not clearly understood, the process oriented models are seldom tested in large scale model, as listed in Table 1.3 (Christensen, 1997; Ginoux et al., 2004; Gong et al., 1997; Gong et al., 2003; In & Park, 2002; Nickovic et al., 2001; Seinfeld & Pandis, 2012; Shao et al., 2003; Stier et al., 2005; Tanaka & Chiba, 2006; Tegen, 2003; Uno, 2003; Walcek & Taylor, 1986; Zender, 2003).

### 1.3.4 A two layer model of dry deposition

Slinn's model (1982) has been widely accepted and used due to its analytical form. Alternative dry deposition models require numerical solvers (e.g. Peter and Eiden, 1992; Wiman and Årgen, 1985; Wiman et al. 1985), or they consider only a specific range of the particle size distribution (Bache, 1979). In many cases, the applied deposition models are either variants of Slinn's model (1982), or they use several of simplifying assumptions invoked by Slinn.

The Slinn's model (1982) is used to calculate deposition velocity in forests. Transfer of particles through the atmospheric surface layer down to the quasi-laminar sub-layer occurs by turbulent diffusion and Brownian diffusion, interception, impaction and sedimentation. Slinn's model is an Eulerian model with the concept of diffusivity to describe the influence of turbulence and Brownian motion. Particles are considered as another continuum in addition to airflow. Therefore, conservation equations are solved to estimate the motion of the particles. As a consequence of the no-slip boundary condition for airflow at the surface, the air at an infinitesimally small distance above a stationary surface is stationary.

The diffusivity and wind profile are obtained by solving a simplified momentum transfer equation:

$$\frac{\partial}{\partial z} \left( K(z) \frac{\partial u}{\partial z} \right) = (c_d \alpha u) u - \frac{1}{\rho} \left( -\frac{\partial p}{\partial x} \right) \quad (1.17)$$

where  $K(z)$  is the eddy diffusivity for momentum,  $c_d$  is the average drag coefficient of the vegetation at height  $z$  and of total surface area per unit volume  $\alpha$ .  $u$  is wind speed,  $p$  is air pressure. The expression of  $v_d$  is:

$$v_d = v_g + \frac{1}{r_a + r_b}, \quad v_g = \frac{\rho_p d_p^2 g C_c}{18 \mu} \quad (1.18)$$

where,  $v_g$  is the gravitational settling velocity,  $r_a$  and  $r_b$  are the aerodynamic resistance and the surface resistance, respectively.  $\rho_p$  is the density of particles;  $d_p$  is the diameters of particles;  $C_c$  is the Cunningham correction factor;  $\mu$  is dynamic viscosity. The formulas of  $r_a$  and  $r_b$  are:

$$r_a = \frac{u_r - u_h}{u_*^2}, \quad r_b = \frac{u_h}{u_*^2} \frac{1}{\sqrt{\varepsilon}} \left( \frac{1 + \sqrt{\varepsilon} \tanh(\gamma \sqrt{\varepsilon})}{\sqrt{\varepsilon} + \tanh(\gamma \sqrt{\varepsilon})} \right) \quad (1.19)$$

where  $u_h$  is the velocity at height  $h$ ,  $u_r$  is the reference velocity,  $\varepsilon$  is the collection efficiency, and  $\gamma$  is a parameter that characterizes the wind profile in a canopy, which is expected to be in the range  $2 < \gamma < 5$ . The analytical form of the deposition velocity can be deduced using Equation (1.17), (1.18) and (1.19) :

$$v_d = v_g + C_d u_r \left[ 1 + \frac{u_h}{u_r} \left( \frac{1 - \varepsilon}{\sqrt{\varepsilon} + \tanh(\gamma \sqrt{\varepsilon})} \right) \right]^{-1} \quad (1.20)$$

where  $\varepsilon$  is defined as:

$$\varepsilon = (E_B + E_{IN} + E_{IM}) e^{-b\sqrt{S_t}} \quad (1.21)$$

Collection efficiency for Brownian diffusion, Impaction, and Interception can be expressed as:

$$\begin{cases} E_B = C_{vd} S_c^{-\frac{2}{3}} \\ E_{IN} = C_{vd} \left( F_s \left( \frac{d_p}{d_p + d_s/2} \right) + (1 - F_s) \left( \frac{d_p}{d_p + d_L/2} \right) \right) \\ E_{IM} = \left( \frac{S_t^2}{1 + S_t^2} \right) \end{cases} \quad (1.22)$$

where  $d_s$  and  $d_L$  are the smaller and larger collectors, respectively,  $F_s$  is the ratio of the smaller collectors.  $S_c$  is Schmidt number,  $S_t$  is average Stokes number:

$$S_c = \frac{v}{D}, \quad S_t = \frac{v_g u_*}{gA} \quad (1.23)$$

$C_{vd}$  is a factor which is physically related to the fact that Brownian diffusion should be scaled as the viscous drag rather than the total drag  $C_{vd}=C_v/C_d$ .  $C_d$  is the drag coefficient,  $C_v$  is the viscous part of drag coefficient.  $C_{vd}$  is 1 for smooth surfaces, and following the experimental results obtained by Chamberlain (1967), we get:

$$C_{vd} = \frac{1}{3} \quad (1.24)$$

In a simplified version of the model of Slinn (1982), only one diameter of collector  $d_c$  is assigned to the collectors. Thus,

$$r_b = \varepsilon_0 u_* \left( S_c + \left( \frac{d_p}{d_c} \right) + \left( \frac{S_t}{0.8 + S_t} \right)^2 \right) e^{-\sqrt{S_t}} \quad (1.25)$$

where,  $\varepsilon_0$  is a constant. Equation (1.25) is the simplified surface resistance in Zhang's model (Zhang et al., 2001), which is introduced and used in Chapter 4.

## 1.4 Summary of scientific problems

To determine the air flow conditions near a rough surface only by knowing the geometry of the surface and a reference wind speed is the dream of all meteorologist. Without the need for large tower to measure the wind profile, a geometrical method could save a lot of money and also provide reliable estimation for the modeling of the atmospheric boundary layer. A geometrical method for air flow can be very useful in determining momentum and mass transfer.

To construct a geometrical method for air flow over a rough surface requires the determination of drag and drag partitions, the wind profile, and the parameters of the surfaces. There are acceptable theories on airflow over smooth and sparse surfaces, but the lack of experimental data limits the understanding of the flow over dense surfaces. The existing drag and drag partition theory and deposition models are limited to sparse surfaces and the mechanism of flow over dense surface is not well understood. A systematic study of the flow over dense rough surfaces and a dataset of measured or simulated surface drag is needed.

This thesis is focused on two kinds of flow over rough surfaces, i.e., 1) the sparse surface with isolated elements and fully developed wakes and 2) the dense surface with densely distributed elements and suppressed wakes. The flow condition on these surfaces could be categorized by the roughness density and the dimensions of wakes behind each element. Both the roughness

density and the dimensions of wake can be related to drag. This is also the main idea of this study to develop a model for estimating flow properties from the geometry of the obstacles on rough surfaces.

To estimate particle deposition velocity, scientists need to consider the aerodynamic transfer of particles, different types of surface collection processes, wide and continuous distributions of particle sizes and various types of land surfaces. Different collection processes are effective for different ranges of particle sizes. However field measurements are generally orders of magnitude larger than the deposition velocity estimated through these processes. It is possible to improve the estimation of deposition velocity by introducing a new mechanism of shear transportation in the roughness layer to replace the less efficient processes of Brownian diffusion, interception and impaction, etc. Then it is possible to produce deposition model of rough surfaces based on simulation results of a wide range of particle sizes on different kinds of surfaces and for various wind speeds. And successfully reproduces the field measurements on high canopies.

Natural flow is seldom steady, and the problem of intermittent dust flux may be the main cause of errors in the estimation of deposition velocity of small particles. By using a vertical dispersion model and data acquired in field measurements to estimate deposition velocity at all heights and changing with time, it is possible to simulate and understand intermittent flow, unsteady dust supply and the result of field measurements.

## 1.5 Thesis outline

This thesis comprises 6 chapters. In Chapters 2 and 3, the air flow over rough surfaces are analyzed and simulated. Chapter 2 studies the form of wakes in the shear flow by 2D simulation. A theory for drag and drag partition under multiple conditions is built and validated against experimental data and 3D simulation results, in Chapter 3. Chapter 4 simulates the deposition process on rough surfaces and produces a dataset of deposition velocity for a wide range of particles sizes on both dense and sparse surfaces under different wind speeds. Chapter 5 considers the influence of intermittent natural airflow on the deposition of particles and make simulation to explain discrepancies that exists between the estimation and the measurement of deposition velocity on rough surfaces. Chapter 6 concludes the thesis and provides outlook for future studies. Figure 1.6 shows the relation among the Chapters and their focuses.

In Chapter 2, the fundamental flow conditions and the wakes on rough surfaces are studied by running 2D simulations. Air flow over rough surfaces with isolated roughness elements or regularly distributed elements are simulated. The relationship among dimension of wake, strength of shear flow, roughness density, and wind speed are found. A model of the wake on rough surface is built, based on hypotheses. Other parameters of corrected logarithmic wind profile of,  $d/h$ ,  $z_0/h$ ,  $z_w/h$ , and  $u_{zw}$  are also calculated and plotted in diagrams against the roughness density for different wind speeds.

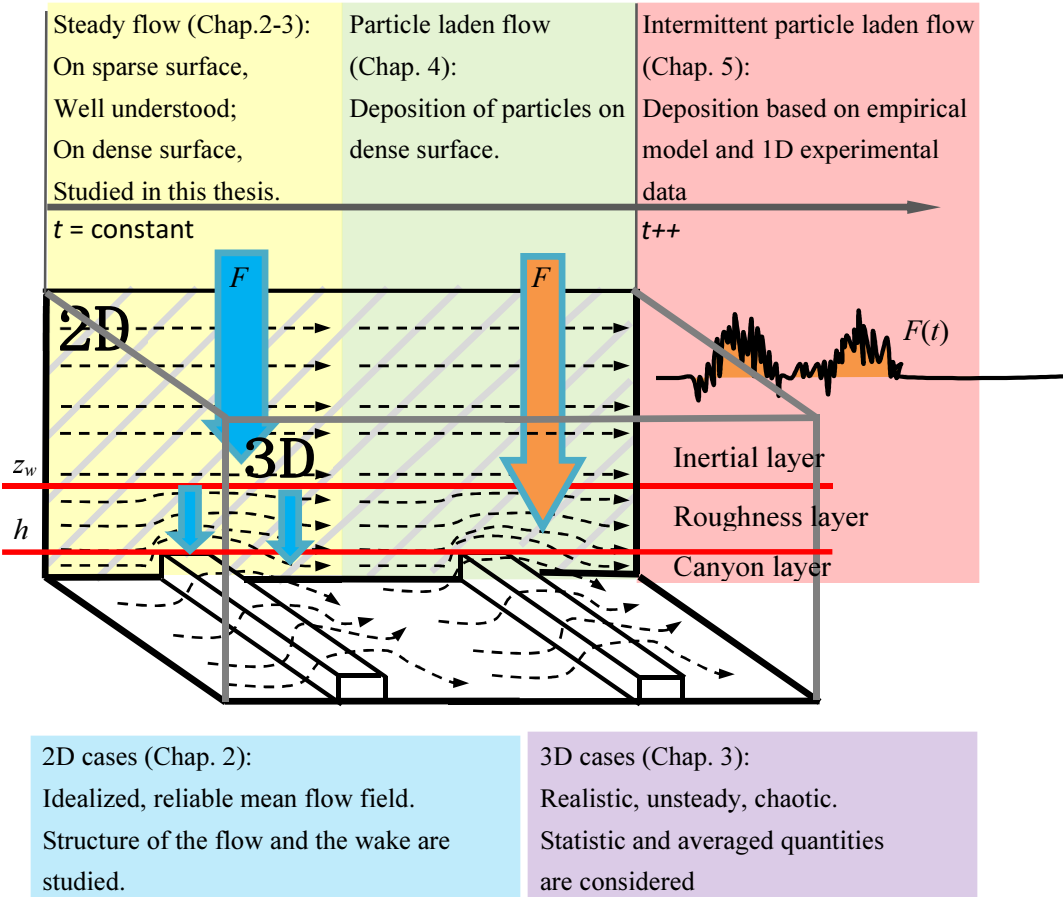


Figure 1.6 The study of momentum and mass transfer to rough surfaces. The steady flow, and the intermittent flow are distinguished by time, i.e.  $t$ . When  $t$  is a constant, the flow is steady; when  $t$  is a variable and  $F(t)$  changes abruptly, the flow is intermittent flow. 2D and 3D study of the flow are also introduced. Momentum flux is in blue, particle flux is in yellow. In unsteady condition, the flux is a function of time. The dashed curves with arrows are the streamlines.  $z_w$  is the height of roughness layer,  $h$  is the height of canyon layer.

In Chapter 3, a resistance method is proposed to quantify momentum flux and a new physical model of drag and drag partition is built. Resistances to the momentum flux and other parameters in the new model are deduced. The new model is validated by the classical experimental data and the 3D simulation data. For the result of 3D simulation, parameters of corrected logarithmic wind profile of  $d/h$ ,  $z_0/h$ ,  $z_w/h$ , and  $u_{zw}$  are also calculated and plotted in diagrams against the roughness density for different wind speeds. A brief comparison between 2D and 3D simulations is also made.

In Chapter 4, sensitivity tests of the parameters in the deposition models evaluate the parameters which cause errors to the estimations of deposition velocity. A new deposition model of the rough surface is built using a complete dataset of deposition simulations on rough surfaces. With proper analysis of the momentum transfer from the atmosphere to the rough surfaces, expressions of deposition velocity as functions of wind speed, friction velocity, particle size or roughness density are given. These Equations are simpler than previous models and considers

the important parameter of roughness density. Finally, this new deposition model is compared to field experiment data for validation. The result agrees well with field measurements on high canopies for the first time.

In Chapter 5, the intermittent conditions of the deposition process is studied. The influence of intermittency on the deposition process are analysed. A numerical experiment is conducted, using an existing vertical dispersion framework and a field measurement data. Parameters used in the numerical experiment are chosen from this study and the final result is consistent with previously measured deposition velocity, for the first time.

The conclusion chapter summarizes the results of this study, including the wake model, the resistance model of the momentum transfer, the new drag and drag partition theory, the new deposition theory and the new understanding of intermittency and its influence on the deposition process. A comparison between 2D and 3D simulations including a summary of the advantage and disadvantage of 2D and 3D simulations is also made. The outlook for future studies suggests that we should extend the proposed models and evaluate more natural conditions

## Introduction

## 2. The wakes on rough surfaces

*Based on 2D simulations of air flow over rough surfaces*

### 2.1 Introduction

This chapter presents a two dimensional (2D) simulation of air flow over rough surfaces to study the flow pattern and the dimension of the wake behind roughness elements. The aim of this chapter is to associate the geometry of rough surfaces and the flow condition with the dimensions of the wakes, with one parameter. It serves as a theoretical preparation for the new drag and drag partition theory in the next chapter. With a better understanding of the pattern and dimension of the wake through numerical simulations, this parameter can be found and determined.

The starting point is to characterize the wake on surfaces mounted with roughness elements (Schlichting, 1936). And the study of the wake begins from analyzing the wake behind an isolated element (Raupach, 1992). In this chapter, both the flow over isolated elements and regularly distributed elements are simulated. The conditions with different height of elements and different roughness densities of elements are all considered.

A 2D RSM (Reynolds stress model) simulation can provide a reasonable mean wind field and the structure of the mean flow (Kim, 1989). Without disturbances from the spanwise components of the flow properties, 2D simulations produce a more steady and regular measurement of the wake than 3D simulations.

This chapter first introduces the 2D simulation in Section 2.2, and provides a visual interpretation of the wake on rough surfaces with isolated and regularly distributed roughness elements in Section 2.3 and 2.4, respectively. The figures of the flow fields and the wake behind isolated elements on rough surfaces are shown, and the lengths of the wakes are measured. Based on the result, a wake length model is proposed to address the relationship among the

wake dimensions, element sizes and reference wind speeds. The dependency of height-to-length ratio of the wake on the height of element and on the wind speed are determined. A function of the friction coefficient and length of wake is constructed in Section 2.4. Section 2.5 presents the wind profiles from the simulation result and deduces their parameters. Section 2.6 concludes this chapter.

## 2.2 Setup of the 2D Simulation

2D RSM simulations are conducted over rough surfaces. The simulations are conducted with the *Ansys Fluent* Software. The domain of the simulations is 300 mm × 150 mm. The geometry of the roughness element are two-dimensional rectangular. The boundary conditions are solid walls on the top and bottom surfaces, zero shear stress and a non-slip condition are used for them, respectively. Periodic condition are applied for the inlet and outlet. The standard Reynolds Stress Model and the standard wall function are used.

In the 2D simulation, there are 20 different wind speed and 13 different meshes that differ in density and the size of roughness elements; a total of 260 runs are conducted. The 2D simulation consists of two groups of runs, the first group examines the flow over an isolated roughness element of three different heights, i.e.,  $h = 5, 7.5$ , and 10 mm; the second group simulates flow over rough surfaces with uniformly distributed square roughness elements that had the same height, i.e.,  $h = 10$  mm. Hundreds of tests are conducted to determine the suitable grid size and the time step for all of the meshes with different rough surfaces. The objective is to get reasonable results while minimizing the consumption of computational power. Detailed data concerning the setup of these two groups are in Table 2.1 and Table 2.2, respectively. Figure 2.1 shows the simulation domain and part of the mesh on dense surface with  $\lambda = 0.67$  as an example. The simulation results are compared to classical wind tunnel measurements to be validated.

2D simulation on surfaces with isolated element (60 runs)																				
$u_r$ [ms <sup>-1</sup> ]	1	2	3	4	5	6	7	8	9	10	11	12	13	14	15	16	17	18	19	20
$h$ [mm]	5	7.5	10	$b/h$													1			
Domain [mm <sup>2</sup> ]	300*100										Time step [s]				0.002					
Grid size [mm]	0.1-0.5										Time length [s]				4					
Total grids	390,000-450,000										Viscous model				Reynold stress model					

Table 2.1 Parameters and options for the use of *Ansys Fluent* to simulate the 2D air flow over surfaces with isolated element.

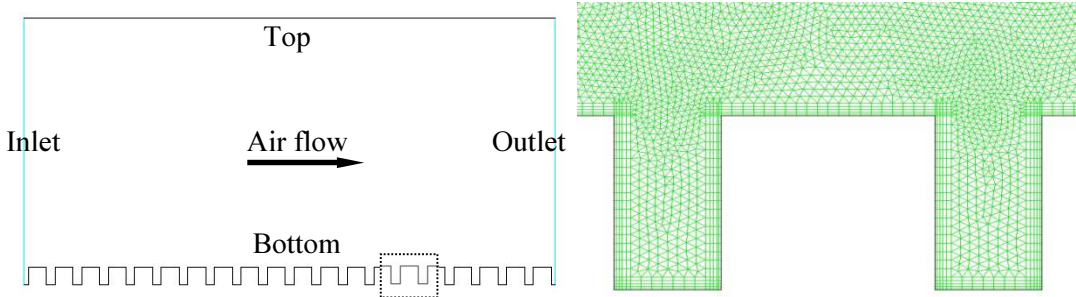


Figure 2.1 Domain of the simulation and the mesh used near the boundary of the dense rough surface with  $\lambda = 2/3$ .

2D simulation on rough surfaces (220 runs)																				
$u_r$ [ms $^{-1}$ ]	1	2	3	4	5	6	7	8	9	10	11	12	13	14	15	16	17	18	19	20
$\lambda$	1/30	1/15	1/10	2/15	1/6	1/5	7/30	1/3	2/5	1/2	2/3									
$h$ [mm]	10					$b/h$	1													
Domain [mm $^2$ ]	300*100					Time step [s]	0.002													
Grid size [mm]	0.1-0.5					Time length [s]	4													
Total grids	250,000-390,000					Viscous model	Reynold stress model													

Table 2.2 Parameters and options for the use of Ansys Fluent to simulate the 2D air flow over rough surfaces with uniformly distributed elements.

The range of  $\lambda$  in the simulation covers both dense and sparse surfaces. In Raupach's experiment (1980),  $\lambda$  is chosen in the range of 0.011 to 0.18, whereas O'Loughlin (1965) used  $\lambda = 1/256$ ,  $1/128$  and  $1/64$ . Marshall (1971) set the value of  $\lambda$  from 0.1 to 0.6 when  $b/h=1$ . Shao (2005) found that the peak drag occurs around when  $\lambda$  was in the range of 0.1 to 0.2. The criteria in the choice of the value of  $\lambda$  in this study was to cover the most of the range of the  $\lambda$  value has been used before. In all runs, the sizes of the domains are the same, and the dimensions of the elements are the same. The meshes of different  $\lambda$  allow successful calculation of the flow in all conditions with the same domain size and the minimum grid size. The total number of grids is also limited to a reasonable value.

The range of wind speed is also carefully chosen. The wind tunnel measurements of drag on a rough surface are usually conducted at high wind speeds, for example, the wind speed 20.3ms $^{-1}$  in Marshall's (1971) experiment and 17.5 ms $^{-1}$  in Raupach et al. (1980). Dust deposition experiments are generally focused on steady flow, and they consider a wide range of wind speeds, e.g., 1-20 ms $^{-1}$  in Chamberlain (1967). The range of used wind speed in this study covers most of those used in previous studies.

In the following sections, the simulated flow over surfaces with isolated roughness element and regularly-distributed, multiple roughness elements are presented. The measured drag and drag

partition are compared with experimental data or previous models to validate this simulation. The parameters of wind profile will be derived by regression analysis.

## 2.3 2D Flow over isolated elements

### 2.3.1 Results of 2D flow over isolated elements

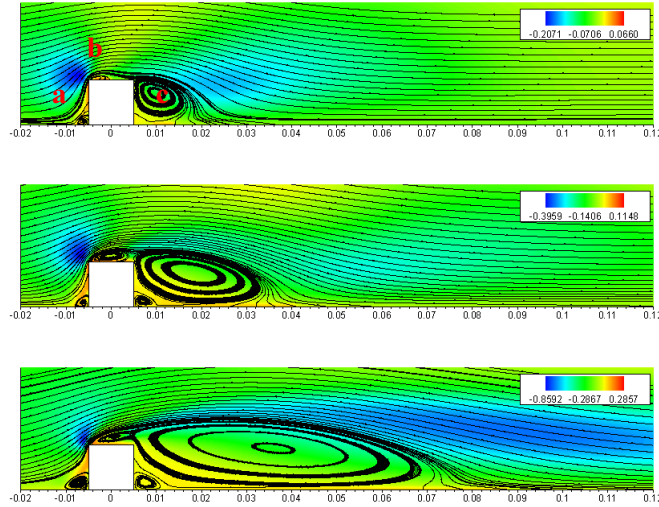


Figure 2.2 Flow over an isolated element, at  $u_r = 1, 2$ , and  $5 \text{ ms}^{-1}$ . Streamlines are shown in black lines. Color contour shows the magnitude of Reynolds stress. The front, top and back vortices are marked with  $a$ ,  $b$  and  $c$ , respectively

A series of simulations are conducted for flow over isolated roughness elements with different heights (see Table 2.1). The heights of the elements are 5, 7.5 and 10 mm. Figure 2.2 and Figure 2.3 show the cases in which  $h = 10 \text{ mm}$  under wind speeds of 1, 2, 5, 10, 15 and  $20 \text{ ms}^{-1}$ . The direction of flow in all the figures is from left to right.

There are mainly three vortices around the roughness element in Figure 2.2 and Figure 2.3, including the front vortex in front of the element, the top vortex on the top of element, and the back vortex behind the element. The front vortex is generally small and isolated from the other two vortices. In this study of 2D air flow, the focus is on the top and back vortices. The front vortex, then, is considered to be an accessory to the larger vortices and its dimension is not discussed in the following sections.

In Figure 2.2, for wind speeds less than  $10 \text{ ms}^{-1}$ , the top vortex and the back vortex are separated; in Figure 2.3, for the larger wind speeds, the two vortices overlapped, which means that the top and back vortices merged into a larger vortex.

The length of the wake is observed to be increasing according to the wind speed, and reaches a constant as the wind speed exceeds a threshold, which is defined as  $u_a$ . From Figures 2.2 and Figures 2.3, as the wind speed increases, the absolute Reynolds stress near the front edge of the element increases (See legend of Figures 2.2 and Figures 2.3), and the flow bursts into the layer above the element with higher momentum. This upward shear flow is against the direction of

downward momentum transfer and dampens the momentum transfer. With larger dampening, the upwards motion of the burst of flow is limited and the flow sweeps downwards at a limited distance away from the element. As a result, this distance increases as wind speed increases. After the wind speed has reached a threshold, the upwards and downwards shear flow become equivalent. This is how the size of a wake respond to wind speed. However, the threshold wind speed  $u_a$  and the length of the wake cannot be directly acquired from Figure 2.2 and Figure 2.3. The length of wakes and  $u_a$  is determined in Section 2.3.3.

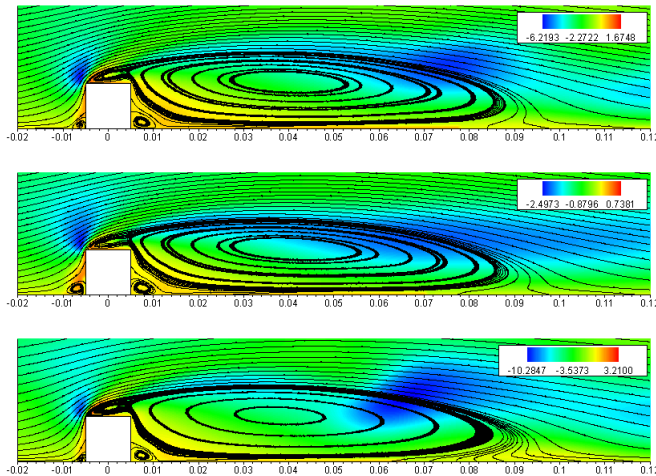


Figure 2.3 Flow over an isolated element, at  $u_r = 10, 15$  and  $20 \text{ ms}^{-1}$ , respectively.

Streamlines are shown. Color contour shows the magnitude of the Reynolds stress

To quantify the dimension of the wake, a distance from the back of the roughness element to the end of the wake,  $l_w$ , is used. The end of wake behind a roughness element is quantitatively the point of zero shear stress. The wake regions behind the elements are bounded by strong shear layers in which the local vorticity value are high. At the end of the wake, a strong shear layer reattaches the bottom surface, this point is called the reattachment point.

Note that, in the series of diagrams in Figure 2.2 and Figure 2.3, the densities of the streamlines are chosen randomly to show the details of the wakes. The number of streamlines is not strictly related to the velocity or the velocity gradient. The velocity of the flow is shown as wind profiles in Section 2.5.3.1.

### 2.3.2 Discussion on the types of wakes

To study the flow over rough surfaces in a deep ambient turbulent flow, the surfaces are traditionally simplified as a flat surface with roughness elements. The existence of a substrate surface and the turbulence in the ambient boundary layer make it complex and difficult to use a simple, integral momentum relationship (Batchelor, 1970; Lighthill, 1975). Therefore, it is necessary to understand the structure of flow quantitatively. It is useful to study the wake behind the elements, in the quasi-laminar roughness layer to relate the surface geometry to the momentum transfer.

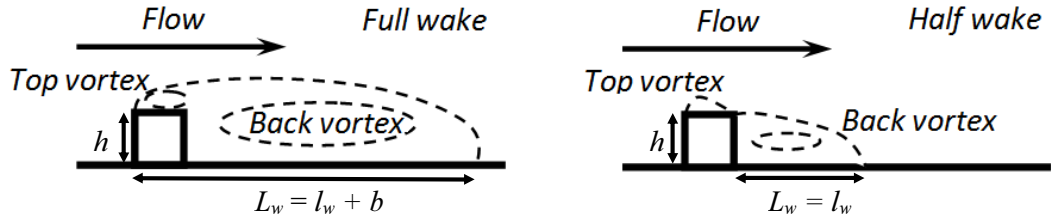


Figure 2.4 Dimensions of the element and the wake. On the left, when wind speed is larger, the wake is a full wake with overlapped top vortex and back vortex; On the right, when the wind speed is smaller, the wake is a half wake with a back vortex and an isolated top vortex.

Figure 2.4, shows the vortices and the two types of wakes that can be observed in 2D simulation from Figure 2.2 and Figure 2.3. A full wake covers both the top and back vortices, it is found behind an isolated element when the shear flow generated from the front edge of the element is strong enough to cover the back vortex; a half wake only covers the back vortex, it is found on the surface with an isolated element at smaller wind speeds, and the induced shear flow is not strong enough to cover both of the vortices.

The main reason for the difference in the two types of wakes is the difference in the strength of the shear flow. And the strength of the shear flow is subject to velocity  $u_h$  and  $u_r$  (Finnigan, 2000; Raupach, 1992). Therefore, a threshold of  $u_h$  or  $u_r$  can be found to distinguish the two type of wakes and flow, and  $L_w$  can be used to determine the change of flow conditions. Thus, an argument for the size of the full wake and the half wake is proposed here:

When the flow is blocked by the element, the flow below height  $h$  must move upward before it collides with the element. Since the momentum is assumed to be transferred from the upper layer to the lower layer, it is reduced when the upward moving flow encounters the upper layer flow. Visually, the flow will then be pushed downward and reattach the substrate. After a certain distance, the logarithmic profile will be restored. A part of the momentum is transferred to the element and the surface or is consumed by keeping the vortices rotating. These consumed momentum is related to the strength of the shear flow and the surface drag. When this momentum is low, the shear flow that induced by the element will be too weak to cover that top of element, and the top and back vortex are separated. When this momentum is high enough, the shear flow will extend over the end of the element, and the top vortex will merge into the back vortex. Meaning that the strength of shear flow are different, when the wake appears as a full wake or a half wake. Consequently, the length of wake is related to surface drag, the strength of shear flow and they are different for the two types of wakes.

Figure 2.4 (a) and (b) shows the dimensions of the element and the effective area of the wake. The length and the width of all the 3D elements in this thesis are equal to  $b$ . The half wake starts from the back of element to the reattachment point; and the full wake starts from the front of the element to the end of element. Their common expressions with  $l_w$ ,  $h$  and  $u_a$  is:

$$L_w = \begin{cases} l_w & u_r < u_a \\ l_w + b & u_r \geq u_a \end{cases} \quad (2.1)$$

As the length of wake behind isolated element is dependent on wind speed, the following two sections analyze the results of the length of wake and mathematically determines the dimension of the full wake and the half wake as functions of wind speed, based on the simulation result.

In the existing theory, the size of a wake behind an element is equivalent to the size of the sheltering area. Traditionally, it is assumed that the size of a wake is related to the friction coefficient (Raupach, 1992). The area and volume of sheltering area is correspond to the area and the volume of wake. The area and the volume of the sheltering area were defined as  $A = bl_w = cbhu_h/u_*$ , and the volume is  $V = bhl_w = cbh^2u_h/u_*$  (Raupach, 1992), where  $h$  is the height of the element,  $l_w$  equals to the length of the sheltering area, and  $c$  is a constant. These definitions imply that:

$$\frac{u_*}{cu_h} = \frac{h}{l_w} \quad (2.2)$$

The height-to-length ratio of the wake is defined here as  $\lambda_w$ :

$$\lambda_w = \frac{h}{l_w} \quad (2.3)$$

These definitions imply that the wake is considered as half wake in existing theory. Therefore,  $\lambda_w$  is related to drag.

However, as the shape of wake is steady in the mean flow, the strength of shear flow on the top and on the bottom of the wake must be balanced. Which means: for a full, the strength of shear flow on the element is equivalent with that on the underlying surface. This is useful that, for dense surface, when the distance between elements is the same as the length of wake behind isolated element, the strength of shear flow on the wake is the same as on the underlying surface. Therefore, the strength of shear flow on the element and on the underlying surface are equivalent, if the shape of the wake steady, when  $\lambda_w = \lambda_a$ .

### 2.3.3 Result on the length of wakes

Result of simulations on surface with isolated elements with heights of 5, 7.5 and 10 mm under 20 different wind speeds are used to analyze the influence of  $h$  and  $u_r$  on  $L_w$ . The total shear stress decreases to zero directly behind the element, and then it increases as the wake develops along the streamwise direction. Near the end of wake the intensity of the total stress decreases, and the end of wake can be determined by the point at which there is zero shear stress, as shown in Figure 2.5.

Note that, the flow which exits from the outlet reenters the domain from the inlet as periodic conditions are applied at the inlet and outlet. The total shear stress recovers when the distance behind the element is 15 to 20 times the height of element, at the highest wind speeds. This proves that the shear flow has little influence on the incoming flow, and a surface with  $\lambda = 1/30$  can be taken as the surface with isolated element. Figure 2.6 show the results of the length of the wakes as a function of wind speed based on Equation 2.1.

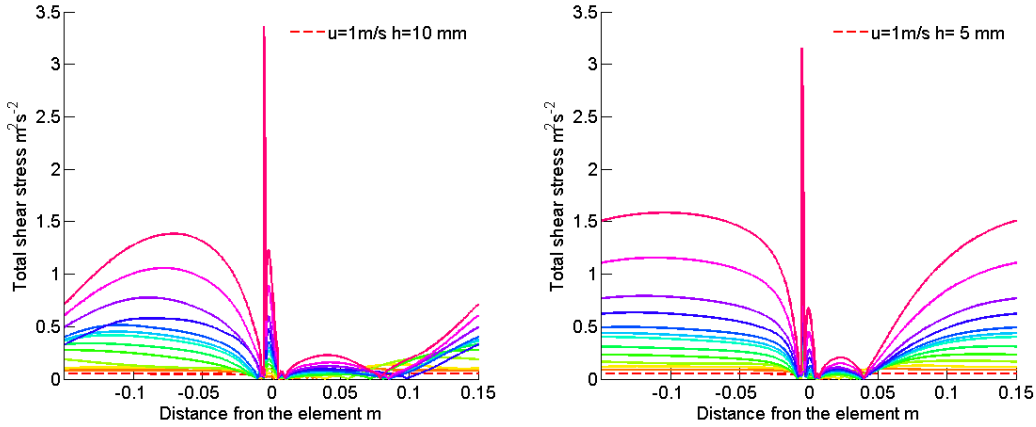


Figure 2.5 Total shear stress on the surface with isolated elements of 10 mm-high and 5 mm-high at wind speeds of 1-20  $\text{ms}^{-1}$ . The abscissa is the distance from the center of the roughness element, different colors marks the total shear stress under different wind speeds. As the wind speed increases, the total shear stress increases and the color changes from red to pink. The data of  $u = 1 \text{ ms}^{-1}$  are marked with dashed line.

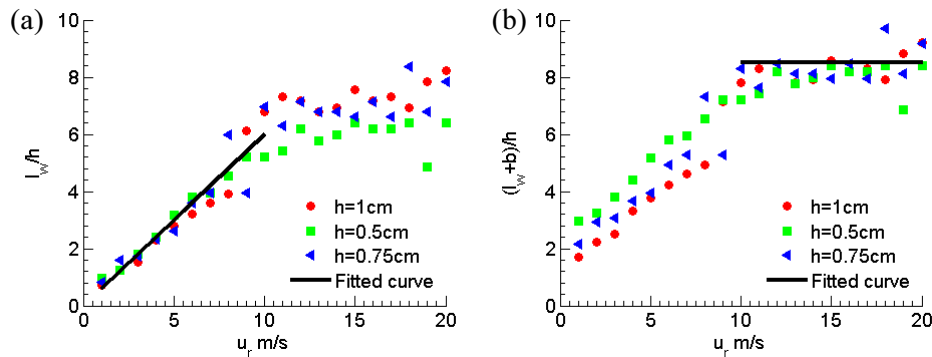


Figure 2.6 (a)  $l_w/h$  and (b)  $(l_w+b)/h$  from the 2D simulation data and the fitted curve. The length of wakes are best fitted as half wakes when  $L_w = l_w$  for  $u_r < 10 \text{ ms}^{-1}$ , and as full wakes when  $L_w = l_w + b$  for  $u_r > 10 \text{ ms}^{-1}$ . These figures prove that the height-to-length ratio of the wake is independent from the height of element.

In Figure 2.6, the data points show the tendency of the length-to-height ratio of the wake increasing as wind speed increases, and reaching a plateau at about  $u_a = 10 \text{ ms}^{-1}$ . With a piecewise function for  $u_r < u_a$  and  $u_r > u_a$ , it is possible to fit these data points, for full wake and half wake, respectively.

The data of  $(l_w+b)/h$  when  $u > u_a$  and the data of  $l_w/h$  when  $u < u_a$  are well fitted by the Equation (2.4) and (2.5). The suitable functions for the curve of length-to-height ratio of half wakes in Figure 2.6(a) is:

$$\frac{L_w}{h} = \frac{l_w}{h} = 0.6u_r \quad u_r < u_a \quad (2.4)$$

And the suitable function for the curve of the length-to-height ratio of full wakes in Figure 2.6(b) is

$$\frac{L_w}{h} = \frac{l_w + b}{h} = 8.5 \quad u_r \geq u_a \quad (2.5)$$

The result of fitting proves that the definition of the full wake and the half wake are reasonable, they can be distinguished by threshold wind speed  $u_a$ , and their length-to-height ratios are independent from  $h$ .

The dependency of the ratio of length of wake on the wind speed is consistent with the type of wake changing with wind speed. And the length of wakes are:

$$L_w = \begin{cases} 0.6u_r h & u_r < u_a \\ 8.5h & u_r \geq u_a \end{cases} \quad (2.6)$$

The next section will discuss this result and its application on dense surfaces.

### 2.3.4 Discussion on the length of wakes

Figure 2.4 shows the top and the back vortices as well as the full and the half wakes behind an isolated element. Figure 2.2 and Figure 2.3 show the images of the wakes behind the isolated elements. Figure 2.6 shows the result of the length of the wake. The measured lengths of the wakes are Equation (2.6) and its common form is in Equation (2.1).

From these results of the 2D simulation, it can be concluded that,

- (a) When  $u_r < u_a$ , the wake is a half wake, the top vortices separates from the back vortices;  $l_w/h$  is the best fit for the  $L_w/h$  for all heights; and  $L_w/h$  is proportional to wind speed.
- (b) When  $u_r \geq u_a$ , the wake is a full wake, the top vortices merges with the back vortices;  $(l_w + b)/h$  is the best fit for the  $L_w/h$  for all heights; and  $L_w/h$  is constant for all wind speed.

Therefore, it is reasonable to assume that the sizes and types of the wake behind isolated element depend on wind speed, rather than the height of element. For convenience, to compare the dimension of the wake to roughness density of surfaces, here we determine the height-to-length ratio of the wake, as:

$$\lambda_w = \frac{h}{L_w} = \begin{cases} \frac{1}{0.6u_r} & u_r < u_a \\ \frac{1}{8.5} & u_r \geq u_a \end{cases} \quad (2.7)$$

Equation (2.7) is valid for all surfaces with isolated elements, it means that:

The height-to-length ratio of the wake ( $\lambda_w$ ) behind a roughness element is independent from the height of element ( $h$ ).

or

The length of wake ( $L_w$ ) is proportional to the height of element ( $h$ ). The length of wake increases as the element height increases.

With this result, it is possible to associate the strength of the shear flow over a rough surface with the geometrical characteristic of the wake. And with another conclusion, the characterization of the wake needs only one constant for surfaces with identical elements:

The height-to-length ratio ( $\lambda_w$ ) of the wake is a constant when the wake is a full wake and it is dependent neither on the wind speed ( $u_r$ ) nor the height of element ( $h$ ).

This conclusion is important to determine the dimension of wake for flow over rough surfaces for both 2D and 3D cases. It means that a uniform height-to-length ratio of the full wake can be used to represent the flow pattern, regardless of the  $u_r$  and  $h$ . And, as  $\lambda_w$ , is not dependent on  $h$ , and it is also more reasonable to use  $\lambda = b/l$  to distinguish the surfaces rather than  $h/l$ . These conclusions will be used in the new drag and drag partition theory. The next step is to associate the roughness density with  $\lambda_w$ .

Note that, in the simulation, the profile is the same as the logarithmic profile on the smooth surface before the air flow encounters the isolated roughness element. This means that the velocity above the surface follows logarithmic law as in Equation 1.10. Where  $u_h$  is proportional to the  $u_r$ . On rough surface,  $u_h$  can replace  $u_r$  and act as the reference velocity. In this way, it is easier to discuss the wake and shear flow on the surface. The next section, present the simulation results from the 2D simulation and introduce the study of wake on rough surface.

## 2.4 2D Flow over regularly-arranged rough surfaces

### 2.4.1 Results of 2D flow over rough surfaces

Figure 2.7 shows the flow over rough surfaces, under wind speed of  $20 \text{ ms}^{-1}$ . The streamline shows clearly the wake and the flows of each layer. The background color is the contour of the Reynolds stress. Both the full wake and the half wake are evident in these Figures.

The full wakes are found mainly on the surface with isolated elements, and half wakes are found on denser surfaces. From the contour of the Reynolds stress, it is observed that the sparser surfaces have smaller value of the negative Reynolds stress, and this value increases as roughness density increases (see the legends in Figure 2.7). The nadir of Reynolds stress occurs in front of each element. The velocity on the surface of the element must be zero, therefore the velocity gradient and the magnitude of absolute Reynold stress is proportional to  $u_h$ . This means that the velocity gradient near the front edge of each element and  $u_h$  both decreases as  $\lambda$  increases. When  $u_r$  becomes smaller than  $u_a$ , as discussed in previous section for isolated element, the wake transforms from a full wake into a half wake. Therefore, the distribution of the Reynolds stress can be another criterion for determining the type of wake and explains the transform of the wakes.

Figure 2.7 also shows that, a wake behind an element shelters an area on the adjacent downstream element, leaving only a certain height of the element exposed to the flow. This remaining height is the height of the restrained wake, i.e.,  $h_w$ , and it decreases as the surface becomes denser. This phenomenon is consistent with present knowledge (Macdonald et al., 1998b; Shao & Yang, 2008). The larger the distance between the elements, the higher  $u_h$ , the

higher shear stress, the larger wake, and larger  $h_w$ . The functions which describe these relationship are discussed in the next section.

Note that, although  $h_w$  can be seen in Figure 2.7, it is very difficult to measure its value directly with acceptable accuracy.  $h_w$  will be used in expression of the length of the wake to address the sheltering effect and its result on the dimensions of the wake.

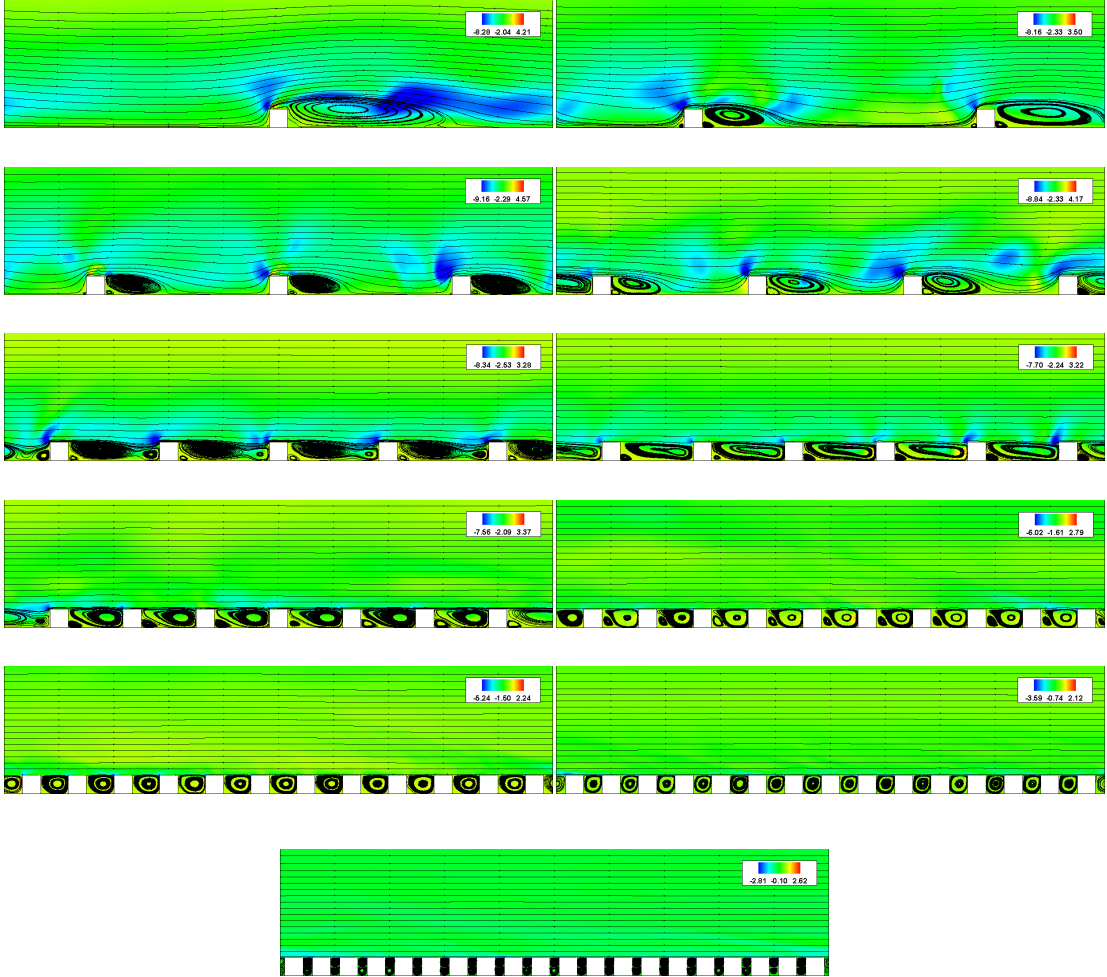


Figure 2.7 Flow over rough surfaces from the simulation results: the height of the element is 10 mm. The background color represents the contour of Reynolds stress [ $\text{m}^2\text{s}^{-2}$ ], and the black curves are the streamlines. The wind speed is  $20 \text{ ms}^{-1}$ .

## 2.4.2 The model of wake on rough surfaces

To address the measure the heights of wakes on dense surfaces,  $h_w$  is used to replace  $h$  in the expression of  $L_w$  and  $\lambda_w$ .  $h_w$  is related to the geometry of the surface. The definition of the parameters for the wake are shown in Figure 2.8.

(a) Two types of wakes on rough surfaces, on sparse and dense surfaces.



(b) Effective dimensions of the wakes.

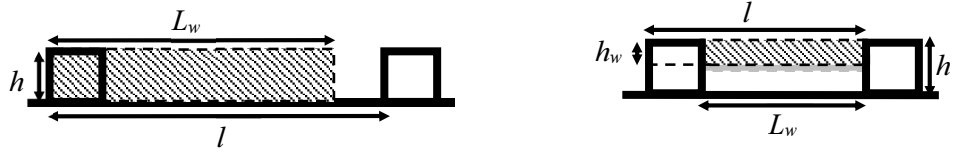


Figure 2.8 Dimension of the wake on rough surfaces. On the left, sparse surface with  $\lambda_w = h/L_w$ ; On the right, dense surface with  $\lambda_w = h_w/L_w$ .

From the result of 2D simulation, the wake is half wake on dense surface and full wake on sparse surface. Therefore, according to Figure 2.8,  $L_w$  can be written as:

$$L_w = \begin{cases} l_w + b = 8.5h & \lambda \leq \lambda_a \\ l_w = 0.6u_r h_w & \lambda > \lambda_a \end{cases} \quad (2.8)$$

This is the expression for the length of wake on rough surfaces for 2D cases.

If the hypothesis of Raupach (1992) also worked on the sheltering of wake on dense surface, and the  $\lambda_w$  was determined by wind speed, i.e.  $u_r$  or  $u_h$ . Then variation of Equation (2.2) on rough surface is

$$\frac{u_*}{cu_h} = \frac{h_w}{L_w} = \begin{cases} \frac{h_w}{8.5h}, & \lambda \leq \lambda_a \\ \frac{1}{0.6u_r}, & \lambda > \lambda_a \end{cases} \quad (2.9)$$

As it is discussed in previous sections: on sparse surface  $L_w < l$ ,  $h_w = h$ ; on dense surface  $L_w = l$ ,  $h_w < h$ . Therefore we have:

$$\frac{u_*}{cu_h} = \begin{cases} \frac{\lambda_w}{8.5\lambda} & \lambda \leq \lambda_a \\ \frac{1}{0.6u_r} & \lambda > \lambda_a \end{cases} \quad (2.10)$$

This equation means that: on sparse surface, the friction coefficient is proportional to  $\lambda_w/\lambda$ ; one dense surface, the friction coefficient is independent of  $\lambda$  and  $\lambda_w$ . This conclusion is useful for the argument of the difference of shear flow over 3D and 2D elements. As there are empty streamwise aisles between the aisles of element on surface with 3D elements, these surfaces are sparser than surfaces with 2D elements, when they have equal  $b/l$ . Therefore, the difference between the friction coefficient of surface with 2D and 3D elements may also be a factor of  $\lambda_w/\lambda$ . And when  $\lambda_w$  is constant, this factor become  $\lambda_a/\lambda$ . This relationships will be further discussed and used in the next chapter for the new drag and drag partition theory

Following Equation (2.10), since  $u_h$  generally decreases as  $\lambda$  increases, then a simple relationship between the  $u^*$  and  $u_h$  can be determined:

$$u_* = \begin{cases} \frac{c\lambda_w u_h}{8.5\lambda} & \lambda \leq \lambda_a \\ \frac{cu_r u_h}{0.6} & \lambda > \lambda_a \end{cases} \quad (2.11)$$

Raupach (1992) had chosen  $c = 0.37$ . As  $u_h$  may change as the roughness density changes. With an expression of  $u_h$  as a function of roughness density and dimension of the wake, the drag can be associated with the property of the surface and wind speeds, and expressed as a function of only  $u_r$ ,  $u_h$ ,  $\lambda_w$ , and  $\lambda$ . However,  $u_h$  is difficult to be determined for both experiment and simulation. Constants were used for  $u_h$ , and it was generally not independently determined (Brown et al., 2008; Raupach, 1992; Walter et al., 2012a). Note that Equation 2.11 is also based on the first hypothesis of Raupach (1992) and the 2D simulation results of this thesis. However, it is not an aim of this thesis to validate previous hypothesis. Therefore, only the main findings of the wake study in Section 2.3 is carried on to the new drag and drag partition theory.

In the next Chapter, a resistance method is used to estimate the momentum flux on surface. That method deduced the resistances and associate the drag with the maximum drag on surface, then it is not necessary to deduce  $u_h$  or the strength of shear flow. A new physical model of drag and drag partition is also presented to estimate the drag by a geometric method. The theoretical results of the wake in 2D cases are applied in 3D study of the flow over rough surface. And  $\lambda_a$  is used as the parameter for the flow condition. As it is independent from element height and independent from wind speed for full wakes, according to findings of this study of wakes.

The parameters of the flow and surface drag in 2D simulations are summarized in the next section.

## 2.5 Parameters of 2D air flow over rough surface

### 2.5.1 Friction coefficient

Figure 2.9 shows the simulated data of  $c_d$ , on rough surfaces, for a total of 220 runs, with  $\lambda$  ranging from 0.033 to 0.67 for 20 different wind speeds with elements of  $b/h = 1$ . The data from previous wind tunnel experiments and field measurements are also shown as a comparison (Garratt, 1977; Jarvis et al., 1976; Raupach et al., 1980).

For convenience, here we define a roughness density of surface with maximum drag, as  $\lambda_m$ . In Figure 2.9, at higher wind speeds,  $u^*/u_h$  increases as  $\lambda$  increases when  $\lambda$  is smaller than  $\lambda_m$ , and decreases as  $\lambda$  increases when  $\lambda$  is greater than  $\lambda_m$ ; at lower wind speeds, i.e., less than  $5 \text{ ms}^{-1}$ , the peak value of  $u^*/u_h$  moves to the larger  $\lambda$ ; As wind speed increases,  $u^*/u_h$  decreases.

To allow a successful comparison, the roughness density are taken as  $\lambda = b/l$  for both the 2D simulation and the experiment data (Figure 2.9). The experiment data scattered over a range of 0 to 0.67. The experimental data include measurements that were made in wind tunnels and in the field (Garratt, 1977; Jarvis et al., 1976; Raupach et al., 1980). It was not possible to control the wind speed in the field experiments. Thus, the average of  $c_d$  for 20 different wind speeds

for each  $\lambda$  (blue curve in Figure 2.9) are calculated for a comparison with the experimental data (black triangles in Figure 2.9) and Raupach (1992)'s estimation (red curve in Figure 2.9). Beside the results that were obtained with a large  $\lambda$ , i.e.,  $\lambda = 2 / 3$ , the simulation results fit the experimental data quite well.

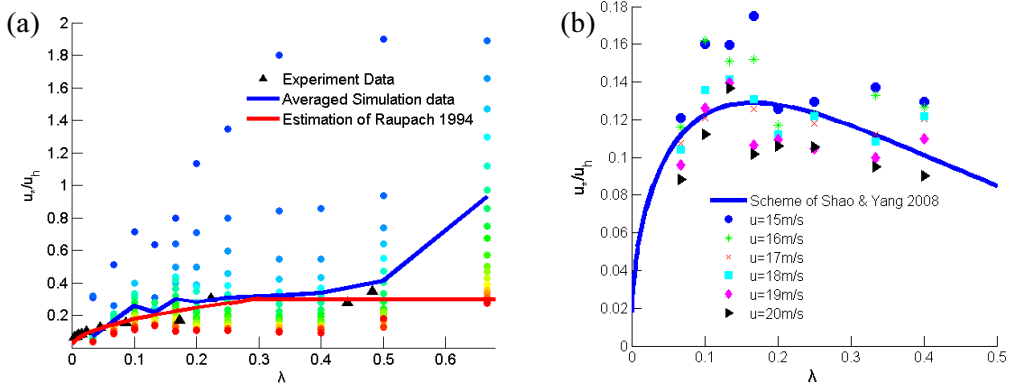


Figure 2.9 (a) Friction coefficient ( $c_d = u^*/u_h$ ) as function of  $\lambda$  at 20 different wind speeds; different wind speeds are distinguished by the color that range from blue to red as the wind speed increases from 1 to 20  $\text{ms}^{-1}$ ; and the mean value of  $c_d$  for all of the wind speed versus  $\lambda$  is plotted (blue curve). The black triangles represent experimental data, red curve is the estimation of Raupach (1992). (b) Simulation data of  $c_d$  at wind speeds of 15, 16, 17, 18, 19 and 20  $\text{ms}^{-1}$ , compared with the estimation of Shao and Yang (2008)

The scheme proposed by Shao and Yang (2008) was based on the theory of Raupach (1992), and it is a variation of the drag model. Shao and Yang's (2008) and Raupach's (1992) scheme agreed well the same wind tunnel measurements on sparse surfaces at high wind speeds. As the scheme of Shao and Yang (2008) does not specify the wind speed, data of wind speeds of 15 to 20  $\text{ms}^{-1}$  are used to show the detail of friction coefficient changing with wind speed, and compared with the model of Shao & Yang (2008). The simulated data for high wind speeds are consistent with those provided by Shao's (2008) scheme. They both show a peak in the range of 0.1 to 0.2. However, 2D simulation is different from 3D simulation, parameterization of  $c_d$  is only applied for 3D simulation data.

### 2.5.2 Drag partition $\tau_r/\tau$

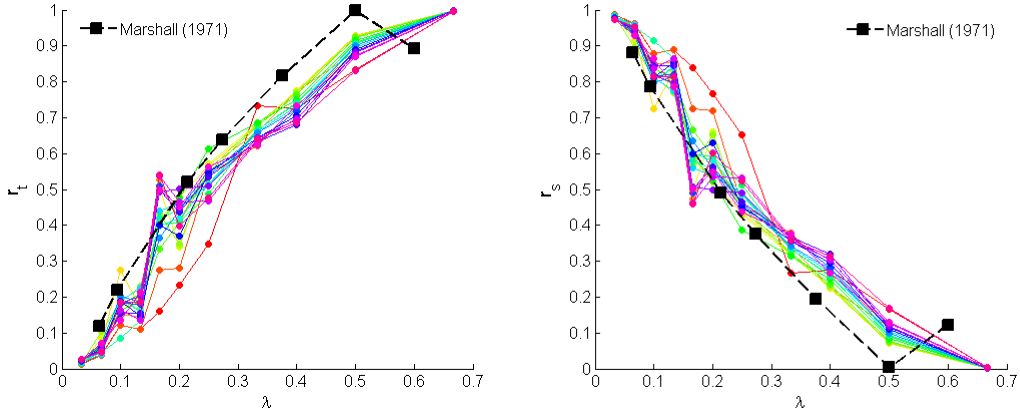


Figure 2.10 Comparison for  $r_r$  and  $r_s$  values from Marshall's (1971) experimental data (marked with squares and dashed lines), with  $b/h=1$ , with our simulation data (marked with solid circle and straight line). The values are plotted on the abscissa of  $\lambda$ . The results for 20 different wind speeds are shown, they are very close to each other, and marked with colors. When wind speed increases from  $1 \text{ ms}^{-1}$  to  $20 \text{ m/s}^{-1}$ , the color of the data changes from yellow to pink.

Figure 2.10 shows  $r_r$  and  $r_s$  from the simulation. The partition functions of the drag on the element and of the drag on the underlying surface are defined as

$$r_r = \frac{\tau_r}{\tau}, \quad r_s = \frac{\tau_s}{\tau} \quad (2.12)$$

where  $\tau_r$ ,  $\tau_s$  and  $\tau$  are shear stress on the roughness element, shear stress on the underlying surface and total shear stress, respectively.

The simulation results are also compared with the experimental data of Marshall (1971) with  $b/h = 1$ , in Figure 2.10. Simulation results of partition of drag on elements and surfaces are consistent with the experimental results. The simulations are conducted using the wind speeds in the range of 1 to  $20 \text{ ms}^{-1}$  and the wind speed used in Marshall's (1971) experiment was  $20.3 \text{ ms}^{-1}$ .

The experimental data and simulation data show the same trend for  $\lambda$  in the range from 0 to 0.5, when  $r_r$  increases as  $\lambda$  increases and  $r_s$  decreases as  $\lambda$  increases (Brown et al., 2008; Musick & Gillette, 1990; Raupach, 1992; Shao & Yang, 2005; Shuttleworth et al., 1984; Walter et al., 2012). A small difference exists for  $\lambda = 0.6$ , when the  $r_r$  value from the experimental data is about 0.1 smaller than  $r_r$  at  $\lambda = 0.5$ . This is a systematic error in the measurement due to high density of the roughness elements (Marshall, 1971). Therefore, it is proven that this 2D numerical simulation provided reasonable data of drag partition, and it is validated by widely-accepted experimental data.

## 2.5.3 Wind profile over rough surfaces

### 2.5.3.1 2D Simulation results of the wind profile

The wind profile is important for describing the air flow in the boundary layer and for estimating momentum flux (Prandtl, 1963; Schlichting, 1936; Stull, 1988). Due to the shear flow induced by the element, the wind profiles on a rough surface differ from each other when the roughness density changes.

On sparse surface, the wind profile are similar to the wind profile on a smooth surface. On a rough surface, the interval between elements is smaller, and results in a reduction of wind speed in the roughness layer. The wind speed in the roughness layer approaches zero, and the wind speed in the inertial layer decreases as the roughness density increases.

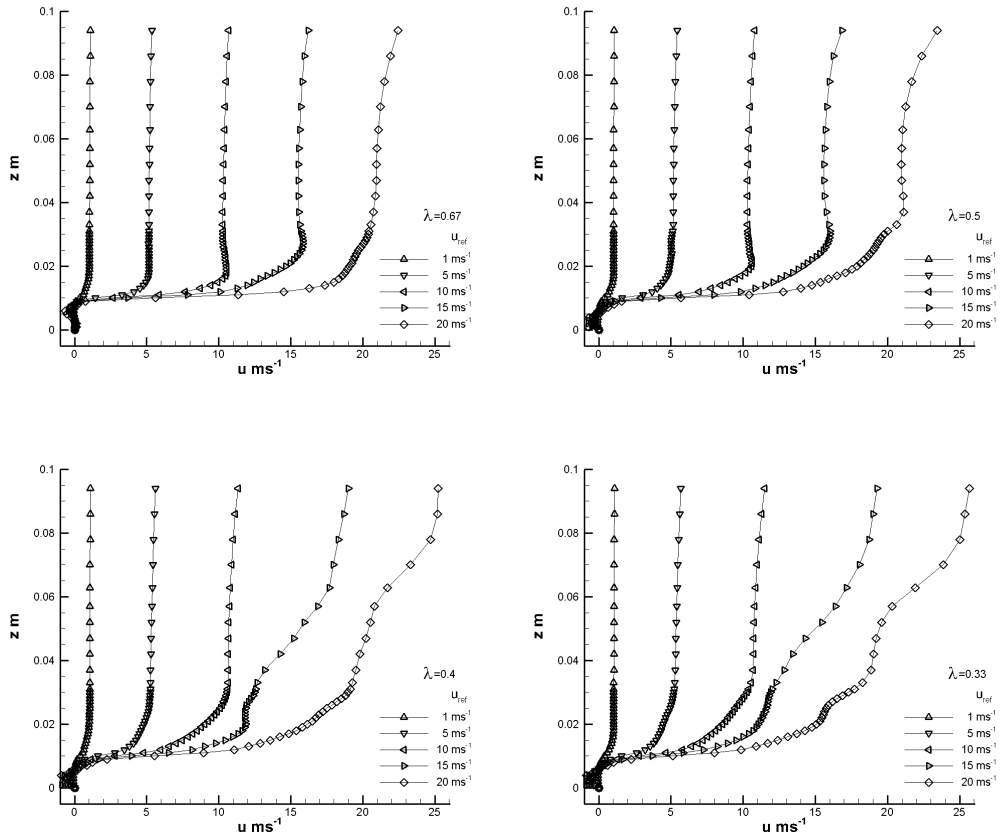


Figure 2.11 Wind profile of flow over 4 different regularly arranged rough surfaces.

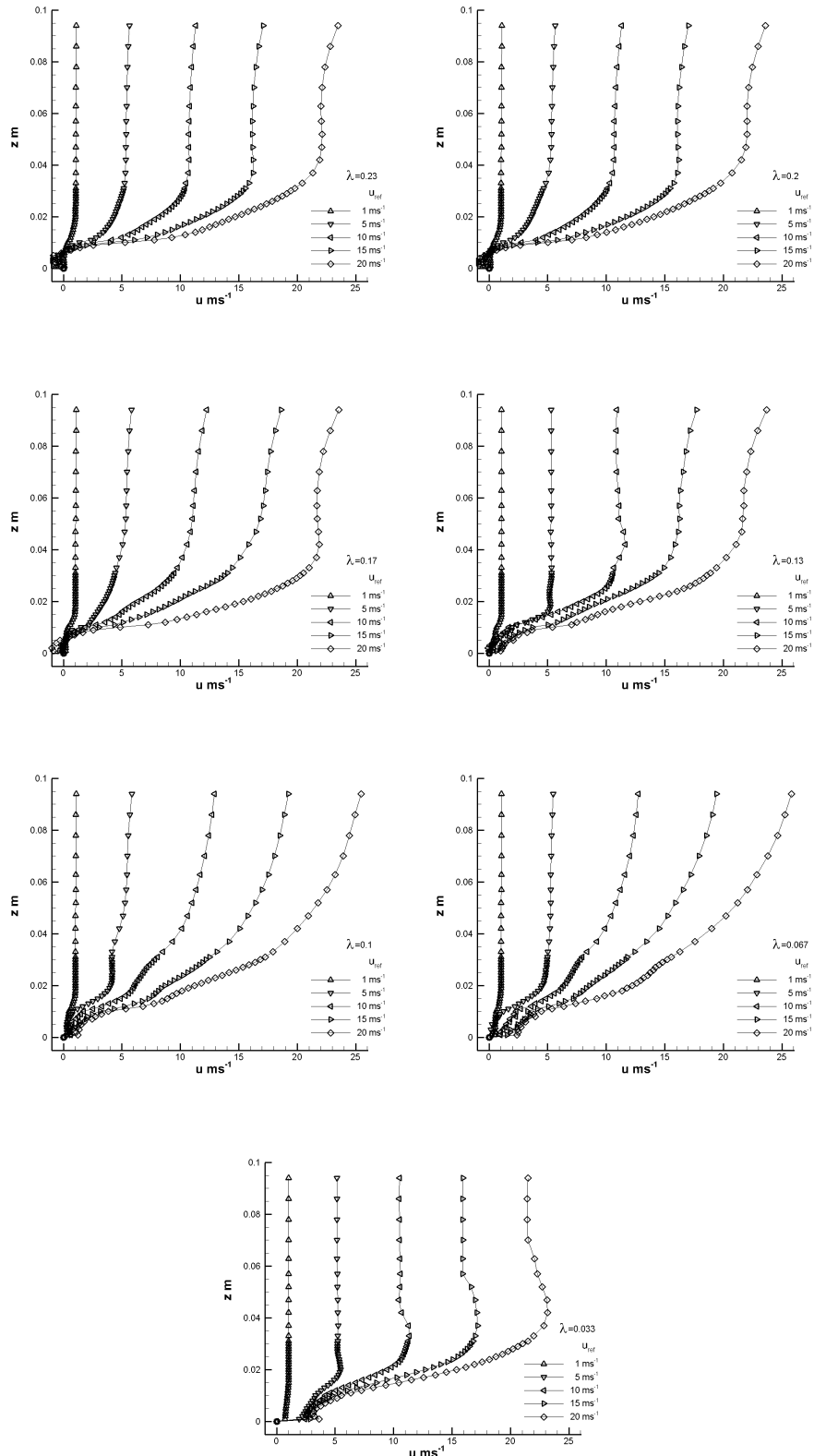


Figure 2.12 Wind profile of flow over 7 different regularly arranged rough surfaces.  
Each diagram corresponds to a surface distinguished by  $\lambda = b/l$ . Each curve represents one wind profile under a wind speed.

Wind profiles from simulation are acquired by the average of the velocity for each height across the whole domain. Figure 2.11 and Figure 2.12 show the velocity profiles for 11 different rough surfaces and 5 wind speeds as examples of the entire 2D data set. In the following sections, for all the curves that are shown, these profiles are fitted with the corrected logarithmic wind profile, as in Equation (1.14), to deduce the following parameters.

### 2.5.3.2 Determine $d/h$ and $z_0/h$ in 2D simulation

The wind profiles in the simulation are fitted with corrected profile of Equation 1.14. The wind profile above  $z_w$  and under  $z_w$  are fitted with a Logarithmic curve and a straight line, respectively:

$$\begin{cases} \ln(z) = a_1 u^+ + b_1, & z \geq z_w \\ z = a_2 u^+ + b_2, & z < z_w \end{cases} \quad (2.13)$$

where  $u^+ = u/u^*$  is a non-dimensional velocity. The fitting process begins with choosing of an appropriate range of  $z_w$  according to previous works (Table 1.1) and the flow conditions shown in Figure 2.7. The fitting of wind profiles are repeated many times until reasonable  $z_w$  are found for all conditions, and the correlation coefficients of the fittings are larger than  $R^2=0.9$ .

The  $d/h$  is acquired by calculating the height at which the logarithmic wind profile extended to the zero plane. Figure 2.13 shows the results of  $d/h$ . The fitted data of  $d/h$  at wind speed greater than  $u_r = 1 \text{ ms}^{-1}$  are close to each other, while  $d/h$  is smaller for  $u_r = 1 \text{ ms}^{-1}$ .

As discussed in section 2.5.1 and shown in Figure 2.2 and Figure 2.3, the wake behind each element does not develop fully at low wind speeds. The average velocity inside the wake is zero, and the structure of this eddy is intact and no mass exchange between the flow inside and outside of the wake. Consequently the size of the wake is related to the height of zero velocity plane. When the canyon layer are filled with wakes, the  $d$  will be pushed upwards and shows the trend in Figure 2.13.

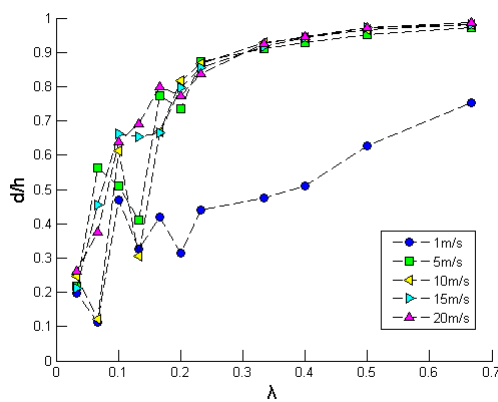


Figure 2.13  $d/h$  of the simulation data for wind speeds of 1 , 5 , 10, 15and 20  $\text{ms}^{-1}$ .

Comparing the  $d/h$  in Figure 2.13 to the height of sheltered height on the front edge of elements in Figure 2.7. Even below the zero displacement height  $d$  or sheltered height, there are wake between the elements. And the wind speed in Figure 2.11, below the height  $d$  determined in

Figure 2.13 is negative for a dense surface ( $\lambda > \lambda_a$ ) and positive for sparse surface ( $\lambda < \lambda_a$ ). These phenomena mean that, although  $d$  is defined as the height of zero-displacement, the value of average velocity at  $d$  does not have to be zero. It is an equivalent height of the zero-plane of the logarithmic profile that has been pushed upwards due to the existence of the roughness layer. The wake and the flow over the wake make the average velocity has a non-zero value at  $d$ .

In Figure 2.14, the  $z_0/h$  values in the 2D simulation are acquired by (Macdonald et al., 1998b):

$$\frac{z_0}{h} = \left(1 - \frac{d}{h}\right) \exp\left(\frac{\kappa}{u_*} u_h\right) \quad (2.14)$$

Both  $d/h$  and  $u_h/u_*$  are obtained in the preceding sections.

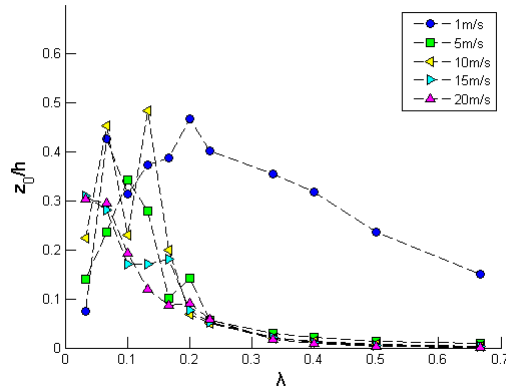


Figure 2.14 Values of  $z_0/h$  using simulation data for wind speed of 1, 5, 10, 15 and  $20 \text{ ms}^{-1}$ .

The result of  $z_0/h$  shows peaks between  $\lambda = 0$  and  $\lambda = 0.3$ . When wind speed increases, the peak shifts to the left side. The trend of  $z_0/h$  is different from experiment nor 3D simulations. Only the 3D simulation data will be used to validate the new theory, thus here do not further discuss this result of  $z_0/h$ .

### 2.5.3.3 Determine $z_w/h$ and $u_{zw}$ in 2D simulation

The  $z_w$  is defined as the height below which the wind profile is disturbed by wake diffusion. And the logarithmic wind profile begins at this height. Raupach (1992) expressed  $z_w$  as

$$z_w - d = c_w(h - d) \quad (2.15)$$

where  $c_w$  is a constant, value of which can be chosen from 1 to 4 (Shao & Yang, 2005). In the simulation,  $z_w$  is deduced as:

$$z_w = \frac{1}{a_2 \kappa} + d \quad (2.16)$$

Figure 2.15 shows the result of the value of  $z_w/h$  fitted for the wind profile. The values of  $z_w/h$  distributes between 1.6 and 2.5, and the value is larger for low wind speeds and smaller for high wind speeds. The trend of  $z_w/h$  changing with  $\lambda$  and wind speed is similar to that of  $u^*/u_h$ . Both

of them decreased as the wind speed increased. For a higher wind speed, 10 to 20 ms<sup>-1</sup>, the  $z_w$  values are very close to each other and both had a single peak between  $\lambda = 0.1$  to 0.2. Shao and Yang (2005) used  $z_w/h = 1.5$  to fit the data from regular surfaces and  $z_w/h = 2$  for the data from staggered surfaces Hall et al. (1996). Note that the value of  $z_w/h$  is much larger when  $u = 1$  ms<sup>-1</sup> than at any other wind speed. Since the wind speed of 1 ms<sup>-1</sup> is closer to the magnitude of the vertical velocity caused by shear flow, the shear flow may influence air flow at high altitude and result in larger  $z_w/h$ .

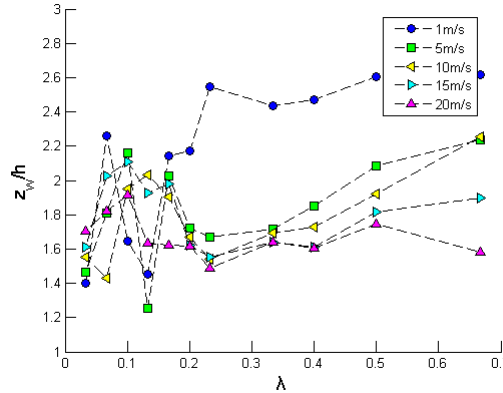


Figure 2.15 Values of  $z_w/h$  from the simulation data at wind speeds of 1, 5, 10, 15 and 20 ms<sup>-1</sup>.

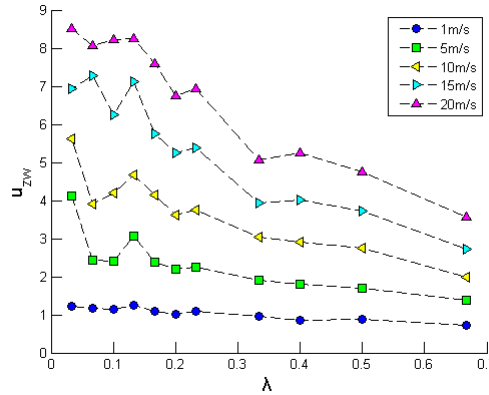


Figure 2.16 Parameter  $u_{zw}$  as determined from the simulation data for wind speeds of 1, 5, 10, 15 and 20 ms<sup>-1</sup>

The last parameter deduced in this section is  $u_{zw}$ . It is the magnitude of the wind speed at  $z_w$ . The parameter  $u_{zw}$  is important in determining the corrected wind profile for a rough surface, and it is defined in Equation (1.17). For fitting of a wind profile, it becomes:

$$u_{zw}^+ = -\frac{b_2 - z_w}{a_2} \quad (2.17)$$

where  $u_{zw}^+$  is non-dimensional number, defined as  $u_{zw}^+ = u_{zw}/u_*$ .  $u_{zw}$  is obtained and shown in Figure 2.16.

Figure 2.16 shows that  $u_{zw}$  increases as the wind speed increases and decreases as  $\lambda$  increases. The value of  $u_{zw}$  is dependent on the choice of  $z_w$ . However, it has been rarely discussed by other scientists, and it is listed here as a reference for reproducing this dataset. More detail of  $u_{zw}$  will be discussed for 3D data in the next chapter.

## 2.6 Conclusion

A correct estimation of the flow field and drag on rough surfaces requires a suitable parameter for the dimension of the wake behind roughness elements. The wake on rough surfaces are studied and the relationship between the geometry of the wake and the friction velocity is deduced through 2D simulations. Momentum flux represented as the friction coefficient  $u^*/u_h$  and other parameters of the corrected logarithmic wind profile of  $d/h$ ,  $z_0/h$ ,  $z_w/h$ , and  $u_{zw}$  are analyzed and calculated from the simulation data, and plotted in diagrams versus  $\lambda$  for a wide range of wind speeds.

For 2D cases, the wakes behind rough elements can be distinguished as half wakes or full wakes. At lower wind speeds or over dense surfaces, the wakes are half wake; at a higher wind speeds or on sparse surfaces, the wakes are full wake. The size and type of the wake is subject to  $\lambda$ ,  $\lambda_w$  and  $u_r$ . Although the details of the flow conditions may differ between 2D and 3D simulations. The drag simulated in 2D cases are consistent with laboratory measurements. Thus most conclusions of 2D simulation are important for analysis of flow on 3D surfaces:

- (a) Under certain wind speed, each of the wakes behind isolated elements of identical  $b$  and distinctive  $h$  has the same  $\lambda_w$ . And  $\lambda_w$  is a constant when the wake is a full wake for all wind speeds. Thus,  $\lambda_w$  is independent from both  $h$  and  $u_r$ , when the wake is full wake.
- (b) The wake behind an isolated element and the wake on a denser rough surface can be distinguished by the height and length of the wake. When the wake size is not restrained,  $L_w < l$  and  $h_w = h$ . On a denser surface, the  $L_w = l$  and  $h_w < h$ .
- (c) A factor of  $\lambda_w/\lambda$  is found to be important for distinguishing the surface with strong shear flow from the surface with weak shear flow. This factor will be used to distinguish the strength of the shear flow for 3D and 2D elements in the next chapter.
- (d) When the distance between elements equals to  $L_w$ , the strength of shear flow on the element is equivalent to the strength of shear flow on the underlying surface. Thus, when  $\lambda = \lambda_a$ ,  $\lambda = \lambda_w$ .

In sum, the parameter of  $\lambda_a$  is suitable to associate the flow condition, the dimension of wake, and the roughness density. The discovery of  $\lambda_a$  is the key to build a physical model for drag and drag partition.



## 3.Drag on rough surfaces

*New model validated by 3D simulations of air flow over rough surfaces*

### 3.1 Introduction

Momentum transfer from atmosphere to rough surfaces can be quantified by drag (Schlichting & Gersten, 2000). Drag on flat surfaces is well understood (Garratt, 1994). Placing roughness elements on a smooth surface generally increases the total drag (Cheng et al., 2007; Raupach, 1992; Schlichting, 1936; Shao & Yang, 2008; Wooding et al., 1973). For certain types of surfaces, the drag may reaches a peak, before the total drag decreases as roughness density increases (Shao & Yang, 2008; Walter et al., 2012a). As the roughness density increases, the drag on the elements increases and the drag on the underlying surface decreases (Marshall, 1971; Schlichting, 1936). This trend of drag partition changing with roughness density were physically parameterized (Raupach, 1992). However, the parameterization of the total drag on rough surface is not as successful as drag partition. Raupach (1992) proposed a theory for the estimation of friction coefficient ( $u^*/u_h$ ). An empirical parameter,  $c$ , is used in the expression of friction coefficient. And this empirical expression of friction coefficient may not have solution in some cases, due to its exponential form. Therefore it is necessary to develop a physical model of drag on rough surfaces with more reasonable expressions.

Raupach's model (1992) is the most widely used drag and drag partition model, but it is focused on sparse surfaces. Scientists have developed several variations of Raupach's model to estimate drag on dense surfaces, but the fundamental expressions remained unchanged (Cheng et al., 2007; Shao & Yang, 2005; Shao & Yang, 2008; Walter et al., 2012a). Moreover, to estimate drag on surfaces with different shapes of elements, a parameter of  $\beta$  was used as a tuning factor in the expression of drag partition

(Raupach, 1992). However, the dependency of  $\beta$  on the dimension or the shape of elements was not parameterized. Therefore, it is necessary and challenging to consider the dimension or shape of roughness element in the new model of drag and drag partition on rough surfaces.

This chapter proposes a physical model of drag and drag partition, based on a resistance method. The momentum flux to the rough surface is analyzed for the element and the exposed underlying surface, respectively. Resistances, strengths of shear flows and the drag partitions are deduced. Drag partition is calculated to reproduce a classical experimental dataset of Marshall (1971). The comparison among the estimation of drag of this new model, the simulation result, and the experimental data show strong agreement. The drag and drag partitions are expressed as functions of  $\lambda$  and  $\lambda_a$ .  $\lambda_a$  is a critical parameter: It determines the surface which has equivalent strength of shear flow on the element and on the underlying surface; and, it is also a function of length-to-height ratio ( $b/h$ ) of roughness elements.  $\lambda_a$  allows the new model to distinguish surfaces with elements of different  $b/h$ . Other physical meanings are introduced in Chapter 2.

The 3D Large Eddy Simulation for air flow over rough surfaces are conducted, for 11 distinctive surfaces ( $1/30 < \lambda < 1/2$ ) with identical elements of 10 mm height, at 6 different wind speeds ( $1\text{-}25 \text{ ms}^{-1}$ ). The friction velocities and friction coefficients are derived from the simulated drag on rough surface. The result of the simulation, together with classical laboratory measurements are used to validate the new drag partition model. The wind profiles as well as the parameters of the wind profiles for each run are also deduced and analyzed.

In this chapter, Section 3.2 introduces the details of advantages and disadvantages of the existing theory and Section 3.3 proposes the new theory of drag and drag partition. The setup of 3D simulation is presented in Section 3.4. The result of 3D simulation and experimental data are shown and compared to the new model in Section 3.5. The other parameters of the wind profile from simulation data are deduced in Section 3.6. Section 3.7 is the conclusion.

## 3.2 Existing theory of drag on rough surfaces

The existing drag partition theory (Raupach, 1992) is based on two hypotheses, the first one specifies the external scales controlling a shelter area  $A$  and volume  $V$  for an isolated roughness element, and the second one describes interactions between the roughness elements. The two hypotheses are:

- (a) For an isolated roughness element of width  $b$  and height  $h$  in a deep turbulent boundary layer with a friction velocity  $u_*$  and a mean velocity  $u_h$ , at height  $h$ , the effective shelter area  $A$  and volume  $V$  scale as follows:

$$A = c_1 b h \frac{u_h}{u_*}, \quad V = c_2 b h^2 \frac{u_h}{u_*} \quad (3.1)$$

- (b). When the roughness elements are distributed uniformly or randomly across a surface, the combined  $A$  or  $V$  can be calculated by randomly superimposing of individual shelter areas or volumes.

These two hypotheses allow for the deduction of an analytical form of shear stress as a function of the frontal area index.

Defining the shear stress on isolated elements as  $\tau_{r0}$  and on an unobstructed surface as  $\tau_{s0}$ , we have the following

$$\tau_{r0} = \lambda_f \rho C_r u_h^2, \quad \tau_{s0} = \rho C_s u_h^2 \quad (3.2)$$

where,  $u_h$  is the reference velocity at the average height of elements. The shear stress on the roughness element and on the surfaces are:

$$\tau_r(\lambda_f) = \lambda_f \rho C_r u_h^2 \left(1 - \frac{V}{nbh^2}\right)^n, \quad \tau_s(\lambda_f) = \rho C_s u_h^2 \left(1 - \frac{A}{nbh}\right)^n \quad (3.3)$$

The data for drag, which Raupach (1992) referred to in his study are mostly measured over a sparse surface with  $0.011 < \lambda_f < 0.18$  (Raupach 1980) and  $\lambda_f = 0.0039, 0.0078$ , and  $0.0156$  (O'Loughlin, 1965). Raupach (1992) argued that if surfaces are very densely crowded by elements and  $n \rightarrow \infty$ , then  $(1 - x/n)^n = e^{-x}$ , the shear stresses become,

$$\begin{aligned} \tau_r(\lambda_f) &= \lambda_f \rho C_r u_h^2 \exp\left(-c_2 \lambda_f \frac{u_h}{u_*}\right), \\ \tau_s(\lambda_f) &= \rho C_s u_h^2 \exp\left(-c_1 \lambda_f \frac{u_h}{u_*}\right) \end{aligned} \quad (3.4)$$

Then the total stress is

$$\tau = \rho C_s u_h^2 \exp\left(-c_1 \lambda_f \frac{u_h}{u_*}\right) + \lambda_f \rho C_r u_h^2 \exp\left(-c_2 \lambda_f \frac{u_h}{u_*}\right) \quad (3.5)$$

Raupach assumed that the  $c = c_1 = c_2$ , and the total stress is

$$\tau = (C_s + \lambda_f C_r) \rho u_h^2 \exp\left(-c \lambda_f \frac{u_h}{u_*}\right) \quad (3.6)$$

and the inverse of the friction coefficient is

$$\frac{u_h}{u_*} = (C_s + \lambda_f C_r)^{-0.5} \exp\left(\lambda_f \frac{c}{2} \frac{u_h}{u_*}\right) \quad (3.7)$$

There may be no real solution to Equation (3.7) when

$$\frac{(C_s + \lambda_f C_r)^{-0.5} c \lambda_f \frac{u_h}{u_*}}{2} > e^{-1} \quad (3.8)$$

Here, a reverse function  $W = W(y)$  of a function  $y = x \exp(-x)$  is introduced, and the friction coefficient in Equation (3.7) could be written as,

$$\frac{u_*}{u_h} = \frac{c \lambda_f}{-W(-c \lambda_f (C_s + \lambda_f C_r)^{-0.5})} \quad (3.9)$$

The friction coefficient deduced by Raupach (1992) are shown in Figure 3.1a. The empirical parameter of  $c$  is chosen as 0.37 to fit the experimental data of Raupach (Raupach et al., 1980) and O'Loughlin (O'Loughlin, 1965).

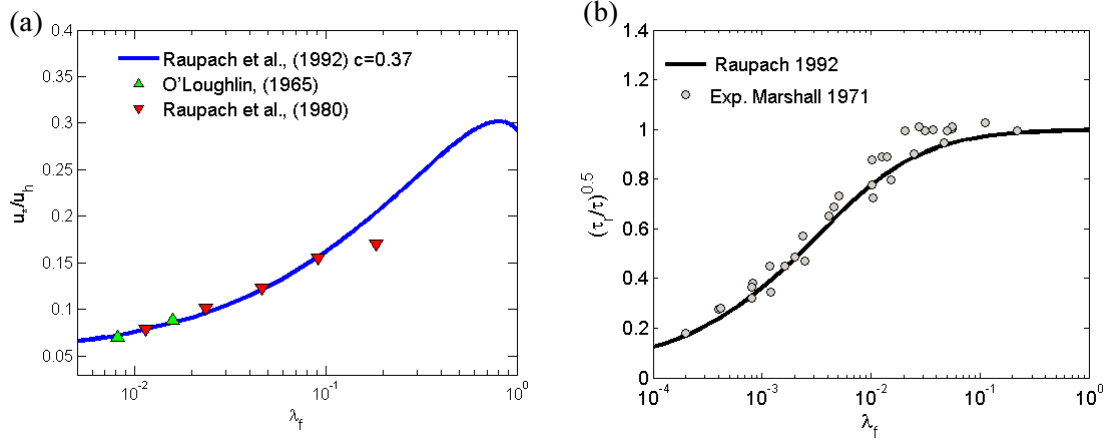


Figure 3.1 Solution of the friction coefficient and drag partition. (a) On the left is the friction coefficient from Raupach (1992), experimental data of Raupach (Raupach et al., 1980) and O'Loughlin (O'Loughlin, 1965); (b) On the right is the drag partition, the estimation is compared with experimental data from Marshall (Marshall, 1971), and the data include the drag partition on 5 rough surfaces with elements of different length-to-height ratios.

As the roughness elements, that considered by Raupach (1992), have  $b/h = 1$ , then we have  $\lambda_f = \lambda^2$ . And drag partitions can be expressed as functions of  $\lambda$ :

$$\frac{\tau_r}{\tau} = \frac{\beta \lambda^2}{1 + \beta \lambda^2}, \quad \frac{\tau_s}{\tau} = \frac{1}{1 + \beta \lambda^2} \quad (3.10)$$

where  $\beta = C_r / C_s$  is a constant, Raupach (1992) defines  $C_r = 0.3$  and  $C_s \approx 0.003$ . The ratio of the  $\tau_r$  to  $\tau_s$  are

$$\frac{\tau_r}{\tau_s} = \beta \lambda_f^2 \quad (3.11)$$

which indicates that the  $\tau_r$  and  $\tau_s$  are mutually proportional and the rate is a function of  $\lambda_f$ . This relationship is useful in the new model.

Figure 3.1(b) shows the estimation of the drag partition from Raupach (1992) compared to the well-known dataset from Marshall (1971). The wind tunnel experiment of Marshall (1971) measured the drag and drag partition on 5 types of rough surfaces with cylindrical elements of different length-to-height ratios. Note that the Raupach model cannot distinguish surfaces with these different elements, which may cause a 20% discrepancy among the measurements, as shown in Figure 3.1(b). As the quantities show in Figure 3.1(b) is the square root of  $\tau_r/\tau$ , the discrepancy can be 60% for  $\tau_r/\tau$ ; this is a discrepancy which should not be ignored.

The hypotheses of Raupach (1992) successfully associated the geometry of the sparse surface to the friction coefficient and were adopted by many meteorologists (Clifton & Lehning, 2008; Gillies et al., 2007; Shao & Yang, 2008; Walter et al., 2012a). However, the choice of the exponential function relies on the assumption of high  $\lambda$ , and it failed to produce real solutions for certain cases. These indicate that the exponential function in the expression of the friction coefficient may not be the best choice.

Shao and Yang (Shao & Yang, 2008) extended this model to dense surfaces by introducing an effective frontal area index. However, the hypotheses and the exponential functions are neither validated nor corrected. The lack of laboratory measurements of shear stress on a dense rough surface is the main reason for relying on the hypotheses, rather than facts (Raupach, 1992; Shao & Yang, 2008). According to the findings in Chapter 2, the full wakes have constant height-to-length ratio on surface with different  $\lambda$ , for each types of elements. By relating the surface drag to  $\lambda_a$ , it is possible to physically determine the drag and drag partition for each surface with different  $b/h$ .

This thesis proposes a resistance method to evaluate the surface drag as a fractional function of  $\lambda$  and  $\lambda_a$ . The details are described in the following section.

### 3.3 The new drag and drag partition theory

The estimation of previous models assumes that the size of the wake is a function of the friction coefficient and  $\lambda$ . Meanwhile, these models do not distinguish the surface elements of different length-to-height ratios. In this study, the momentum flux in the roughness layer is analyzed and the threshold roughness density  $\lambda_a$  is used. A physical model of drag and drag partition without empirical parameter is carried out. And  $\lambda_a$  distinguishes the surfaces with different of elements of different  $b/h$ .

#### 3.3.1 Total Resistance to the momentum flux

Traditionally, 1D model of momentum transfer uses a wind profile to quantify the momentum transfer (Cowan, 1968; Leuning & Attiwill, 1978; Thom, 1971). In a fully developed turbulent flow, the wind profile in the roughness layer and inertial layer are different due to the shear flows and the wakes. The velocity profile obeys Equation (1.15) (Raupach et al., 1980). Although some empirical values were used, parameters of the wind profile, i.e.,  $z_w$  and  $u_{zw}$ , were not parameterized (Raupach, 1992; Shao & Yang, 2005; Walter et al., 2012). And there is no simple expression of the wind profile in the canyon layer. As the wind speed is difficult to determine, the velocity difference is relatively easier to acquire. Therefore, to quantify the momentum difference between  $u(z)$  and  $u(h)$ , a square of velocity difference  $\Delta U^2(z)$  is defined, as:

$$\Delta U^2(z) = (u(z) - u(h))^2 \quad (3.12)$$

Here,  $u(h)$  is referred to the reference velocity, as it is in many studies (Raupach, 1992; Shao & Yang, 2005; Walter et al., 2012). The horizontal velocity increases as the height increases. The distance through which the momentum is transferred can be nondimensionalized and considered as a bulk resistance,  $R(z)$ . The momentum flux is defined as  $F(z)$ . When  $\Delta U^2(z)$  refers to voltage gradient, the momentum flux refers to electric current and  $R(z)$  refers to the resistance, these three parameters can be expressed in a same way as the Ohm's law, according to Equation (1.15). Then the resistance  $R(z)$  to the momentum transfer between  $z$  and  $h$  is:

$$R(z) = \frac{\Delta U^2(z)}{F(z)} \quad (3.13)$$

$R(z)$  is a dimensionless parameter. It is similar to an inversed drag coefficient. But note that,  $F$  is the strength of the shear flow, not the drag on surface. Ratios of the drag divide by components of  $F$  are introduced in the next section, as the absorption ratios of momentum fluxes. When the momentum transfer in the whole canyon layer is considered, the parameter of  $z$  in Equation (3.13) can be omitted.

The resistance in the canyon layer is influenced by horizontal inhomogeneity, differences exist for the element and the exposed underlying surface. Therefore, it is necessary to determine the resistances for different sections of the rough surface in the canyon layer.

### 3.3.2 Resistances of $R_r$ and $R_s$ to the momentum flux

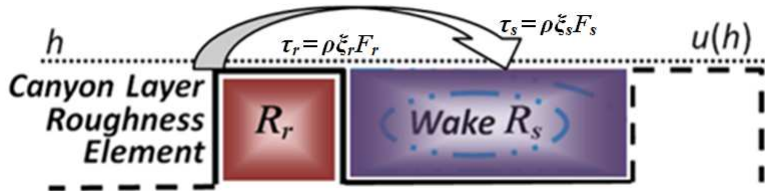


Figure 3.2 Schematic representation of resistances to momentum transfer in the canyon layer.

$u(h)$  is the velocity at height  $h$ . The  $R_r$  and  $R_s$  are resistances of the element and the underlying surface, respectively.  $\tau_r$  and  $\tau_s$  are the corresponding shear stresses;  $F_r$  and  $F_s$  are the strength of shear flow or momentum flux;  $\xi_r$  and  $\xi_s$  are the absorption ratios of momentum flux. The arrow indicates the path of the shear flow.

In the layer of horizontal heterogeneous flow, it is more accurate and reasonable to use different resistances for different locations than using a single bulk resistance for the whole surface (Incropera, 2011). Therefore, in the canyon layer, the surface must be categorized into different areas and deduce the resistance and drag for each area, in a sense similar to drag partition (Schlichting, 1936). The surface can be divided into the elements and the underlying surface, as shown in Figure 3.2.

The  $F$  and  $R_C$  can be categorized for the underlying surface, i.e.,  $F_s$  and  $R_s$ , and for the element, i.e.,  $F_r$  and  $R_r$ . These definitions imply that  $F_r$  and  $F_s$  are horizontally parallel to each other. Then, the total resistance in the canyon layer can be calculated together with Equation (3.13):

$$R_C = \frac{\Delta U_C^2}{F_r + F_s} = \frac{1}{\frac{F_r}{\Delta U_C^2} + \frac{F_s}{\Delta U_C^2}} = \frac{1}{R_r + R_s} \quad (3.14)$$

where  $\Delta U_C^2$  is the square of velocity difference between the top and bottom of canyon layer,  $F_r$  is the momentum flux to the element, and  $F_s$  is the flux to the underlying surface. As  $F_r$  and  $F_s$  determine the momentum flux on the surface, and momentum flux is eventually carried by the shear flow. Thus they also determine the strength and the distribution of the strength of shear flow over the surface.

On a rough surface, the inhomogeneity of the air flow is mainly the result of the shear flow induced by the elements. The strength of the shear flow on the element increases as  $\lambda$  increases, and the shear flow

on the underlying surface decreases as  $\lambda$  increases. As a result, there is always a surface which has equal strength of shear flow on the element and on the underlying surface. As it is introduced in Chapter 1,  $\lambda_a$  is the roughness density of this particular rough surface. According to conclusion in Chapter 2, it is used here as the roughness density of the surface with equal  $F_r$  and  $F_s$ :

$$F_r(\lambda_a) = F_s(\lambda_a) \quad (3.15)$$

Thus,  $\lambda_a$  is related to the flow condition over the rough surface, and it is an important parameter for determining  $F_r$  and  $F_s$ .

Note that, the  $F_r$  and  $F_s$  determine the strength of the flow but not the drag on surface. Only a portion of momentum transfer to the surface can be absorbed by the surface, the other portions are carried away by the shear flow. Here define  $\xi_r$  and  $\xi_s$  as the absorption ratios of momentum flux on the element and the underlying surface, respectively. They are dimensionless ratio of the drag divided by the strength of the shear flow and density of air. Then the fluxes can be associated with drag, as

$$\frac{\tau_r}{\rho} = \xi_r F_r, \quad \frac{\tau_s}{\rho} = \xi_s F_s, \quad \frac{\tau}{\rho} = \xi_r F_r + \xi_s F_s \quad (3.16)$$

Then, the momentum flux is related to the shear stress on the surface.

The resistances are non-dimensional parameters, which are associated to the geometry of the surface and the wake. To deduce the expression of drag and drag partitions, the next section first deduces the resistances as functions of  $\lambda$  and  $\lambda_a$ . And the drag and drag partitions are deduced in section 3.3.4.

### 3.3.3 Determine the resistances

According to previous experimental results and the analysis in this thesis, under certain wind speed, the momentum flux on surfaces can be determined. Here lists all useful definitions and mathematic relationships for the momentum flow in canyon layer:

- (a) The relation between  $\tau_r$  and  $\tau_s$  obeys Equation (3.11):  $\tau_r / \tau_s = \beta \lambda^2$ ;
- (b) Definition of the resistance method in Equation (3.13):  $\Delta U_C^2 = FR_C$ , for canyon layer;
- (c) Total resistance of parallel resistances in Equation (3.14):  $R_C = 1/(1/R_r + 1/R_s)$ ;
- (d) From one of the definition for  $\lambda_a$  in Equation (3.15):  $F_r(\lambda_a) = F_s(\lambda_a)$ ;
- (e) Definition of the ratio of momentum absorption:  $\tau_r/\rho = \xi_r F_r$ ,  $\tau_s/\rho = \xi_s F_s$ ,  $\tau/\rho = \xi_r F_r + \xi_s F_s$  (Equation (3.16)); and
- (f) The maximum  $\tau_r$  is the maximum total shear stress as  $\tau_{rr}$ , and the largest  $\tau_s$  is the total drag on smooth surface as  $\tau_{s0}$ .

Therefore, according to Equations (3.16) and (3.13)  $F_r$  and  $F_s$  can be expressed as

$$F_r = \frac{\tau_r}{\rho \xi_r} = \frac{\Delta U_C^2(\lambda, \lambda_a)}{R_r(\lambda, \lambda_a)}, \quad F_s = \frac{\tau_s}{\rho \xi_s} = \frac{\Delta U_C^2(\lambda, \lambda_a)}{R_s(\lambda, \lambda_a)} \quad (3.17)$$

where  $\Delta U_C^2(\lambda, \lambda_a)$  equals to the square of wind speed at  $h$ , it is a function of the geometry of the surface and the dimension of the wake, i.e.,  $\lambda$  and  $\lambda_a$ ; and  $R_r(\lambda, \lambda_a)$  and  $R_s(\lambda, \lambda_a)$  are the resistances which determine the distribution of the strength of shear flow on the element and the underlying surface, respectively.

From Equation (3.11) and (3.17), we have

$$\frac{F_r}{F_s} = \frac{R_s}{R_r} = \frac{\tau_r \xi_s}{\tau_s \xi_r} = \beta \lambda^2 \frac{\xi_s}{\xi_r} \quad (3.18)$$

Therefore, according to the definition of  $\lambda_a$  (Equation (3.15)), and Equation (3.18), we have

$$\beta = \frac{\xi_r}{\lambda_a^2 \xi_s} \quad (3.19)$$

Then, we can deduce the simplest forms of momentum flux from Equations (3.11), (3.17), (3.18), and (3.19) as

$$F_r = \Delta U_c^2 (\lambda, \lambda_a) \frac{\lambda}{\lambda_a}, \quad F_s = \Delta U_c^2 (\lambda, \lambda_a) \frac{\lambda_a}{\lambda} \quad (3.20)$$

Therefore, according to Equation (3.13) and Equation (3.20), the resistances of the element and the underlying surface are

$$R_r = \frac{\Delta U_c^2}{F_r} = \frac{\lambda_a}{\lambda}, \quad R_s = \frac{\Delta U_c^2}{F_s} = \frac{\lambda}{\lambda_a} \quad (3.21)$$

These equations imply that the resistances are independent from the strength of the shear flow, while relying on the density of roughness element and the distribution of the shear flow, i.e.,  $\lambda$  and  $\lambda_a$ . Then, the total resistance of the canyon layer can be calculated from Equation (3.21):

$$R_C = \frac{1}{\lambda_a/\lambda + \lambda/\lambda_a} \quad (3.22)$$

Then, the ratio of  $R_r$  to  $R_C$ , and the ratio of  $R_s$  to  $R_C$  are:

$$\frac{R_r}{R_C} = \frac{\lambda_a/\lambda + \lambda/\lambda_a}{\lambda_a/\lambda}, \quad \frac{R_s}{R_C} = \frac{\lambda_a/\lambda + \lambda/\lambda_a}{\lambda/\lambda_a} \quad (3.23)$$

These ratios are consistent with the analysis in this chapter and results of previous experiments, without undetermined parameters. Thus, the next section deduces the drag and drag partitions as function of  $\lambda$  and  $\lambda_a$ , based on this resistance method.

### 3.3.4 The new expression of drag and drag partitions

When the resistances and their relation with drag are determined, the drag can be determined separately. The total drag is defined in Equation (1.1) and Equation (3.14), which means that the momentum flux to the element and the underlying surface are parallel to each other, while sharing identical  $\Delta U_c^2$ . Thus,

$$FR_C = F_r R_r = F_s R_s \quad (3.24)$$

According to Equation (3.22) and the definition of the resistance method of Equation (3.13), the partition of drag can be deduced by the partition of resistances, as:

$$\tau_r = \rho \xi_r F_r = \frac{\rho \xi_r F R_C}{R_r}, \quad \tau_s = \rho \xi_s F_s = \frac{\rho \xi_s F R_C}{R_s} \quad (3.25)$$

Under particular conditions,  $\rho\xi_r F$  and  $\rho\xi_s F$  can be determined. Firstly, on smooth surface, the drag on the underlying surface equals to the total drag, as

$$\tau_{s0} = \rho\xi_s F \quad (3.26)$$

Secondly, for the surface with maximum drag, the drag on element approaches the total drag, as

$$\tau_{rr} \approx \rho\xi_r F \quad (3.27)$$

From the experiments and simulations,  $\tau_{rr}$  and  $\tau_{s0}$  can be determined, respectively. Then  $\tau_r$  and  $\tau_s$  can be determined as

$$\tau_r = \frac{\tau_{rr} R_c}{R_r}, \quad \tau_s = \frac{\tau_{s0} R_c}{R_s} \quad (3.28)$$

Then the partitions of drag can be written as

$$\begin{cases} \tau_r = \frac{\tau_{rr} \lambda_a / \lambda}{\lambda_a / \lambda + \lambda / \lambda_a} \\ \tau_s = \frac{\tau_{s0} \lambda / \lambda_a}{\lambda_a / \lambda + \lambda / \lambda_a} \end{cases} \quad (3.29)$$

Note that the skin drag on the element (Shao, 2008) is considered as a part of  $\tau_r$ , thus not separately determined. The total shear stress is the sum of Equation (3.29):

$$\tau = \frac{\tau_{rr} \lambda_a / \lambda + \tau_{s0} \lambda / \lambda_a}{\lambda_a / \lambda + \lambda / \lambda_a} \quad (3.30)$$

Then,

$$\tau_r / \tau = \frac{\tau_{rr} \lambda_a / \lambda}{\tau_{rr} \lambda_a / \lambda + \tau_{s0} \lambda / \lambda_a} \quad (3.31)$$

Equation (3.29), (3.30) and (3.31) are referred to drag partition on surface with 3D elements, based on the resistance method. The 2D ridge-like elements are different from the 3D cubical (or cylinder) roughness elements. The absence of transverse densities of the elements means that the ratio of  $R_r$  to  $R_c$  can be assumed as  $R_r/R_c = (\lambda_a/\lambda + \lambda/\lambda_a)^8$ . Then the expression of drag on 2D elements is assumed:

$$\tau_r / \tau = \frac{\tau_{rr}}{\tau_{rr} \lambda / \lambda_a + \tau_{s0} \lambda_a / \lambda} \quad (3.32)$$

Equations (3.31), and (3.32) are the new expressions of drag partition for surfaces with 3D and 2D elements, respectively. In the rest of this chapter, comparisons of drag among the simulation results, prediction of the new theory and classical experiment results are presented, to validate this new theory.

---

<sup>8</sup> As the spanwise mutual sheltering is not well understood, the difference between the drag on element for 2D and 3D element are assume as a factor of  $\lambda/\lambda_a$ , as  $R_r(2D) = \lambda/\lambda_a R_r(3D)$ . This is reasonable as resistance of 2D element is smaller than of 3D element. This is supported by the theory in Section 2.4.2, and by the simulation and experimental results in Sections 3.5.2.1 and 3.5.2.2.

### 3.4 Setup of 3D simulation of flows over ridges

3D simulation on rough surfaces (66 runs)							
$u_r [\text{ms}^{-1}]$	1	5	10	15	20	25	
$\lambda$	1/30	1/15	1/10	2/15	1/6	1/5	4/15
$h [\text{mm}]$	10					$b/h$	1
Domain [ $\text{mm}^3$ ]	300*100*150					Time step [s]	0.002
Grid size [ $\text{mm}$ ]	0.1-1					Time length [s]	4
Total grids	1,000,000-1,200,000					Viscous model	Large Eddy Simulation

Table 3.1 Parameters and options for reproducing the 3D simulation of air flow over rough surfaces in *Ansys Fluent*

3D large eddy simulations are conducted over rough surfaces. The simulation domain is  $300 \text{ mm} \times 150 \text{ mm} \times 100 \text{ mm}$ . The parameters applied in the simulation are listed in Table 3.1. Bar-like ridges with a height and length of 10 mm are used as roughness elements, and the mesh are shown in Figure 3.3. The flow in the roughness layer is more complex than in the inertial layer as shown by the 2D simulation. And the thickness of the rough layer rarely exceeds the height of the element by 3 folds. Therefore, the mesh below  $3h$  is drawn twice as dense as in the higher part of the mesh. The roughness ridges lay perpendicular to the streamwise direction. The boundary conditions are periodic for the inlet and outlet as well as for the left and right boundaries. The top of the domain is defined as a wall with zero shear stress and the bottom rough surface is a wall with non-slip conditions.

The flow is initialized as a constant velocity field. The simulation for each surface and wind speed lasts 4 seconds, and the fully developed conditions are achieved after 0.5 second. Different wind speeds and roughness densities are used in the simulations. The given wind speeds in the simulation are 1, 5, 10, 15, 20, and  $25 \text{ ms}^{-1}$ . Mesh with different roughness densities are used to analyze the relationship between air flow and roughness density. The chosen  $\lambda$  varies from 0.033 to 0.5, which covers the greatest range of the values of interested the values used in previous experiments. The exact value of  $\lambda$  is chosen based on the 2D simulation to address the largest gradient of the drag coefficient and the roughness length. They are listed in Table 3.1.

An example of a transient flow, including the iso-surface of a high vorticity (4500) and the contour of UV Reynolds stress, is shown in Figure 3.3. The high vorticity area are mainly on the surface or above the top of wakes. The Reynolds stress is positive over the elements, and negative over the rest of surfaces. Note that all the flow fields analyzed in this thesis are time-averaged streamwise vertical cross section of the simulation results, they are shown in the following sections. Details of the results are in the next section.

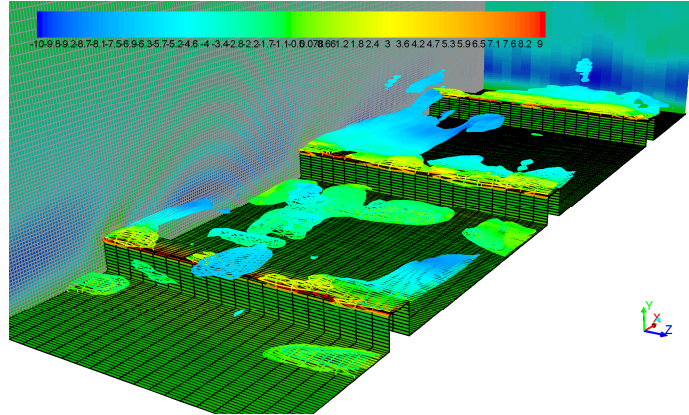


Figure 3.3 Details of the mesh and a transient flow of the 3D simulation for  $\lambda = 0.1$ . The colored area is the iso-surface of high vorticity with a value of 4500; the color represent the UV Reynolds stress. Note that all the flow fields analyzed in this thesis are time-averaged streamwise vertical cross section of the simulation results.

## 3.5 Results and discussion

### 3.5.1 3D simulation results of flow over rough surfaces

#### 3.5.1.1 3D Flow over isolated elements

This section presents the results of 3D simulations of flow over isolated elements. In Figure 3.4, the diagrams of the simulation runs at 5 wind speeds are shown in series. The wake is shown by the streamlines, and the Reynolds stress contour is shown in color.

In all cases, the streamlines separate from the frontal edge of the element, and the wake are all full wakes. This is different from the results of 2D simulation, even for the smallest wind speed. This also means that the height-to-length ratio of the wakes is independent from  $h$  and  $\lambda$ . And a uniform parameter can be assigned for the height-to-length ratio of the wakes.

The length of the wake can be determined from the scale below the diagrams. The maximum length of the wake is approximately 8 times per  $h$ . Considering the front vortices of a length of 1  $h$  that acts as an accessory to the full wake and may increase the total length of the wake, here chosen as  $L_w = 9h$ . The differences of  $L_w$  caused by changes in wind speed in 3D cases are much smaller than in 2D cases.

Figure 3.4 shows also the distribution of Reynolds stress. There is a region of positive Reynolds stress above the element, and a region of negative Reynolds stress above the underlying surface. Reynolds stress is a term of energy dissipation in the Reynolds averaged Navier-Stokes Equation (Schlichting & Gersten, 2000). With the direction of flow, a positive Reynolds stress indicates the acceleration of the flow and a negative value indicates a loss of momentum. These positive and negative Reynolds stress regions above the elements are also the regions where the velocity increases and decreases. These

regions also determine where the wake forms, develops and vanishes. As there is no restrain to the development of the wake, this pair of regions extends to the top of the domain and the whole domain is influenced by the shear flow induced by the element.

Because both the horizontal and vertical velocity are subject to Reynolds stress, it is safe to assume that the vertical velocity also increases and decreases in the two region of positive and negative Reynold stresses, respectively. This argument is useful in a later chapter on dry deposition, when the intensified vertical velocity around the element also influences the deposition velocity.

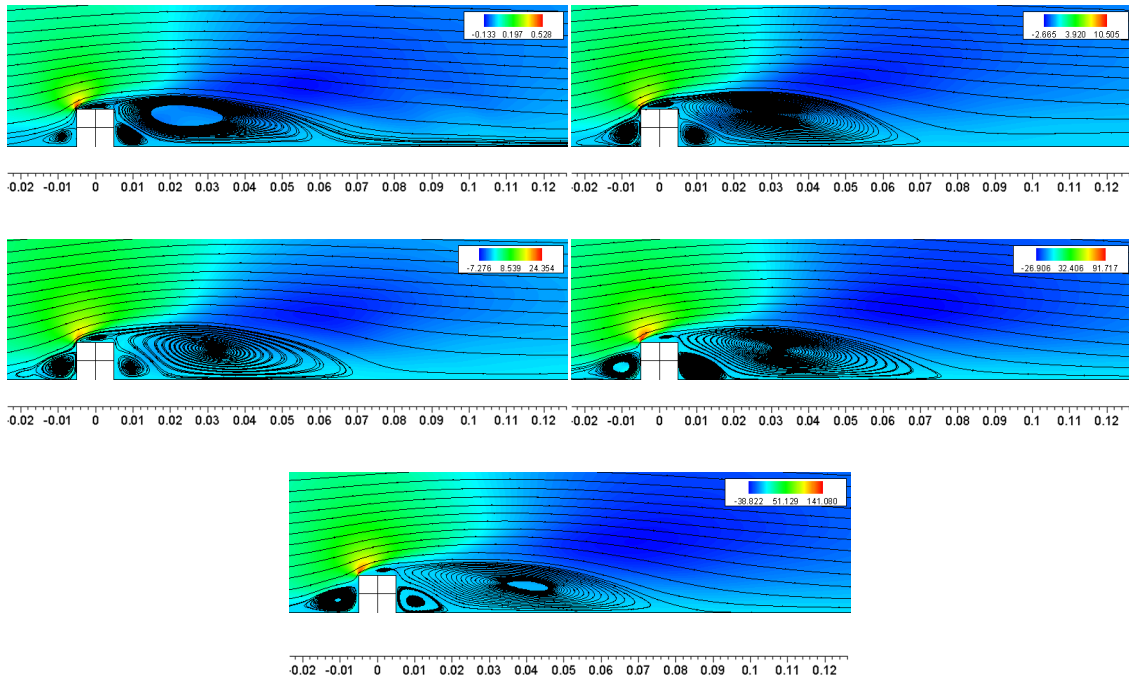


Figure 3.4 The flow over isolated element at wind speeds of 1, 5, 10, 15, and 20  $\text{ms}^{-1}$ . The lines are streamline, the background color represents the Reynolds stress, abscissa axis is the distance from the center of the element.

### 3.5.1.2 3D Flow over rough surfaces

This section presents the results of the 3D simulation of flow over rough surfaces, with different roughness densities. In Figure 3.5, the wake is shown by the streamlines, and the Reynolds stress contour is shown in color. The diagrams of flow over rough surfaces with 11 roughness densities under wind speed of 20  $\text{ms}^{-1}$  are shown in series.

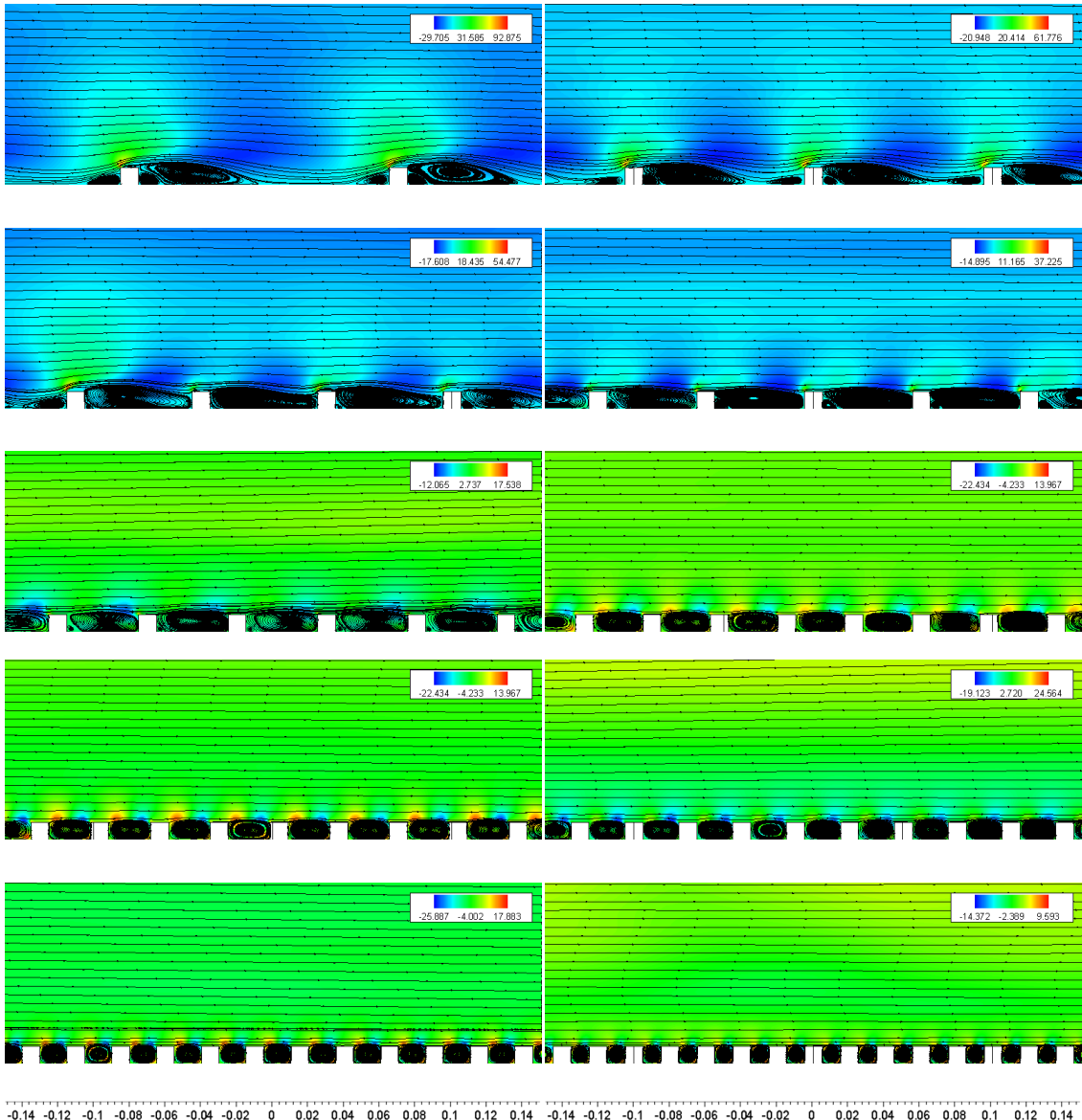


Figure 3.5 Flow over 11 distinctive surfaces. The lines are streamline, the background color represents the Reynolds stress, abscissa axis is the distance from the center of the domain. The wind speed is  $20 \text{ ms}^{-1}$ .

Both of positive and negative Reynolds stress regions exists across all of the diagrams in Figure 3.5. Three obvious facts can be concluded from the diagrams;

- A pair of a positive and a negative Reynolds stress region exist between each two roughness elements;
- The size of these regions decreases as the roughness density increases, in both vertical and horizontal directions; and
- Above the region of intensive Reynolds stress, the Reynolds stress is almost constant at each height.

These conditions of Reynolds stress distribution are consistent with the defined conditions of the roughness layer and the inertial layer. They are closely related to the strength of shear flow in the

roughness layer. When the Reynolds stress is less influential over the denser surface on a higher altitude, the roughness layer is also thinner. Furthermore, when the thickness of the roughness layer is smaller, according to Equation (1.11), the momentum flux is reduced. Consequently, the mass transfer can be also influenced.

In sum, the wake and its area of influence, as represented by the distribution of Reynolds stress are related to the roughness density. A quantitative study of the wake size can lead to a quantitative expression of a drag and drag coefficient as a function of roughness density.

### 3.5.1.3 Wind profiles on rough surface

This section presents the wind profiles of the 3D simulation of flow over rough surfaces. In Figure 3.7 each diagram the velocity profiles of one rough surface with 6 cases of different reference wind speeds are shown. A total of 11 diagrams represent the 11 roughness densities from 0.033 to 0.5. The diagrams are shown in series. Although the wind profile of a 3D simulation is very similar to the result of a 2D simulation, the existence of spanwise component of flow properties influenced the velocity profile in 3D results. The detailed differences of the wind profile between the 3D and 2D simulations will be discussed in Section 3.6 according to the fitted parameters of  $d/h$ ,  $z_0/h$ ,  $z_w/h$  and  $u_{zw}$ .

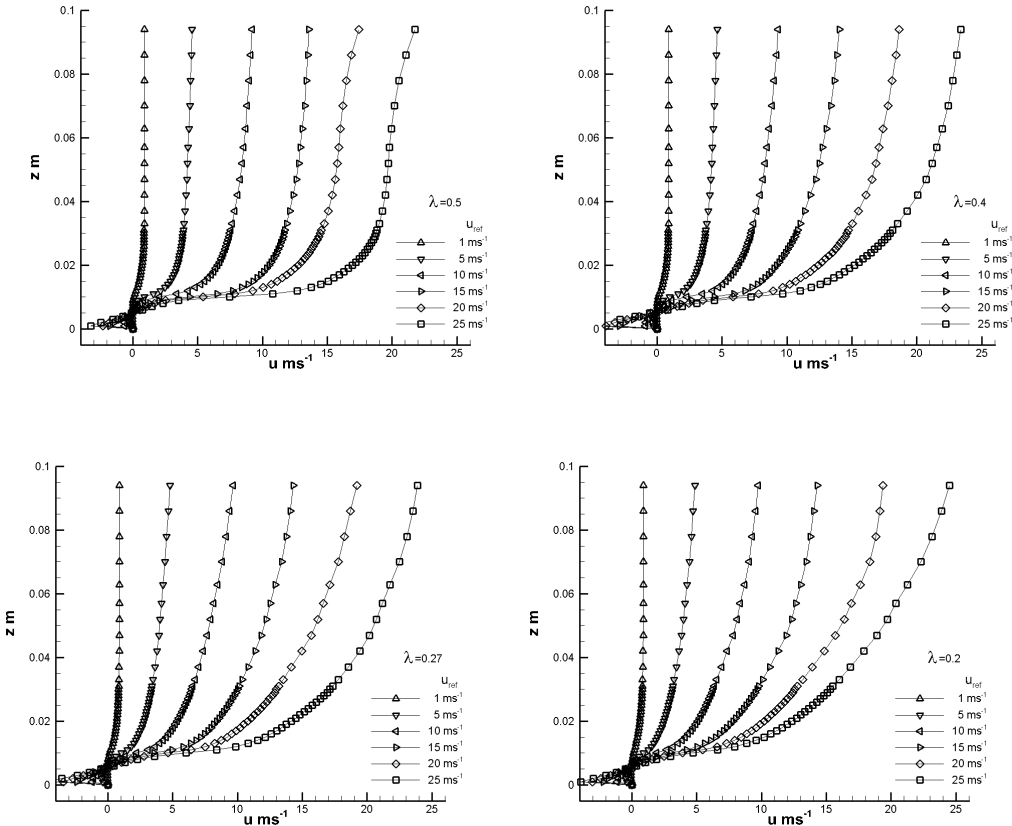


Figure 3.6 The wind flow profile over a rough surface in 3D simulation over 4 rough surfaces under 6 wind speeds.

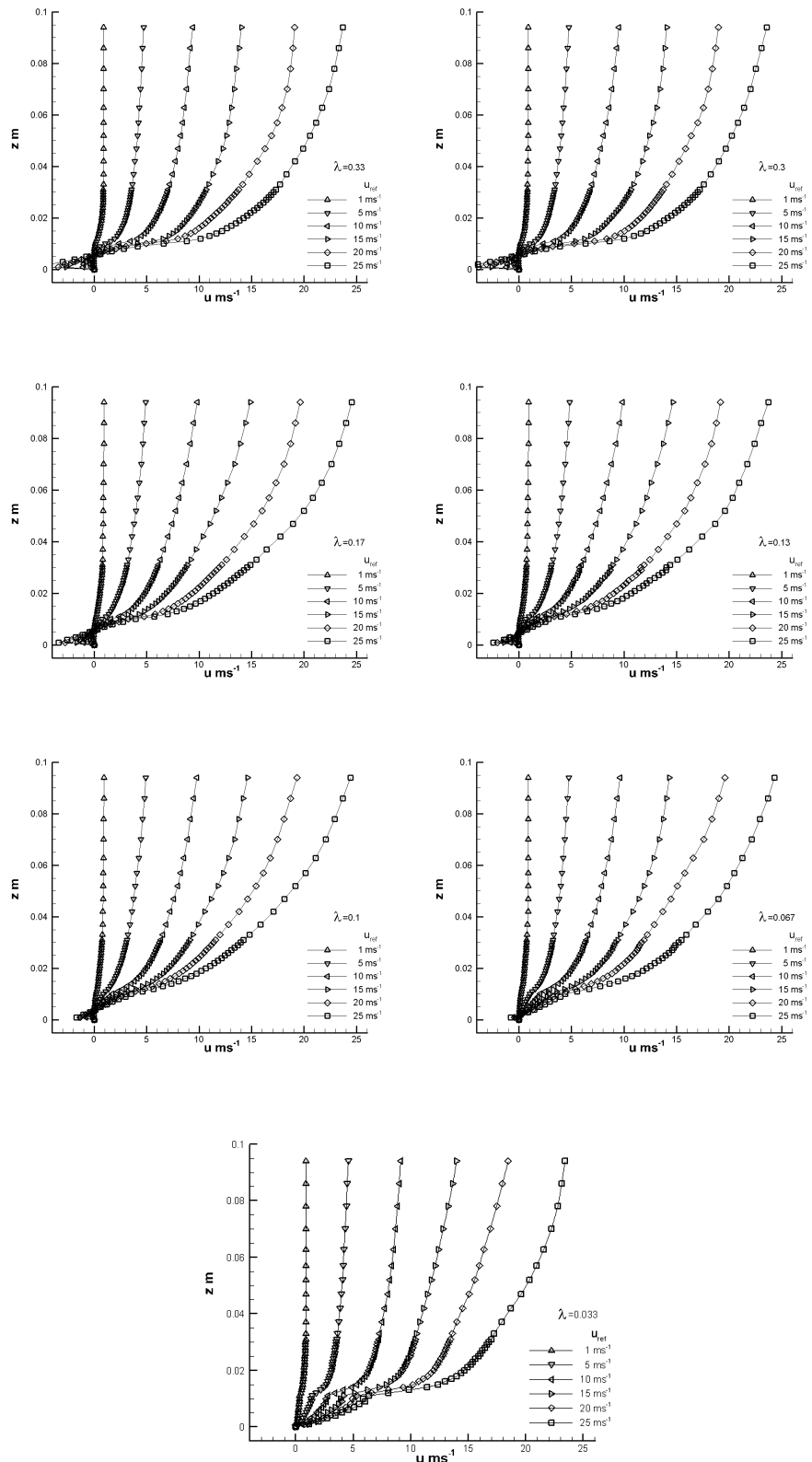


Figure 3.7 The wind flow profile over a rough surface in 3D simulation over 7 rough surfaces under 6 wind speeds.

### 3.5.2 Discussion on 3D simulation results

#### 3.5.2.1 The new expression of Friction velocity $u^*$

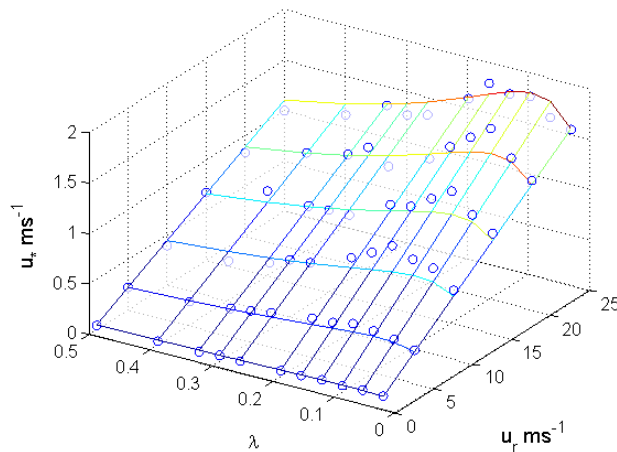


Figure 3.8 The simulated and estimated friction velocity for various wind speeds and roughness densities. The circles are simulation data, the mesh is the estimated data.

$u^*$	$\lambda = 1/30$	$1/15$	$1/10$	$2/15$	$1/10$	$1/6$	$1/5$	$1/4$	$2/5$	$1/2$	$2/3$
$u_r = 1 \text{ ms}^{-1}$	0.06	0.07	0.07	0.07	0.06	0.06	0.05	0.05	0.04	0.04	0.04
$5 \text{ ms}^{-1}$	0.32	0.38	0.41	0.43	0.39	0.38	0.33	0.3	0.27	0.23	0.22
$10 \text{ ms}^{-1}$	0.67	0.84	0.87	0.96	0.84	0.74	0.58	0.56	0.47	0.39	0.39
$15 \text{ ms}^{-1}$	0.99	1.12	1.31	1.18	1.05	1.01	0.81	0.81	0.79	0.84	0.66
$20 \text{ ms}^{-1}$	1.27	1.44	1.68	1.54	1.39	1.23	1.04	1.18	1.06	0.97	0.82
$25 \text{ ms}^{-1}$	1.53	1.6	1.75	1.72	1.78	1.57	1.31	1.26	1.3	1.1	0.99

Table 3.2 Friction velocity from 3D simulation for 11 different surfaces at 6 different wind speed.

The most important parameter for both the determination of momentum and mass transfer is the friction velocity, i.e.,  $u^*$ . In the simulation, the friction velocities are calculated from the total shear stress on the whole surface, and shown in Table 3.2 and Figure 3.8.

Data for the  $u^*$  from 11 surfaces under 6 wind speeds are acquired from the 3D simulation. These data are shown in Figure 3.8 as circles. In Figure 3.8,  $u^*$  generally increases as the wind speed increases and a peak is observed, which is consistent with the new drag and drag partition theory and the size of the wake behind a isolated element noted in Section 3.5.1.1.

Following the new drag and drag partition theory,  $u_*$  can be expressed as the reference velocity divided by the total resistance from Equation (3.30). No empirical parameters, but physical parameters need to be determined. As drag is proportional to the square of wind speed. The friction velocity is expressed as:

$$u_* = \frac{u_r}{20} \sqrt{\frac{\tau_{rr} + \tau_{s0} \lambda/\lambda_a}{\rho(\lambda_a/\lambda + \lambda/\lambda_a)}} \quad (3.33)$$

Here  $\lambda_a = 1/9$  for the result of 3D simulation, and the shear stresses are assumed proportional to the square of wind speed. The maximum drag on the element and the underlying surfaces, at  $20 \text{ ms}^{-1}$ , are  $\tau_{rr} = 3.5 \text{ m}^2\text{s}^{-2}$  and  $\tau_{s0} = 0.74 \text{ m}^2\text{s}^{-2}$ , respectively. The simulated data for the 11 rough surfaces and 6 wind speeds and estimation of Equation (3.33) are shown in Figure 3.8. The efficiency of the fitting is  $R^2 = 0.94$ .

According to Equation (3.33), the roughness density of the surface with the maximum value of drag and friction velocity can be calculated. This value of roughness density is defined as  $\lambda_m$ , and expressed as:

$$\lambda_m = (\lambda_a \sqrt{\tau_{rr}^2 + \tau_{s0}^2} - \tau_{s0} \lambda_a) / \tau_{rr} \quad (3.34)$$

For the simulation data,  $\lambda_m = 0.09$ . This value can be also observed from Figure 3.8.  $\lambda_m$  is useful to determine the surface with maximum drag, but the difference between  $\lambda_a$  and  $\lambda_m$  is needed to be noticed:  $\lambda_a$  is the threshold roughness density which distinguish sparse and dense surface<sup>9</sup>, as it is also the roughness density of rough surface with  $F_r = F_s$ ; while,  $\lambda_m$  is the roughness density of the rough surface, with 2D elements, which has the maximum drag, it is expressed as a function of  $\lambda_a$  (Equation (3.34)).

### 3.5.2.2 The new expression of the drag partition $\tau_r/\tau$

The drag partition ratio of  $r_r$  and  $r_s$  are assumed to be identical for different roughness density (Brown et al., 2008; Gillies et al., 2007; Musick & Gillette, 1990; Raupach, 1992; Shao & Yang, 2008; Walter et al., 2012a), though it is also different when the length-to-height ratio of the roughness elements changes (Marshall, 1971).

The experimental data of Marshall (1971) is well known and was used to develop models of drag and drag partition by many authors (Finnigan, 2000; Raupach et al., 1980; Shao & Yang, 2008; Wooding et al., 1973). This experiment used 5 different shapes of cylinders with length-to-height ratio of  $b/h=5, 3, 2, 1$  and  $0.5$ . The roughness densities range from 0.01 to 1. Because the drag partitions are objected to the  $b/h$  ratio, the roughness density of the maximum shear stress changes with  $b/h$ , and  $\lambda_a$  is a function of  $b/h$ . In Figure 3.9, the relationship between  $\lambda_a$  and  $b/h$  is shown.

---

<sup>9</sup>  $\lambda_a$  is the threshold roughness density when  $b = h$ . Otherwise the threshold roughness density is  $\lambda_a h/b$ . Different values of  $b/h$  are discussed only in Section 3.5.2.2.

The elements used in the experiment of Marshall (1971) are 3D elements. The expressions of  $\tau_r$  and  $\tau_s$  in the new theory are Equation (3.29), with  $\tau_{rr} = 5 \text{ m}^{-2}\text{s}^{-2}$  and  $\tau_{s0} = 0.74 \text{ m}^{-2}\text{s}^{-2}$  (Marshall, 1971), at  $u = 20.3 \text{ ms}^{-1}$ . And the partition of drag on the roughness elements is Equation (3.31). The well-known drag partition data from Marshall (1971) and the estimation of Equation (3.31) are shown in Figure 3.9.

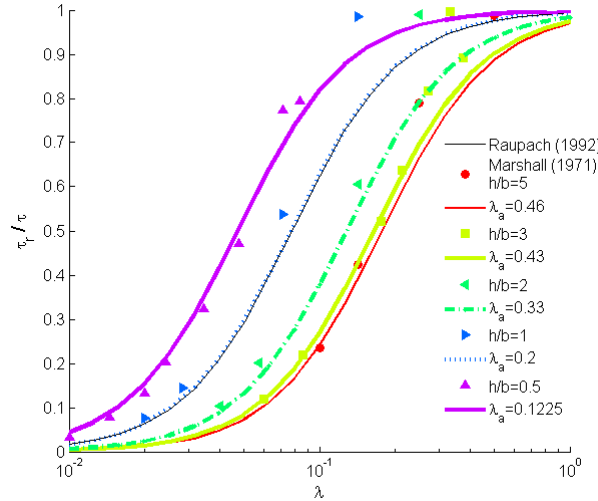


Figure 3.9  $\tau_r/\tau$  from the wind tunnel experiment of elements with 5 length-to-height ratios of  $b/h = 0.5, 1, 2, 3$ , and 5; and the estimation of new model (Equation (3.31)) and Equation (3.35) for a parameter of  $\lambda_a$  from 0.1225 to 0.46

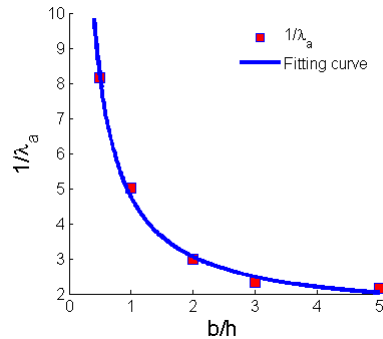


Figure 3.10  $\lambda_a$  versus  $b/h$  of roughness element, the squares are  $\lambda_a$  from the experimental data, the curve is  $\lambda_a$  from Equation 3.35.

The  $\lambda_a$  changes with  $b/h$ . The curve of  $\lambda_a$  can be perfectly fitted with a curve, as

$$\lambda_a = \left( 3.4 \frac{b}{h} + 1.35 \right)^{-1} \quad (3.35)$$

The fitted line and the derived  $\lambda_a$  from the experiment data of Marshall (1971) is shown in Figure 3.10. It shows clear trend of  $\lambda_a$  changing with  $b/h$ . Equation (3.31) together with Equation (3.35) provides a solution for the friction coefficient of different length-to-height ratios of a roughness element. This is a novel finding in this thesis. Figure 3.10 shows that the curve of drag partition of Raupach (1992) and

the curve of new theory are the same when  $b/h = 1$ , which means that the new theory is supported by the theory of Raupach (1992).

The scheme of Shao (2005) and Shao & Yang (2008) is based on the exact expression of drag partition of Raupach (1992). Which means the application of Shao (2005) and Shao & Yang (2008) can be extended to different surfaces with different dimension of elements using the new drag partition theory. Thus the expression of this drag and drag partition can be also used to improve the schemes of Shao (2005) and Shao & Yang (2008).

### 3.5.2.3 The new expression of the friction coefficient $u^*/u_h$

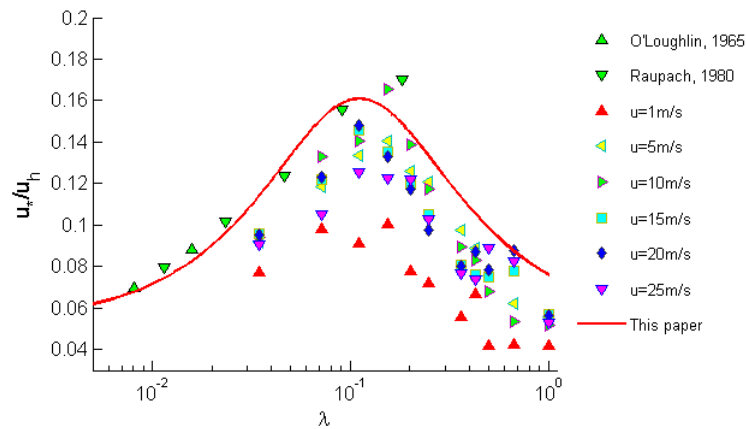


Figure 3.11 Friction coefficients on rough surfaces, including results of wind tunnel experiments of O'Loughlin (1965) and Raupach et al. (1980), the simulation results of 6 wind speeds, and the estimation according to Equation (3.36)

Because the momentum transfer over a rough surface is not a linear process, the friction coefficient is not a linear function of  $u^*$  or  $u_h$ . Complex mechanism of turbulence diffusion and wake transfer dominate this process, the expression of the friction coefficient can be very complex. Therefore, it is safe to assume that the function of the friction coefficient is similar to the friction velocity, and deduces it empirically from simulation data.

Equation (3.33) provides a suitable choice for the friction coefficient,

$$\frac{u_*}{u_h} = \frac{0.22}{\lambda_a/\lambda + \lambda/\lambda_a} + 0.052 \quad (3.36)$$

Here  $\lambda_a = 1/9$ . The estimated friction coefficients on a rough surface from Equation (3.36), including the results of a wind tunnel experiment by O'Loughlin (1965) and Raupach et al. (1980), and the simulation result from 6 wind speeds are shown in Figure 3.11.

The transfer of momentum is enhanced as  $\lambda$  increases, and it decreases as  $\lambda$  exceeds the threshold of  $\lambda_a$ . All of the data in Figure 3.11 are consistent with this trend, and the estimation of Equation (3.36) fits well with the data from wind tunnel experiments by O'Loughlin (1965) and Raupach et al. (1980), and with the simulation data for  $10 \text{ ms}^{-1}$  and  $20 \text{ ms}^{-1}$ . However, when the wind speed changes, many of the

friction coefficient simulation data are smaller than the estimation. This may be the result of the choice of reference height. Because there are limited experimental results of friction coefficients changing with wind speeds under similar condition, it is not possible to test the estimations under various wind speeds.

### 3.6 Parameters of wind profile in 3D simulation

Using the technique introduced in Chapter 2, the parameters of wind profile from 3D simulations are deduced. The values of  $d/h$ ,  $z_0/h$ ,  $z_w/h$  and  $u_{zw}$  for different surfaces and under different wind speeds are drawn in Figure 3.12 - 3.15.

Figure 3.12 shows the results of the  $d/h$ . The measured  $d/h$  in a 3D simulation is similar to the result of the 2D simulation in Figure 3.12. The  $d/h$  increases as the roughness density increases, which is related to a more restrained wake as the distance between the elements decreases. The  $d/h$  does not change much when wind speed changes.

The law of the  $z_0/h$  changing with the wind speed is similar for all wind speeds. There are peaks for these values over different roughness densities. The peak exists between  $\lambda = 0.1$  and  $\lambda = 0.133$ . The magnitude of  $z_0/h$  in Figure 3.13 is similar to the 2D simulation result in Figure 2.14.

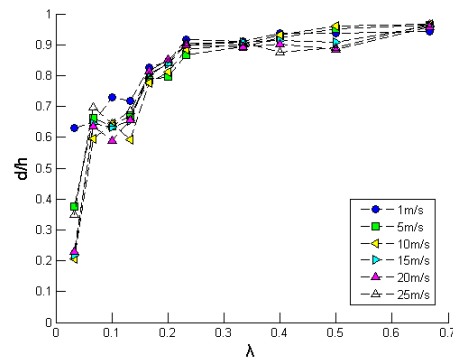


Figure 3.12  $d/h$  on 11 surfaces under 6 wind speeds

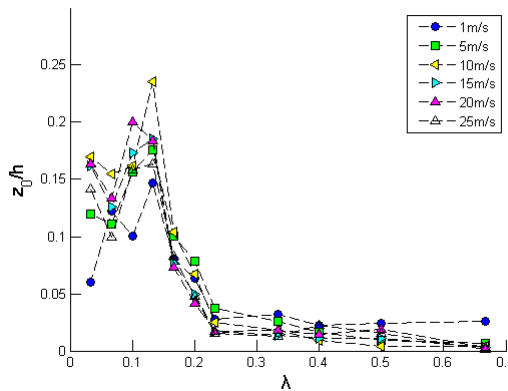


Figure 3.13  $z_0/h$  on 11 surfaces under 6 wind speeds

The results of the  $z_w/h$  in Figure 3.14 is smaller than those for the 2D simulation in Figure 2.15, whereas the  $z_w/h$  in the 2D and laboratory experiment are typical between 1.4 and 2.6; the results of the 3D simulation is 1 to 1.6. This may be the result of the use of a spanwise symmetrical roughness element. Without transverse heterogeneity, the thickness of the roughness layer must be smaller; and the existence of the spanwise shear stress will further reduce the vertical shear flow. The peak exists between  $\lambda = 0.667$  and  $\lambda = 0.133$ , which is similar to the 2D simulation.

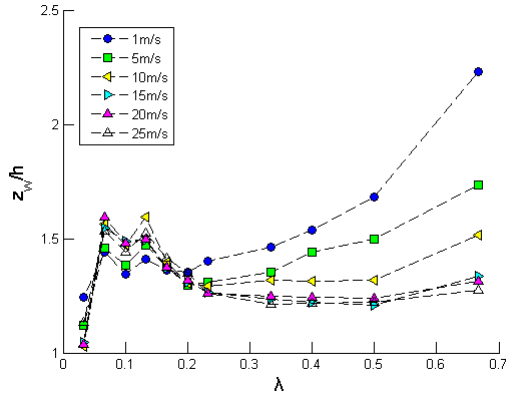


Figure 3.14  $z_w/h$  on 11 surfaces under 6 wind speeds

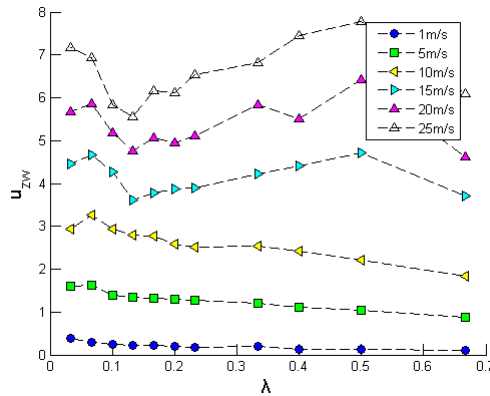


Figure 3.15  $u_{zw}$  on 11 surface under 6 wind speeds

However, the result of the  $u_{zw}$  in Figure 3.15 is different from the 2D simulation in Figure 2.16. In 3D simulation it is smaller and decreases slower as  $\lambda$  increases. Two reasons might have caused these difference. Firstly, because the thickness of the roughness layer in the 3D simulation is shallower than that in the 2D simulation, the shear flow is less influential to the main stream. Thus  $u_{zw}$  does not change as much as in 2D simulation. Secondly, the existence of spanwise components reduces the streamwise velocity, thus is  $u_{zw}$  smaller. These are reasonable difference from 2D and 3D simulation.

For some wind speeds, 15, 20, and 25  $\text{ms}^{-1}$ . The  $u_{zw}$  start increasing after it reaches a nadir around  $\lambda = 0.15$ . The reason is not clear, but the nadir is also at where then peak of  $z_w$  and  $z_0$ . This trend may be analyzed in the future.

The average velocity over all surfaces is roughly 1/4 of the reference velocity. As shown in Table 3.3. The average error for estimating  $\overline{u_{zw}}$  with  $u_r/4$  is only 7.9 %. This estimation is about 81% efficient for  $u_r = 1 \text{ ms}^{-1}$ , while 90% - 98% efficient for other wind speeds. Therefore, estimating  $\overline{u_{zw}}$  with  $u_r/4$  is an applicable method for wind speed larger than  $1 \text{ ms}^{-1}$ . It could be useful to estimate the  $z_w$  or other parameters of the wind profile.

$u_r$	$1 \text{ ms}^{-1}$	$5 \text{ ms}^{-1}$	$10 \text{ ms}^{-1}$	$15 \text{ ms}^{-1}$	$20 \text{ ms}^{-1}$	$25 \text{ ms}^{-1}$
$\overline{u_{zw}}$	0.2092	1.2797	2.6166	4.1473	5.3607	6.5834
$u_r$	0.8369	5.1188	10.4665	16.5892	21.4427	26.3336
$\frac{ \overline{u_{zw}} - 0.25u_r }{\overline{u_{zw}}}$	19%	2.3%	4.5%	9.6%	6.7%	5.1%

Table 3.3 The average  $u_{zw}$  under each wind speed and difference between  $\overline{u_{zw}}$  and  $0.25u_r$ .

Because the flow over a rough surface is a nonlinear process, the precise value of the parameters can only be obtained through a numerical simulation or a laboratory measurement. It is more difficult to find a simple approach for estimating these parameters using linear functions as functions of both the roughness density and wind speed rather than using wind speed or roughness density alone (Mahowald et al., 1999). Furthermore, without a thorough understanding or contribution of the spanwise properties of the flow, the divergence of the data in Figure 3.14 and Figure 3.15 are difficult to explain and those functions seem impossible to obtain. Therefore, future's work is needed to produce a dataset of flow properties over rough surfaces with a controlled spanwise distribution density of elements and an analysis of the spanwise components of these properties.

### 3.7 Conclusion

A resistance method is used to analyze the transfer of momentum and estimate the drag in canyon layer. A new drag and drag partition theory is proposed based on a resistance method and the study of the wake in Chapter 2. The geometry of surfaces is quantified as  $\lambda$ , and the condition of the shear flow is quantified by  $\lambda_a$ . A new expression of drag and drag partition are expressed as functions of roughness density, threshold roughness density and wind speed. The new theory is a physical theory, all parameters in the expression of drag and drag partitions are measurable physical quantities. A physical theory reveals the law of nature, it has wide applicability.

The use of  $\lambda_a$  in the new theory make it capable to estimate drag partition on surface with various  $\lambda$  and roughness elements with different  $b/h$ . The existing theory produces same result as the new theory, when  $b/h=1$ . The friction coefficient is also deduced.

The new equation of drag partitions uses fractional functions and overcomes the restraints of exponential functions chosen in previous theories. The estimation of this new model agrees well with classical experimental data on a surface with different  $b/h$ . The comparisons between the estimation and the experimental data of drag and drag partitions validates this theory for different surfaces. As

wind speed is also a parameter in the new theory, the drag under various wind speeds can be simultaneously estimated.

The trends of the resultant parameters of wind profiles changing with the roughness density are well represented in the 2D simulation results.  $z_0/h$  and  $z_w/h$  are smaller in the 3D simulation, and the  $u_{zw}$  is not only smaller but also decreasing slower in 3D than in 2D simulation. The existence of spanwise components of flow properties is mainly responsible for these differences. The value of the  $z_w/h$  is calculated from the 3D simulation results.  $z_w/h$  ranges from 1 to 1.6, with only several points of data larger than 1.6. The values of  $z_w/h$  are analogous to larger wind speeds. A peak of  $z_w/h$  exists for a  $\lambda$  between 0.0667 and 0.133. The results indicate that  $u_{zw}$  generally decreases as the roughness density decreases, the value of  $u_{zw}$  are different for different wind speeds. The average  $u_{zw}$  under certain wind speed larger than  $1 \text{ ms}^{-1}$ , and can be estimated by  $u_r/4$ .



# 4. Deposition on rough surfaces

*Based on 3D simulations of particle laden flow over rough surfaces*

## 4.1 Modeling particle deposition

Deposition velocity is the largest over high canopies. The largest discrepancies between the estimation of deposition velocity and the field measurements also occurs on these surfaces (Gallagher et al., 1997; Petroff et al., 2008; Ruijrok et al., 1995; Sehmel, 1980; Seinfeld & Pandis, 2012). For decades, these discrepancies had not been understood (Gallagher et al., 1997b; Kouznetsov & Sofiev, 2012). Previous studies used the model of the flow over a single cylinder to approach the flow over more complex surfaces and used a constant drag coefficient for all surfaces (Fuchs, 1964; Giorgi, 1986; Slinn, 1982). These models cannot distinguish the drag coefficients for different roughness densities and different wind speeds. As a result, the estimation of deposition on high canopies are far from accurate in reproducing the measurements (Gallagher et al., 1997; Kouznetsov & Sofiev, 2012; Petroff et al., 2008). Therefore, a detailed study is needed for both the airflow and the particle flux over rough surfaces.

The aim of this Chapter is to understand these discrepancies and to find the correct value of  $v_d$  on rough surfaces, based on numerical simulation data. This Chapter extends the simulations of airflow to 3D simulations of particle laden flow. Parameterization of the deposition on rough surfaces is based on the simulation.

Section 4.2 defines the deposition velocity; Section 4.3 conducts sensitivity tests to examine the error in existing models; Section 4.4 introduces the simulations with particle injection and their results are presented in Section 4.5. In Section 4.5, the results of momentum transfer are incorporated to the study of deposition. The deposition rate trends changing with  $u_r$ ,  $u^*$ ,  $\lambda$  and  $d_p$  are explained and parameterized. Section 4.6 concludes the findings of this Chapter.

## 4.2 Definition of deposition velocity in the simulation

For a certain size range of particles, deposition velocity is the average velocity of particles been transferred from a certain reference height to the surface. But, for most laboratory and field experiments, velocity of particle is not directly measurable, thus a classical definition is used (Chamberlain et al., 1966):

$$v_d(z) = \frac{F}{C(z) - C(0)} \quad (4.1)$$

where  $F(z)$  and  $C(z)$  are the flux and concentration of particles at height  $z$ , respectively.  $C(0)$  is usually assumed zero. When  $F(z)$  is not directly measured and an eddy correlation method can be used to calculate the deposition velocity when only the concentration and the vertical wind speed are measured:

$$v_d(z) = \frac{\overline{v'(z)C'(z)}}{C(z)} \quad (4.2)$$

where  $v'(z)$  is the fluctuation of vertical wind speed,  $C'(z)$  is the fluctuation of concentration. In this case, the  $v_d$  is a function of fluctuation of vertical wind speed and particle concentration. The mean vertical wind speed is assumed to be zero, and it is not considered in Equation (4.2). These definitions are used mainly in field measurements (Gallagher et al., 1997).

In the simulation, deposition velocity can be calculated from deposition rate as:

$$v_d = \frac{r_d h_D}{t} \quad (4.3)$$

where  $r_d$  is the deposition rate,  $h_D$  is the height of the domain and  $t$  is the time length of sampling. The  $r_d$  of dust onto surface can be obtained from simulations. It is the ratio of the number of dust particles trapped on the surface to the total number of dust particles that injected to the domain:

$$r_d = \frac{N_t}{N_D} \quad (4.4)$$

here  $N_t$  is the number of particles collected on the surface,  $N_D$  is the total number of particles. This definition is commonly used for numerical simulation of deposition (Luo et al., 2009; Wang & Squires, 1996; Zhang & Li, 2008).

## 4.3 Sensitivity tests of parameters in deposition models

### 4.3.1 Critical parameters for dry deposition

Sensitivity tests are conducted to understand the influence of surface roughness on the deposition process. The influence of various parameters on the deposition velocity is quantified.

An analytical form of the dry deposition velocity from Zhang's model (2001) is used as a sample, which is

$$v_d = \frac{\rho_p d_p^2 g C_c}{18\mu} + \frac{1}{\ln(z_r/z_0) - \Psi_H + \varepsilon_0 u_* \left( \left(\frac{v}{D}\right) + \left(\frac{d_p}{d_c}\right) + \left(\frac{S_t}{0.8 + S_t}\right)^2 \right) e^{-\sqrt{S_t}}} \quad (4.5)$$

The model of deposition velocity of Zhang et al. (2001) was developed from Slinn's model (1982) and shown in Figure 4.1. The definitions of the parameters in Equation (4.5) are provided in Section 1.3.4 of the two layer deposition model.

Among the critical parameters in Equation (4.5), e.g., molecular diffusivity, collector size, and the size of the particles, only the collector size  $d_c$  cannot be directly measured and needs to be determined empirically for distinctive surfaces. While the others can be empirically determined or measured. The parameter  $d_c$  is critical for the interception process, and it is responsible for the deposition of medium-sized particles, which have the largest discrepancy of  $v_d$  between the estimated and measured values. The direct influence of the fluctuation of  $d_c$  on deposition velocity can only be determined from tests. Since  $d_c$  appears as a part of the expression of the roughness resistance  $r_b$ , a sensitivity test on the resistance of roughness layer  $r_b$  is needed in the first place.

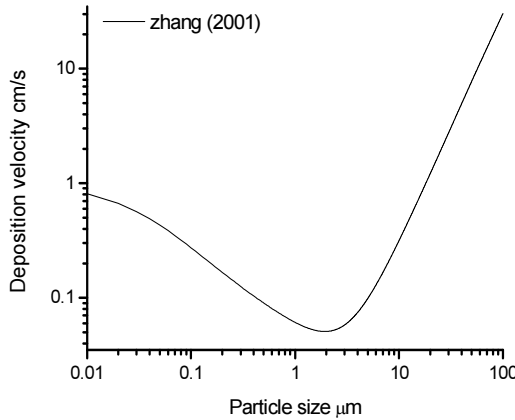


Figure 4.1 Deposition velocity of Zhang (2001) versus particle diameter with  $u^*=0.6\text{ms}^{-1}$ ,  $d_c=0.01\text{m}$ .

### 4.3.2 A sensitivity test of $r_b$

The surface resistance, i.e.  $r_b$ , is related to the surface roughness. As a rough surface is generally considered as a flat surface with randomly distributed roughness elements, then  $r_b$  of these surface is dependent on the distribution of these surfaces. However, in all dry deposition models,  $r_b$  were not calculated as a function of roughness density. A sensitivity test is conducted to measure the discrepancy between the response of  $v_d$  from a series of random  $r_b$  (normally distributed) or constant  $r_b$ . Here the discrepancy is defined as a relative error:

$$\text{relative error} = \frac{v_d(r_b = \text{Normal}) - v_d(r_b = \text{Constant})}{v_d(r_b = \text{Constant})} \quad (4.6)$$

The constant  $r_b$  is  $3000 \text{ sm}^{-1}$  and the normal distribution of  $r_b$  has a mean of  $3000 \text{ sm}^{-1}$  and a variation of 500.  $v_d$  is calculated in Equation (4.6). The result shows that the discrepancy could be as much as 337%.

### 4.3.3 A sensitivity test of $d_c$

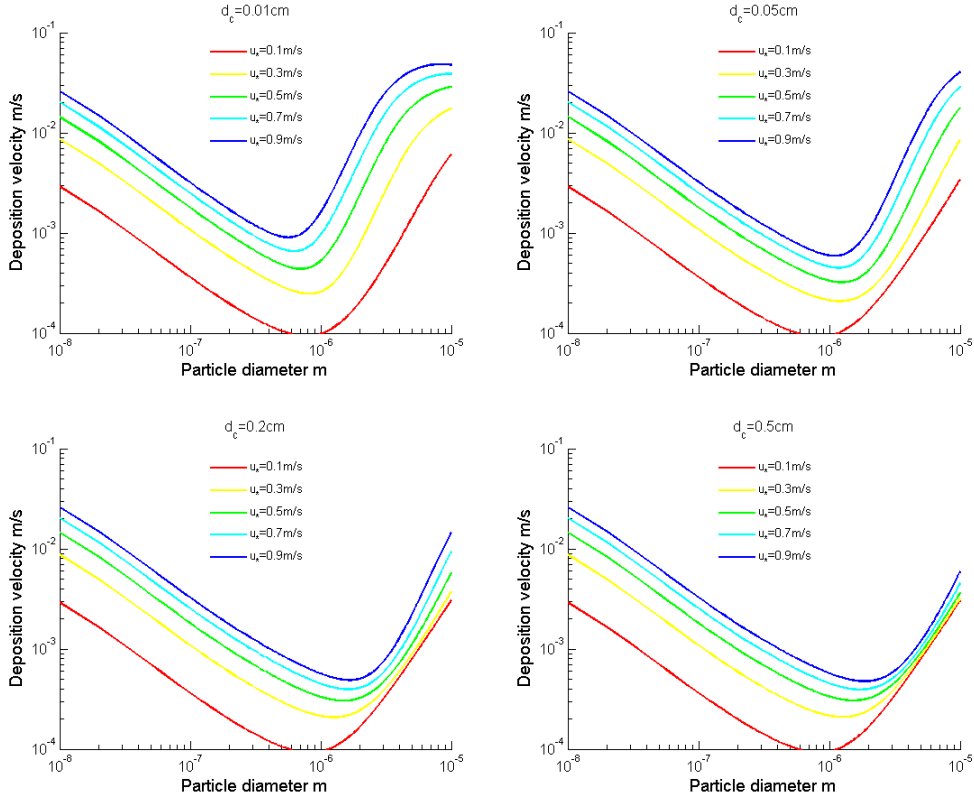


Figure 4.2 Deposition velocity versus particle diameter with different diameters of the collectors, under five wind speeds.

The diameter of collector  $d_c$  is critical in the expression of  $r_b$ . The dependency of  $v_d$  on  $d_c$ , together with  $u_r$  and  $d_p$ , is shown in Figure 4.2,  $v_d$  are calculated with Equation (4.6). The  $v_d$  is influenced by  $d_c$  for particles larger than  $0.5 \mu\text{m}$  and at higher wind speed. The variation of  $v_d$  is small for smaller particles and lower wind speeds. The discrepancy due to changes in  $d_c$  could be very large, as shown in Figure 4.2.

### 4.3.4 Sensitivity of the deposition velocity over high canopies

The discrepancies among the estimations and measurements of deposition in the natural condition can reach two to three orders of magnitude. Figure 4.3 shows some of the classical data from field measurements for high canopies compared to the estimation of Zhang (2001).

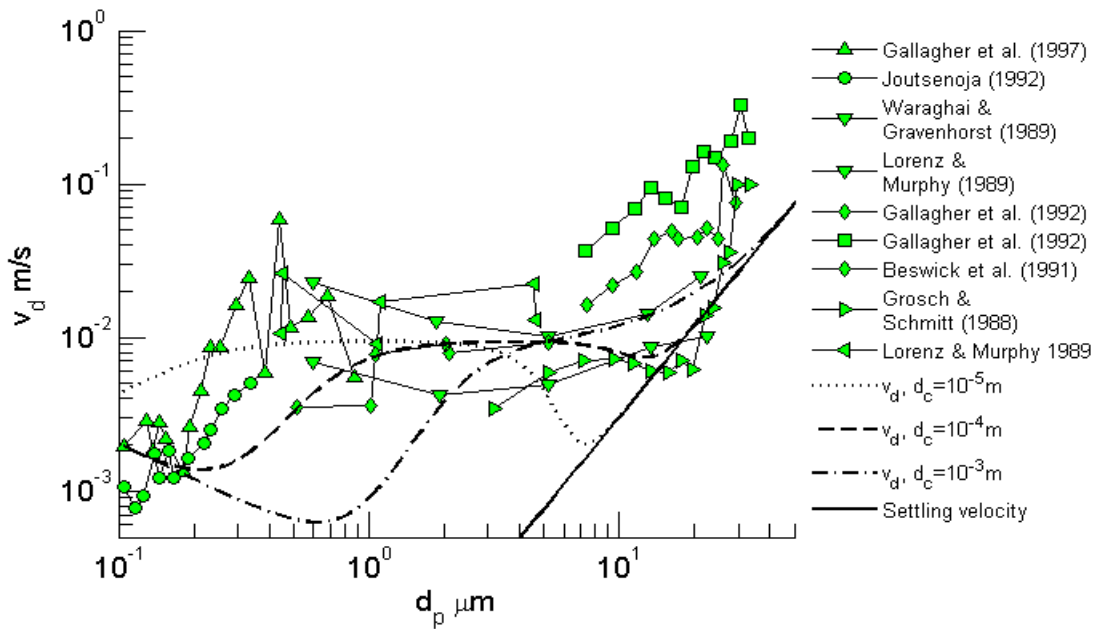


Figure 4.3 Data from the field experiment with high canopies and estimation by the model of Zhang (2001) with  $d_c=10^{-5}$ ,  $10^{-4}$  and  $=10^{-3}$  m.

Only some of the data could be fitted by the model, when  $d_c$  was modified in a large range of value. The  $v_d$  for all size ranges were underestimated, especially for medium-sized ( $0.5\mu\text{m}$  -  $1\mu\text{m}$ ) and very large particles ( $d_p > 10\mu\text{m}$ ), these are the two major discrepancies:

- (a) A peak deposition velocity exists for small particle around  $0.5\mu\text{m}$ , the deposition model did not show such a peak, and the differences between the values of  $v_d$  differ by a factor of 100.
- (b) The  $v_d$  for very large particles, i.e.,  $d_p > 10\mu\text{m}$ , was about 10 times larger than the estimation.

Such discrepancies are common in field measurements, but they had not been well understood for decades (Gallagher et al., 1997; Kouznetsov & Sofiev, 2012; Zhang & He, 2013). The mechanisms of the collection processes in existing deposition models served as resistances to the deposition process in the function of  $r_b$  (Equation (1.25)). Even if these collection efficiencies were set at 100%, the deposition velocities are smaller than the experimental data in Figure 4.3. The cause of these underestimation is the absence of mechanism of deposition by the shear flow induced by roughness elements. And only transport by diffusion are considered in previous models. The strength of the shear flow is dependent on  $u_r$  and  $\lambda$ , as it is determined in Chapter 3. Shear flow induced by the roughness element is effective to both the transfer of momentum and mass. Thus both the influence of  $u_r$  and  $\lambda$  should be addressed in the expression of  $v_d$ .

The sensitivity test have proven that  $r_b$  and  $d_c$  are important parameters in expression of  $v_d$ , with as much as 100 times of possible error resulting if these parameters are not properly considered. Therefore, better scaling parameters are needed for rough surfaces. In this chapter, the flow is assumed to be steady, and  $v_d$  is calculated in a numerical simulation as a function of  $u_r$ ,  $\lambda$ , and

$d_p$ . The results of the simulation will explain these discrepancies that found in the sensitivity tests. A complete dataset of  $v_d$  is presented in the following sections.

## 4.4 Setup of 3D Simulation of particle laden flow

3D simulation on rough surfaces with particle injection (66 runs)															
$u_r$ [ms <sup>-1</sup> ]	1		5		10		15		20		25				
$\lambda$	1/30	1/15	1/10	2/15	1/10	1/6	1/5	1/4	2/5	1/2	2/3				
Particle diameter [μm]	0.1	0.8	1.5	2.2	2.9	3.6	4.3	5	5.8	6.5	7.2	7.9			
Domain [mm <sup>3</sup> ]	300*100*150			$h$ [mm]	10			$b/h$	1						
Grid size [mm]	0.1 - 1		Total grids	740,000-900,000				Time step length [s]	0.002						
Time length [s]	4		Viscous model	Large Eddy Simulation			Stochastic tracking	Random walk							
Injection time [s]	0-0.2		Injection number	150,000											
Particle Material	Calcium Carbonate	Particle Density [kgm <sup>-3</sup> ]	2600			Particle Drag model	Stokes Cunningham								
Physical model for particle	Brownian motion			Shaffman lift force			Pressure gradient force								

Table 4.1 Parameters and options for reproducing the simulation in *Ansys Fluent* software in using a 3D simulation of particle laden flow over rough surfaces.

3D large eddy simulations are conducted over rough surfaces. The domain of simulations is 300 mm × 150 mm × 100 mm. The parameters applied in the simulations are listed in Table 4.1. Bar-like ridges that have heights and lengths of 10 mm are used as roughness elements. The mesh is shown in Figure 3.3. The meshes and the setup for the simulation of airflow are the same as in Section 3.4. To treat the particles, the bottom rough surface is defined as a trap for particles, which means that the particles are counted as trapped particles and removed from the domain, when the distance from the center of the particle to its surface is less than its radius.

The flow is initialized as a constant velocity field, and the dust particles are injected into the domain at the beginning of each simulation run. The injection continues for 0.2s. The dust particles are injected from the inlet, and the injection points are uniformly distributed on the surface of inlet with 5 columns and 20 rows. The particles are tracked in each time step of the flow calculation. The Random Walk model is applied to simulate the dispersion due to turbulence in each time step. The Shaffman force, Brownian diffusion, and pressure gradient force are included in the Equations of motion of the particles. The spatial distribution and the velocity of particles of the particle laden flow on the end of a simulation is shown in Figure 4.4.

The simulation for each rough surface and each wind speed lasts 4 s. The fully-developed condition is achieved after 0.5 s, with a steady deposition rate in each time step. The trapped particles are counted as deposited particles only after the flow is fully developed.

Different wind speeds and roughness densities are considered in the simulations. The given wind speeds in the simulation are 1, 5, 10, 15, 20 and 25 ms<sup>-1</sup>. Meshes with different roughness densities are used to analyze the relation between deposition velocity and roughness density. The chosen  $\lambda$  varies from 0.033 to 0.5, which covers the greatest range of the values that are used in previous experiments.

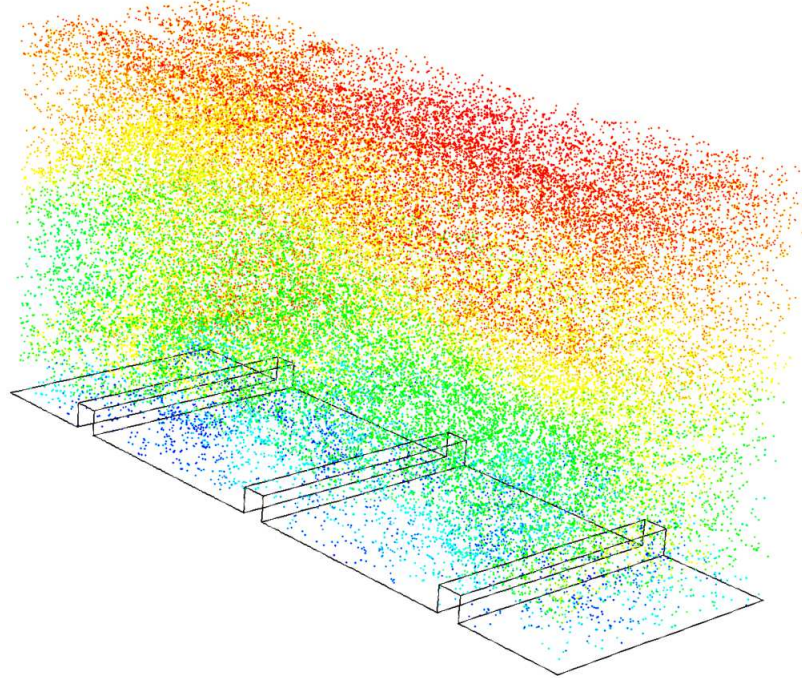


Figure 4.4 Simulation result of particle laden flow over a surface with  $\lambda = 0.1$ . The points are particles. The color of particles represents velocity magnitude, red for high speed and blue for low speed, maximum wind speed is 20 ms<sup>-1</sup>. The outline of bottom surface is also shown.

## 4.5 Results and discussion

### 4.5.1 Steady state particle flux

To make sure that in all simulations runs, particles are fully dispersed in the domain, the collection rate of particles changing with time steps are accounted. When the particles travel towards the rough surface, they take a period of time to finally reach the surface, and thus time is needed for the flux to reach steady state (Slinn 1980, 1982). In the simulation, the number of trapped particles are obtained. The fully dispersed condition is reached when the ratio of the deposited particles to total number of particles in the domain become constant.

The total deposition rate,  $r_d$ , is the ratio of deposited particle in each time step to total number of injected particles, and the transient deposition rate,  $r_{sd}$ , is the ratio of the number of deposited particles in each time step to the number of particles left in the domain:

$$r_{sd} = \frac{N_t}{N_D - N_t} \quad (4.7)$$

The deposition velocity is calculated from  $r_d$ , when  $r_{sd}$  is steady.

For all runs,  $r_d$  decreases rapidly and the reach a relative steady state in the first 0.5 s. After the first 0.5 s,  $r_{sd}$  becomes steady and the flux reaches steady state, too. Since the deposition velocity of particles larger than 5 microns is around  $0.35 \text{ ms}^{-1}$ , and  $h_D = 15 \text{ mm}$ , most of the largest particles are trapped before 3.5 s. Therefore, only the particles deposited between 0.5 s and 3.5 s are chosen as samples to deduce the deposition velocity with the method introduced in the previous sections.

## 4.5.2 Results of Deposition Velocity

### 4.5.2.1 Deposition velocity versus $\lambda$ and $d_p$

The simulations of 15 different sizes of dust depositing onto rough surfaces with 11 different rough densities at 6 different wind speeds are conducted. The results are shown in Figure 4.5 and Figure 4.6.

For a total of 66 runs, the time-averaged deposition velocities are calculated by counting the particles on the surface and with the definition of deposition velocity in Equation (4.3). Figure 4.5 shows simulated  $v_d$  in 6 diagrams, one for each wind speed. The corresponding curves of  $v_d$  are plotted for 6 rough surfaces, the abscissa is  $d_p$ . To show the trend of  $v_d$  changing with  $\lambda$ , Figure 4.6 shows the same dataset in 6 diagrams for 6 winds speeds, on the abscissa of  $\lambda$  for different  $d_p$ .

Figure 4.5 shows that, on sparse surfaces, particles with larger diameters generally deposit with higher velocities than smaller particles, this is consistent with previous experiments and theories of deposition on smooth and sparse surfaces (Petroff et al., 2008; Sehmel, 1980; Wesely & Hicks, 2000); while on denser surfaces, the difference between  $v_d$  of large and small particles are much smaller. Since the flow over dense surfaces is restrained by the smaller distance between the elements. The dimension of the wake and the magnitude of Reynolds stress are also restrained. Conversely, the wake induced by the elements can be fully developed on a sparse surface, and results in stronger shear flow. These can be observed from the diagram of the contours of Reynolds stress in Figure 3.4 and Figure 3.5. These results mean that, the size and strength of shear flow induced by elements have different effects on the  $v_d$  of particles with different sizes:

- (a) On sparse surfaces, with stronger shear flow,  $v_d$  of larger particles is larger than smaller particles.
- (b) On dense surfaces, with weaker shear flow,  $v_d$  of larger particles is similar to smaller particles.

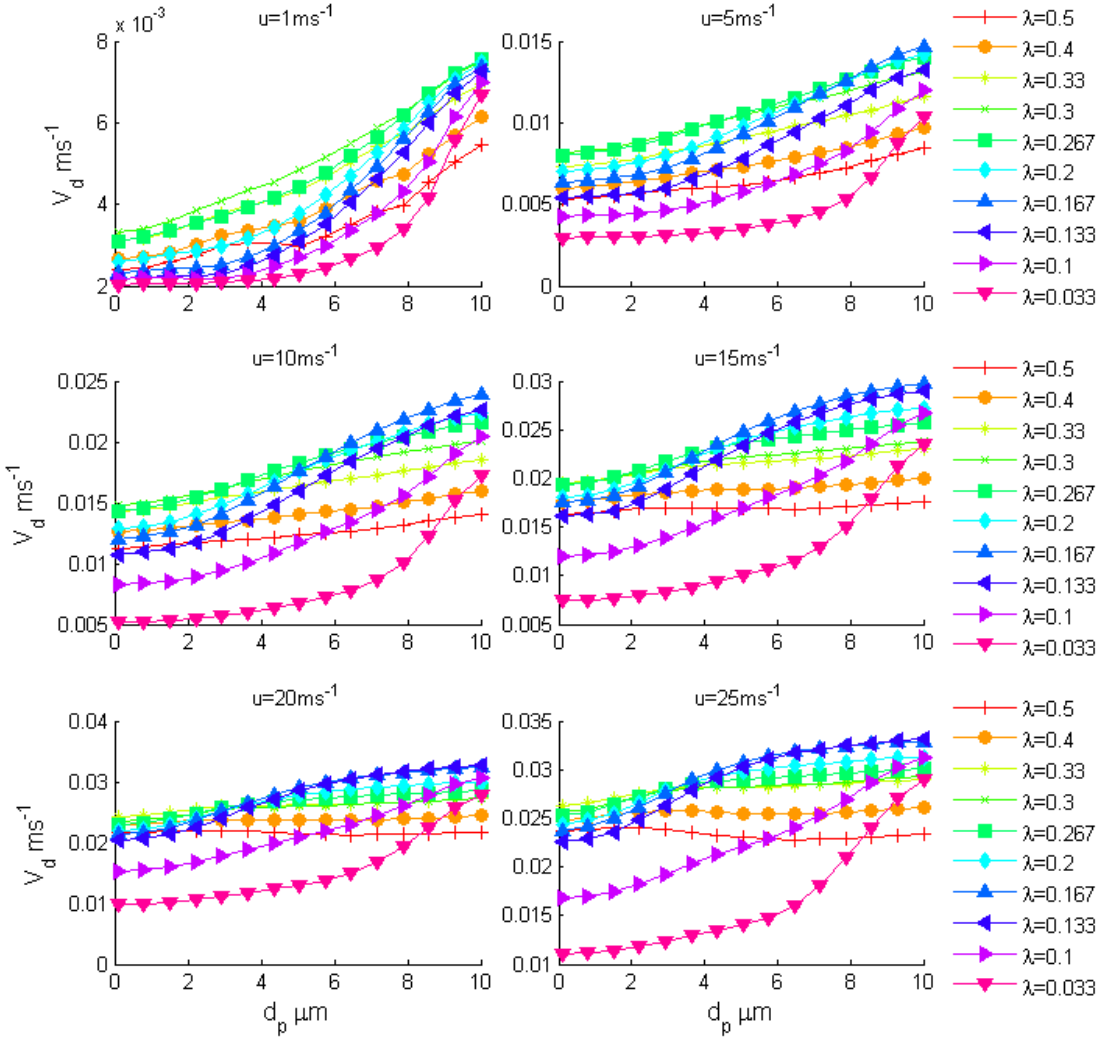


Figure 4.5 Deposition velocities versus particle diameters for surfaces with 10 roughness densities at six wind speeds, i.e.,  $u = 1, 5, 10, 15, 20$ , and  $25 \text{ ms}^{-1}$ .

These result is similar to the study of interception process of Giorgi (1986), who also argued that larger particle will not perfectly follows the flow and have larger  $v_d$ . The physical dependency of  $v_d$  on  $\lambda$  is parameterized in the following sections.

Figure 4.5 also shows that,  $v_d$  generally increases as wind speed increases. The difference among  $v_d$  for different particle sizes and surface roughness are also smaller for smaller wind speeds. This trend is also associated to the strength of shear flow. As wind speed increases, the strength of the shear flow increases, thus strengthening the vertical transport of particles. While the response of  $v_d$  of large and small particles to the change in Reynold stress differ due

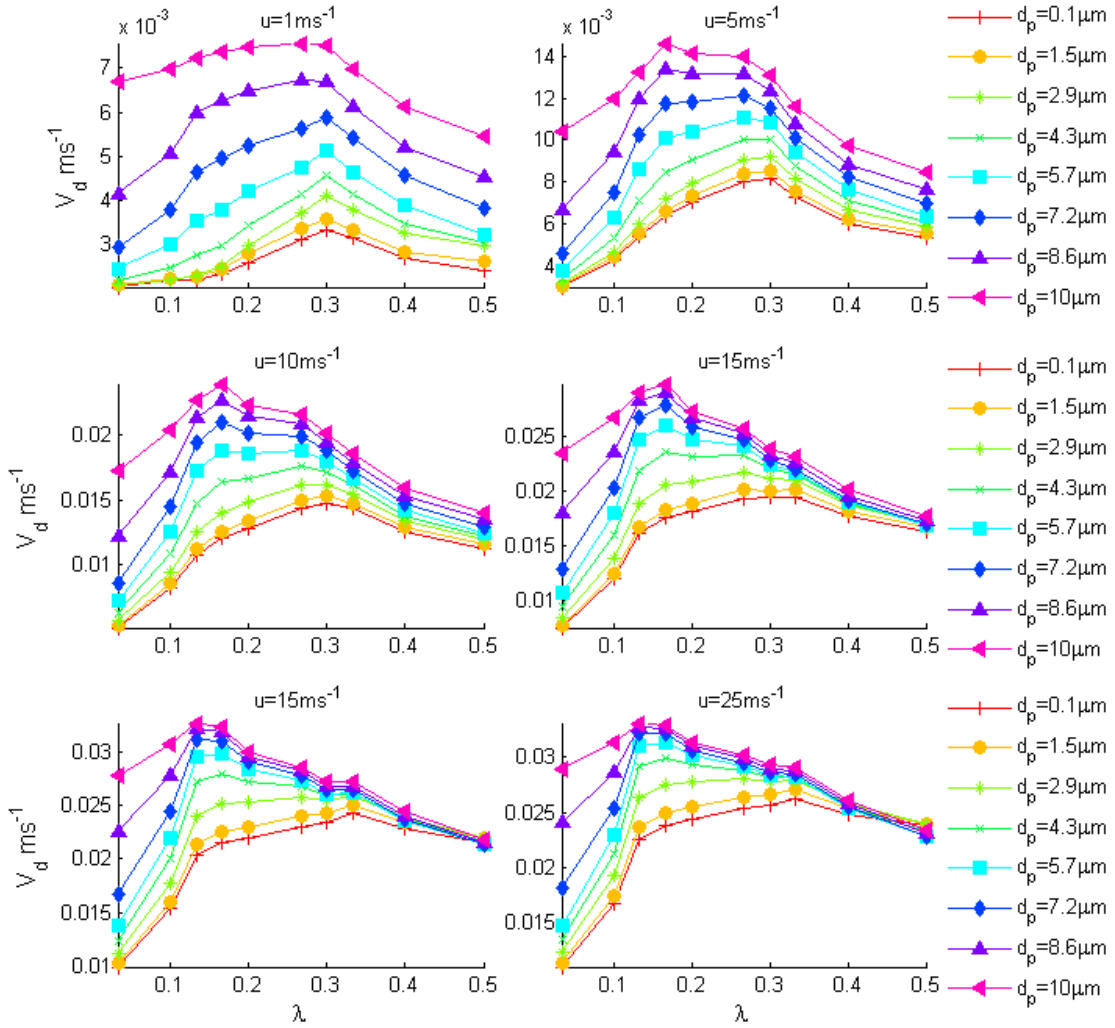


Figure 4.6 Deposition velocities versus roughness density for 8 particle diameters at six wind speeds, i.e.,  $u = 1, 5, 10, 15, 20$  and  $25 \text{ ms}^{-1}$ .

to their different inertia. Wind speed is considered as a parameter in the new expression of  $v_d$ , in the following sections, too.

Figure 4.6 shows peaks of  $v_d$  between 0.133 and 0.3. These peaks coincided with the peaks in the figures in previous chapters of air flow simulation, e.g., the curves of  $u^*$  (Figure 3.8),  $u^*/u_h$  (Figure 3.11),  $z_0/h$  (Figure 3.13), and  $z_w/h$  (Figure 3.14). From these Figures and the analyses in the previous chapters, the reason for the existence of these peaks can be explained as below:

On rough surfaces that have identical roughness elements but different roughness densities, the number of elements and the wakes behind them is proportional to  $\lambda$ , and inversely proportional to  $l$ . The increment of the number of the wakes enhances the intensity of turbulence diffusion and the momentum and mass transfer, and have positive influence on the important parameter of the flow conditions, i.e.,  $u^*$  (peak at  $\lambda = \lambda_m$ ),  $u^*/u_h$ ,  $z_0/h$ ,  $z_w/h$ , and the average and maximum value of  $v_d$ . However these quantities decrease, after  $\lambda$  exceeds the threshold of  $\lambda_a$ , as a result of

the decreasing strength of the shear flow and the dimension of the wake. Thus, these quantities all increase at first and then decrease as  $\lambda$  increases, reach their peak around  $\lambda_m$ . The value of these peaks are around 0.133 - 0.2, where the gradient of the increment of these quantities due to the increasing number of elements and the reduction due to the weakening shear flow become equivalent.

In sum, these drag and the height scales share the same trend changing with  $\lambda$ . This phenomena proves that these quantities over rough surfaces are mutually related. Thus, it validates the theory that the influence of the wake associates the surface condition with the flow condition. It also proves that the transport of mass and momentum share the same mechanism of shear transportation on rough surfaces.

Comparing to existing model estimations, the magnitude of the acquired deposition velocity on a rough surface is much larger than that on a smooth surface (Kouznetsov & Sofiev, 2012; Slinn & Slinn, 1980; Slinn, 1982; Zhang et al., 2001). Typical deposition velocities on smooth surfaces are  $10^{-4}$  to  $10^{-2} \text{ ms}^{-1}$ , and  $10^{-2}$  to  $10^0 \text{ ms}^{-1}$  on rough surfaces. The collection velocity of interception and Brownian diffusion mechanisms cannot reach the magnitude of  $v_d$  simulated on rough surfaces. The shear transport become the main mechanism of deposition over rough surfaces. The strength of shear varies on different surfaces under different wind speeds, the response of  $v_d$  also differs for different sizes of particles.

#### 4.5.2.2 Dependency of deposition velocity on wind speed

It is assumed, that  $v_d$  depends on wind speed. According to the study of Chamberlain (Chamberlain, 1967), if  $F$  is the downwards flux of particles, we can write:

$$F - v_g C(z) = K(z) \frac{dC(z)}{dz} \quad (4.7)$$

where  $K(z)$  is the diffusivity coefficient, which includes Brownian diffusion and turbulence diffusion. Assuming that the diffusivity coefficient for mass and momentum are analogous, then

$$K(z) = \kappa u_* z \quad (4.8)$$

by integration of Equation (4.8):

$$\frac{v_g}{\kappa u_*} \ln(z) = -\ln\left(\frac{F - v_g C(z)}{A}\right) \quad (4.9)$$

The top of the element and the wake serve as an effective sink for particles, as  $C(h) = 0$  which is the concentration of particle  $c$  at  $h$ , then Equation (4.9) can be rewritten as

$$\frac{F - v_g C(z)}{F} = \left(\frac{h}{z}\right)^\alpha, \quad \alpha = \frac{v_g}{\kappa u_*} \quad (4.10)$$

The  $v_d$  is then

$$v_d(z) = \frac{F}{C(z)} = \frac{v_g}{1 - \left(\frac{h}{z}\right)^{\alpha}} \quad (4.11)$$

It is convenient to define the dimensionless deposition velocity and the resistance to mass transfer,

$$v_d^+(z) = \frac{v_g(z)}{u_*} \quad (4.12)$$

$$r^+(z) = \frac{u_*}{v_g(z)} \quad (4.13)$$

Then,

$$r^+(z) = \frac{1 - \left(\frac{z}{h}\right)^{-\alpha}}{\kappa\alpha} \quad (4.14)$$

in the limiting cases, when  $v_g$  is very small or  $u_*$  is very large,  $\alpha$  tends to be zero, according to (Chamberlain, 1967), as

$$r^+(z) = \frac{u(z)}{u_*} + \frac{1}{\kappa} \ln(z_0/h) \quad (4.15)$$

It is related to the roughness layer's Stanton number  $B$  by Owen & Thomson (Owen & Thomson, 1963) who wrote:

$$B^{-1} = \kappa^{-1} \ln(z_0/h) \quad (4.16)$$

Therefore, the resistance to mass transfer could be written as

$$r^+(z) = f^+(z) + B^{-1} \quad (4.17)$$

where  $f^+(z) = u(z)/u_*$  is the dimensionless resistance to momentum transfer. If the boundary condition of mass and momentum transfer is at the same place,  $z_0 = h$ , or  $B^{-1} = 0$ , we have  $r^+(z) = f^+(z)$ , and

$$v_d(z) = \frac{u_*^2}{u(z)} \quad (4.18)$$

In fact, the transfer of particles may be several times faster than the momentum transfer when the collection process on the rough surface is considered. For simplicity,  $v_d$  and  $u_r$  are defined at the same reference height, as:

$$v_d = c \frac{u_*^2}{u_r} \quad (4.19)$$

And for larger particles, when gravitational settling is considered and  $v_g$  is large, the deposition velocity will be further increased. The value of  $c$  and expression of  $v_d$  are analyzed with simulation data for different wind speeds, in the next section.

### 4.5.2.3 Deposition velocity versus the wind speed

The relationships among  $u_*$ ,  $u_r$ , and  $v_d$  are not linear, when  $\lambda$  or  $d_p$  is considered (see Figure 4.5 and Figure 4.6). Thus, to deduce the deposition velocity on all surfaces, the average values of  $v_d$  must be determined at first. The mean  $v_d$  are measured during the 3D simulation, and they are deduced as functions step by step.

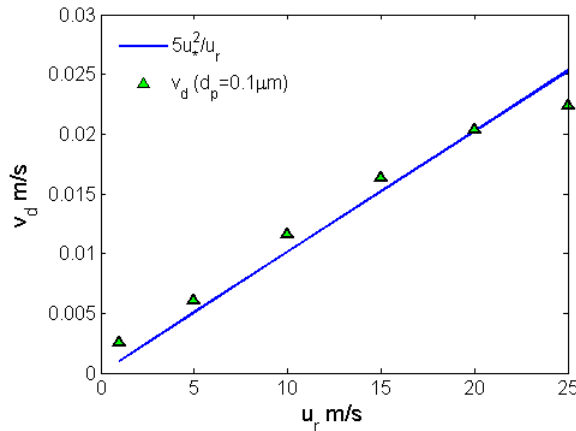


Figure 4.7 Deposition velocity for small particles ( $d_p = 0.1 \mu\text{m}$ ), averaged on all surfaces for each wind speed

When particles are very small ( $d_p = 0.1 \mu\text{m}$ ), their motion follow the air flow, thus the deposition velocity for these particles is:

$$v_d = \frac{5u_*^2}{u_r} \quad (4.20)$$

where  $u_*$  and  $u_r$  are determined in Chapter 3, and the constant 5 is determined for particle with  $d_p = 0.1 \mu\text{m}$ . The comparison between the estimation of Equation (4.20) and the simulated deposition velocity for each wind speed is presented in Figure 4.7, which shows consistency.

However, larger particles tend to divert from the main flow, and their deposition velocities may increase, as shown in Figure 4.8 of  $d_p = 10 \mu\text{m}$ . The estimation of deposition velocity for larger particles and the fitting function is

$$v_d = 0.45 \left( \frac{u_*^2}{u_r} \right)^{0.5} \quad (4.21)$$

It is shown in Figure 4.8. Both of the fitting curves in Figure 4.7 and Figure 4.8 have the correlation coefficient  $R^2 = 0.98$ .

Equation (4.20) and (4.21) set the conditions for the  $v_d$  for smallest and largest sizes of particles. The  $v_d$  of larger particles is relatively larger than for smaller particle, with different trends versus  $u_r$ . Equation (4.21) of  $v_d$  for large particles is a novel quantitative relationships, which has been identified in the deposition process.

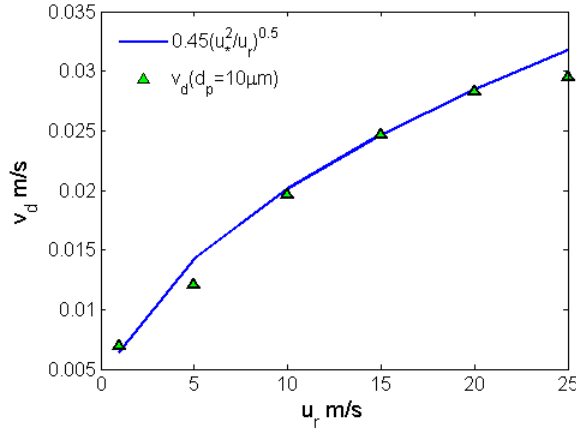


Figure 4.8 Deposition velocity for large particles ( $d_p = 10 \mu\text{m}$ ), averaged for all of the surfaces for each wind speed.

#### 4.5.2.4 Deposition velocity versus roughness density

Figure 4.9 and Figure 4.10 show the measurement and estimation of deposition velocities at 6 wind speeds over sparse ( $\lambda = 0.033$ ) and dense surfaces ( $\lambda = 0.5$ ), respectively. The data of  $v_d$  in these two figures indicated that:

- (a)  $v_d$  increases as the wind speed increases.
- (b) on dense surfaces ( $\lambda = 0.5$ ),  $v_d$  is not sensitive for the particle size;
- (c) on sparse surfaces ( $\lambda = 0.033$ ),  $v_d$  is similar to the deposition velocity on smooth surfaces, which increases as  $d_p$  increases.

Which are consistent with in the previous sections. Based on these characteristics, a formula of  $v_d$  for both sparse and dense surfaces is proposed:

$$v_d = \frac{a_1 d_p^2}{0.001 + 10d_p} + a_2 + v_g \quad (4.22)$$

Here  $a_1$  and  $a_2$  are fitting coefficients.  $v_g$  is the terminal velocity of particle (see Equation (1.18)). The fitting parameters of  $a_1$  and  $a_2$  for Equation (4.22) with various parameters from the simulation data are shown in Table 4.2.

	$u = 1 \text{ ms}^{-1}$	$5 \text{ ms}^{-1}$	$10 \text{ ms}^{-1}$	$15 \text{ ms}^{-1}$	$20 \text{ ms}^{-1}$	$25 \text{ ms}^{-1}$
$\lambda = 0.033$	$a_1$	0.0017	0.029	0.079	0.126	0.15
	$a_2$	0.00158	0.0023	0.0044	0.0066	0.009
$\lambda = 0.5$	$a_1$	-0.011	-0.009	-0.013	-0.03	-0.045
	$a_2$	0.0025	0.0054	0.0012	0.017	0.022

Table 4.2 Fitting coefficients in the expressions of  $v_d$  for dense surface ( $\lambda = 0.5$ ) and sparse surface ( $\lambda = 0.033$ ) at six wind speeds, for Equation (4.22).

The field measurement of  $v_d$  over tall canopies could be taken as the measurement on dense surfaces. In this case,  $v_d$  is usually greater than the measurement on the smooth surfaces and low canopies (Gallagher et al., 1997; Hussein et al., 2009; Zhang & Li, 2008). This is also observed in the simulation, in which  $v_d$  is not sensitive to  $d_p$ , see Figure 4.3. This consistency confirms that the simulation has successfully reproduced the deposition processes.

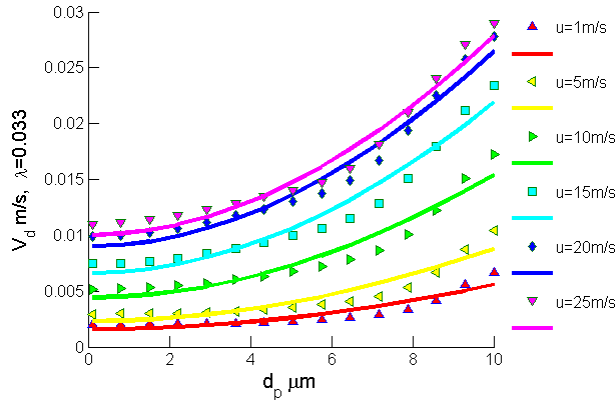


Figure 4.9 Deposition velocity on a sparse surface for  $\lambda = 0.033$  at six wind speeds 1, 5, 10, 15, 20, and 25  $\text{ms}^{-1}$ , symbols are simulation data, curves are fitting results

On a smooth surface,  $v_d$  is usually considered to be a function of particle size, i.e.,  $d_p$ . And the result of the simulated  $v_d$  on a very sparse surface is similar to that on a smooth surface. The simulation and fitting results are compared to field data to be validated.

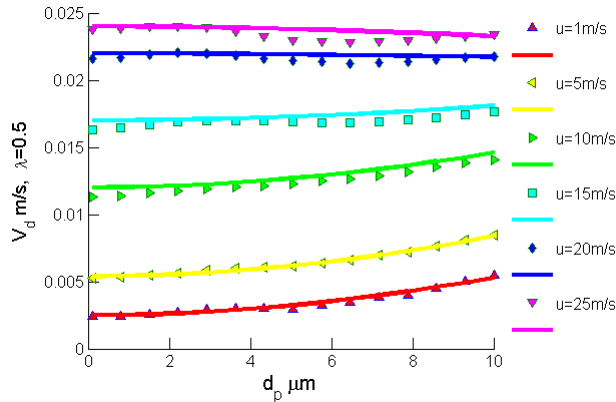


Figure 4.10 Deposition velocity on dense surfaces ( $\lambda = 0.5$ ) under 6 wind speeds 1, 5, 10, 15, 20, and 25  $\text{ms}^{-1}$ , symbols are simulation data, curves are fitting results

### 4.5.3 Estimations versus field measurements

The  $v_d$  in the previous sections are limited to a range of 0.1 to 10  $\mu\text{m}$ , but it is possible to extend the simulation result to 100  $\mu\text{m}$  based on the understanding of the deposition process. The main mechanisms of deposition for large particles ( $d_p > 5 \mu\text{m}$ ) are gravity settling (Kouznetsov &

Sofiev, 2012; Slinn, 1982; Zhang & He, 2013) and the acceleration due to shear flow induced by the roughness elements, i.e., shear transportation. According to the definition of terminal settling velocity  $v_g$ , a particle reaches  $v_g$ , in absence of vertical flow. Which means that only one of the two mechanism, gravitational settling and shear transportation, dominates the deposition process for each size range of particles. Therefore, we simply assume that  $v_d$  is the same as estimated by Equation (4.22), when it is larger than  $v_g$ , or  $v_d = v_g$  when the estimation of  $v_d$  is smaller than  $v_g$ . Therefore,

$$v_d = \max\left(\frac{a_1 d_p^2}{0.001 + 10d_p} + a_2 + v_g, v_g\right) \quad (4.23)$$

Equation (4.23) includes the two main mechanisms, and these two mechanisms are effective for different size ranges, the gravity settling is critical only when the shear transportation is less effective, vice versa. The parameter of  $a_1$  and  $a_2$  for the surfaces of  $\lambda = 0.033$  and  $\lambda = 0.5$  are listed in Table 4.2.

The extended estimation of  $v_d$  (Equation (4.23)) and the field measurements of deposition velocities are shown in Figure 4.11 (Beswick et al., 1991; Gallagher et al., 1997a; Gallagher et al., 1992; Grosch & Schmitt, 1988; Joutsenoja, 1992; Lorenz & Murphy Jr, 1989; Waraghai & Gravenhorst, 1989). The values of  $v_d$  on the dense surface of  $\lambda = 0.5$  and the sparse surface of  $\lambda = 0.033$  are compared with a series of field experimental data.

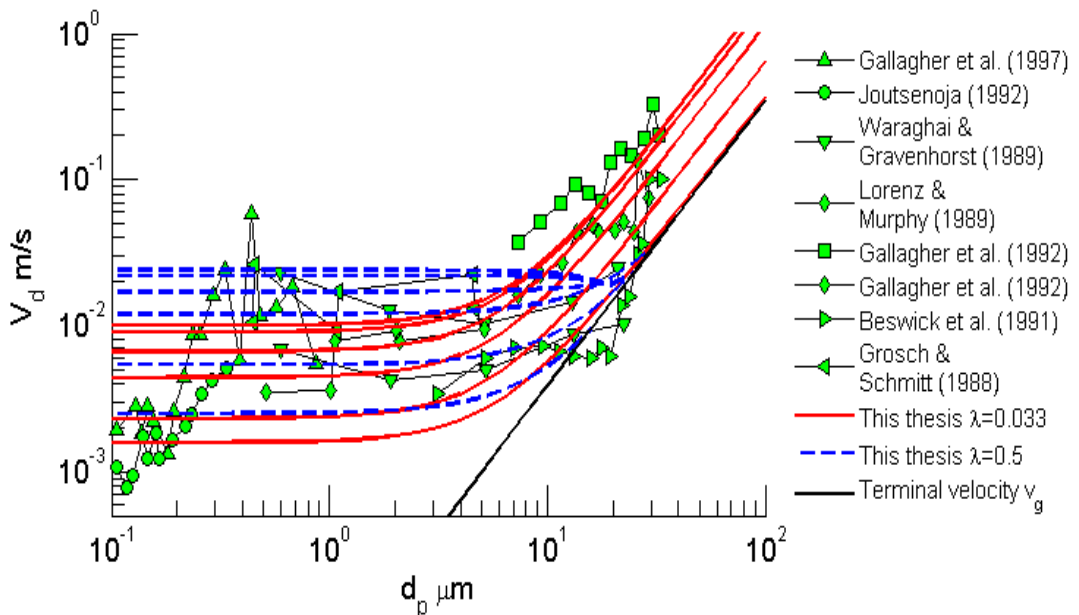


Figure 4.11 Deposition velocity from field experimental results and the estimation from this paper. The deposition velocity from simulation increase as wind speed increase, simulation results for 2 surfaces ( $\lambda = 0.033$  and  $\lambda = 0.5$ ) under 6 wind speeds ( $1 - 25 \text{ ms}^{-1}$ ) are shown, the wind speeds are the same as in Figure 4.9 and Figure 4.10.

The two major discrepancies of previous models, i.e., the underestimation of  $v_d$  for large particles and medium-sized particles (Section 4.3.4), are corrected by the new improvements:

- (a) The  $v_d$  for large particles is accelerated by the shear flow, the increment can be more than 10 times of  $v_g$ . The simulated  $v_d$  on sparse surface for large wind speeds is close to the field measurement.
- (b) The  $v_d$  for smaller particles from field measurements, are in the same range as the presented simulation data.

Although the field measurement were acquired over complex surfaces and wind conditions, the simulation and estimation results are consistent with these measurements. This means that, all of the complex field conditions can be predicted by choosing correct  $\lambda$  of the rough surfaces and the wind speeds correctly. The estimated data shown in Figure 4.11 are the first successfully reproduced  $v_d$  on rough surfaces with high canopies.

In the expressions of  $v_d$  in Equation (4.23), the surface collection processes as well as the resistances of different layers has not been applied. They are not as efficient as the mechanisms of gravity settling or shear transportation in the roughness layer, as discussed in Section 4.3.4.

The  $v_d$  in multiple conditions are well reproduced;  $v_d$  on surfaces with  $0.1 \mu\text{m} < d_p < 10 \mu\text{m}$ ,  $0.033 < \lambda < 0.5$  and  $1 \text{ ms}^{-1} < u < 25 \text{ ms}^{-1}$  can be looked up in the table in the Appendix; the expression of  $v_d$  for  $d_p = 0.1 \mu\text{m}$ ,  $d_p = 10 \mu\text{m}$ ,  $\lambda = 0.033$  and  $\lambda = 0.5$  are deduced. Clearly, the new estimation of the deposition velocity agrees well with experimental data, and our understanding of the deposition onto rough surface has been improved.

However the data of Gallagher et al. (1992), shows different trend of  $v_d$  changing with  $d_p$  for small particles. This might be caused by their measuring technique or complex nature conditions. The next chapter will look into this discrepancy.

## 4.6 Conclusion

In contrast to the existing method of characterizing a rough surface as a single cylinder, a more complete and reasonable simulation dataset of deposition velocity on rough surfaces is presented. Wide ranges of wind speed, roughness densities and particle sizes are considered. The simulated deposition velocity agrees well with field measurements. The deposition velocity of different rough surfaces can be looked up in the table in the Appendix, including the parameters of roughness densities of the surfaces, wind speeds and particle sizes. In addition to the advantage of linking different surfaces with a roughness density, it is a novel approach to apply the wind speed and roughness density as parameters in the expression of the deposition velocity.

The magnitude of the acquired deposition velocities on rough surfaces are much larger than on smooth surfaces. The typical deposition velocities are  $10^{-4}$  to  $10^{-2} \text{ ms}^{-1}$  on smooth surfaces, whereas it is  $10^{-2}$  to  $10^0 \text{ ms}^{-1}$  on rough surfaces. The collection velocity of interception, Brownian diffusion, etc., cannot reach a magnitude of deposition velocity on a rough surface. Therefore, the shear transportation over rough elements is the main mechanism of deposition.

The expression of  $v_d$  as functions of  $u_r$ ,  $u_*$ ,  $\lambda$  and  $d_p$  are deduced. These Equations are simpler than the previous models and are suitable for reproducing the features of rough surfaces.

It's worth noticing that, the important parameters of the flow, i.e.,  $u^*$ ,  $u^*/u_h$ ,  $z_0/h$ ,  $z_w/h$ , and  $v_d$  all shows peaks at  $\lambda_m$ . Despite the nonlinearity in the deposition process. It is reasonable that this coincidence indicate that the momentum transfer and mass transfer are physically similar, and they are all subject to the mechanism of shear transportation.

Further studies could conduct more simulations or measurements on rough surfaces with different lengths of roughness elements, different transverse distances between elements or different shapes of elements. With these additional data it may provide a complete Eulerian model for deposition prediction under all types of conditions.

# 5. Deposition in natural conditions

*Based on 1D simulations of vertical dispersion*

## 5.1 Intermittent deposition process

The previous chapter studied the deposition process under steady states. However, in natural conditions, the wind speed and the dust flux are not steady (Gallagher et al., 1997a). The field measurements of deposition in natural condition is usually two orders of magnitude larger than laboratory measurements. And a peak of deposition velocity is shown for particle of size of  $d_p = 0.5 \mu\text{m}$ . Scientists claim that the result of field measurements are unable to be interpreted, as they show different trend changing with particle size as in laboratory measurement (Kouznetsov & Sofiev, 2012; Petroff et al., 2008; Zhang et al., 2001). However, this might be caused by the measuring technique or unsteadiness in natural conditions.

The unsteadiness is often recognized as intermittency. The intermittency of flow is known as the sudden change of a periodic flow or un-periodic nature of a flow (Frisch, 1995). The intermittent flow can be treated as a mixing of various states of steady flow. The steady state of flow can only be assumed as valid for a short time period. The effect of intermittent dust flux on deposition velocity can be considered in simulation.

The widely used field measuring technique of eddy correlation method has certain problem. This chapter addresses the influence of intermittent dust flux and the measuring technique on  $v_d$ . The aim is to explain the influence of the influences on the size resolved deposition velocity, and understand the results of a field measurement. A 1D simulation of dry deposition based on a vertical dispersion model and a measurement of intermittent dust flux is conducted. The result of sized resolved deposition velocity agrees well with field measurement. And the understanding of the uncertainties in measurement are improved.

Section 5.2 introduces the vertical dispersion model. In Section 5.3, a simulation of deposition in nature condition is conducted, with a field-measured data as input. Necessary parameters are acquired from the 3D simulation of the air flow over rough surfaces, from Chapter 3. The result of the simulation is consistent with the measured deposition velocity in the field experiment. Section 5.4 concludes this chapter.

## 5.2 A framework of the vertical dispersion

Kouznetsov and Sofiev (Kouznetsov & Sofiev, 2012) proposed an approach of vertical dispersion based on an exact solution of the steady state equation for aerosol flux in the boundary layer. This approach considers large and small particles and the transition from the smooth regime to the rough regime, by using two length scales to characterize the rough surface: the aerodynamic roughness and the collection scale. It approaches the deposition velocity on smooth surface without empirical parameters, and its estimation on low canopies is reasonable. As the collection length approaches the surface with a single cylinder in the same way as other models, its comparison with data on high canopies shows large uncertainties. It is not the perfect solution for deposition on a rough surface. However it is the latest reliable model for deposition on a smooth surface and a sparse rough surface. It estimates the vertical dispersion of small particles and the vertical distribution of concentration and flux.

Although the deposition model proposed in Chapter 4 fit well with simulation data over dense surfaces, it does not provide estimation of  $v_d$  at different heights. Therefore, the model of Kouznetsov and Sofiev (Kouznetsov & Sofiev, 2012) is used to test the influence of intermittency and the measuring technique on  $v_d$ . The detail of this model is as follows.

Vertical transfer of particles can be modeled by assuming that turbulent transfer and gravitational settling can be added together as follows (Csanady, 1963)

$$F(z) = -K(z) \frac{dC(z)}{dz} + v(z)C(z) \quad (5.1)$$

When the vertical velocity is assumed to be zero, there is a simpler form of flux:

$$F(z) = -K(z) \frac{dC(z)}{dz} \quad (5.2)$$

which is easy to solve when the concentration is defined as:

$$C(z) = -J(z) \int_0^z \frac{dz}{K(z)} \quad (5.3)$$

For simplicity, a resistance is defined as:

$$r(z) = \int_0^z \frac{dz}{K(z)} \quad (5.4)$$

And when the constant flux is assumed,

$$J(z) = \frac{C(z)}{1 - \exp(vr)} v \quad (5.5)$$

The resistance below height  $z_l$  is:

$$r(z) = \int_0^{z_1} \frac{dz}{K(z)} \quad (5.6)$$

Zero concentration on the bottom surface and the constant flux hypothesizes cannot be assumed for Equation (5.2). Therefore, Equation (5.2) is only applicable for two generic atmospheric layers with a constant flux. However, there is a straightforward solution for the deposition flux (Equation (5.1)):

$$F_{ij}(z) = \frac{C(z_j)J(z_i, z_j) - C(z_i)}{\int_{z_i}^{z_j} J(z_i, z_j)/K(z) dz} \quad (5.7)$$

where  $z_i$  and  $z_j$  define a range of height with a constant flux, and  $J$  refers to:

$$J(z_i, z) = \exp\left(\int_{z_i}^{z_j} \frac{v(z)}{K(z)} dz\right) \quad (5.8)$$

And the resistance between these two heights is:

$$r_{ij} = \int_{z_i}^{z_j} \frac{dz}{K(z)} \quad (5.9)$$

These are the solutions for the steady state equations. However, for an unsteady state, it may only be assumed that the steady state remains for a short period of time, similar to the assumption that the constant flux exists only between two heights. Then, the deposition velocity is:

$$\frac{1}{v_d(z_j)} = \frac{1}{J(z_i, z_j)} \left( \frac{1}{v_d(z_i)} + \int_{z_i}^{z_j} J(z_i, z_j)/K(z) dz \right) \quad (5.10)$$

When  $v$  is constant, the deposition velocity is simply:

$$\frac{1}{v_d(z_j)} = \frac{1}{v_d(z_i)} \exp(-vr_i) + \frac{1}{v} (1 - \exp(-vr_i)) \quad (5.11)$$

The integration of  $r_{ij}$  requires a correct estimation of the diffusivity  $K(z)$  as a function of height. While inside the roughness layer and in the aerodynamic layer, the profile of diffusivity are different. (See Equation (1.8).)

It is not possible to determine the exact value of  $z_w$  in a field measurement. Without a working theory for estimating  $z_w$ , the value of  $z_w$  is chosen arbitrarily in previous models (Kouznetsov & Sofiev, 2012). Here the value  $z_w$  is chosen as the medium value from the simulation result in Chapter 3, i.e.,  $z_w/h=1.3$ , as an average value for mixed sparse and dense surfaces in nature.

## 5.3 Deposition in the intermittent condition

### 5.3.1 Experimental data of Gallagher (1997)

Gallagher et al. (1997) measured  $v_d$  during the summer of 1995 on a Speulder Forest site in The Netherlands with an average height of canopy of 18 m. The measuring heights were 18m and 25m, and  $u_* = 0.56 \text{ ms}^{-1}$ . Their measurements by eddy correlation method showed a large deposition velocity, typically  $0.01 \text{ ms}^{-1}$  or more. This result contradicted existing models, which had seriously underestimated  $v_d$  for sub-micron particles. (See Figure 4.3). However, this dataset showed a clear and consistent behavior in deposition velocity across the spectrum of aerosol sizes. Its results have been cited by many authors, and it is considered as one of classic, reliable field measurements of deposition (Kouznetsov & Sofiev, 2012; Petroff et al., 2008; Zhang et al., 2001). The measured deposition velocity and flux are shown in Figure 5.1 and Figure 5.2, respectively.

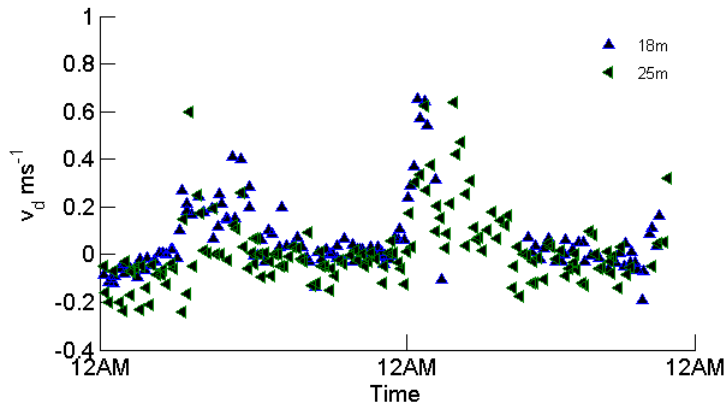


Figure 5.1 Extrapolated data of  $v_d$  from Gallagher (1997) at two heights.

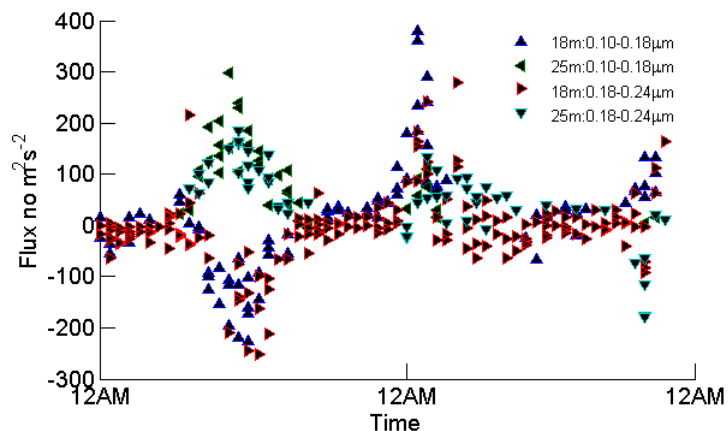


Figure 5.2 Extrapolated data of dust flux from Gallagher et al. (1997) for two size ranges of particles at two heights.

In Gallagher's data (1997), occasional particle emission, intense diurnal fluctuation, and intermittent fluxes are observed. The fluxes for different particles size ranges agreed well between the two heights, mainly during the day time. The maximum deposition velocities being observed is up to  $0.7 \text{ ms}^{-1}$ , with typical errors varying from 30% to 50%. The emission data are simply rejected while analyzing deposition velocity. The data measured at 25 m had less emission values, so 25 m is accepted as the reference height for deposition velocities (Gallagher et al., 1997).

However, the existence of these emission data shows the unsteadiness of the flux. In natural condition, especially regarding the diurnal process of intermittent condition, the flux will change according to the meteorological conditions as shown in Figure 5.2. This results in a discontinuous supply and influences the distribution of the concentration of dust, further disturbs the measurement of deposition velocity.

### 5.3.2 Numerical experiment

The one dimensional vertical dispersion framework is used to simulate the dust event measured by Gallagher et al. (1997), and to reproduce the size resolved deposition velocity. The parameters of  $z_w/h$ ,  $d/h$ , and  $u_*$  are carefully chosen from simulation. The domain of the simulated deposition process is the height between 18 m and 26 m, which covered the whole roughness layer when  $z_w/h = 1.3$ . The deposition flux is given by the data of the measurement. The deposition velocity is determined by the vertical dispersion model.

At each time step, the flux is assumed to be at a steady state, the deposition velocity is determined by the vertical dispersion model. The transient flux and concentration of particles are calculated from the dust supply from the top of the domain and the profile of deposition velocity. The initial flux, concentration and deposition velocity of the particles are shown in Figure 5.3 and Figure 5.4.

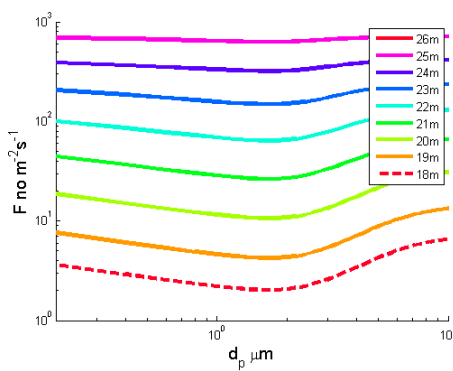


Figure 5.3 Initial flux versus particle size at different heights in the simulation.

Figure 5.3 shows small gradient of flux versus height or particle diameter. The flux of medium-sized particles is slightly smaller than that of larger and smaller particles at lower heights. The distribution of concentration in Figure 5.4 shows that the concentration of the medium-sized

particles are larger than those of other size ranges. This is a reasonable output of the model for the initial flow.

After a simulation of 48 hours, the concentration of medium-sized particles remained larger than that of other particles, and result in larger estimated flux for medium-sized particles. In the field measurements, the deposition velocity is calculated with the eddy correlation method, i.e., Equation (4.2). The result of the simulation is presented and compared to experimental data in the following section.

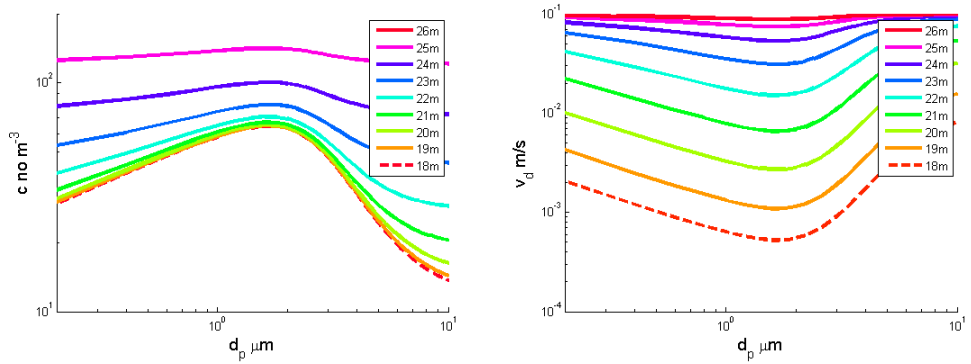


Figure 5.4 Initial concentration, and deposition velocity versus particle size at different heights in the simulation: The curves for different heights are marked by different colors, and the curve at the top of the canopy is drawn with dashed line.

### 5.3.3 Deposition velocity in natural condition

During 48 h of simulation, the deposition velocities at each height, i.e.,  $v_d(z)$ , is estimated from the vertical dispersion model (Kouznetsov & Sofiev, 2012), the flux, i.e.,  $F(z)$  is controlled by the input data (Gallagher et al., 1997), concentration is calculated by  $C(z)=F(z)/v_d(z)$ . The simulation begins at the same time as the experiment. During the simulation, diurnal variation of concentration is obvious:

At night, the dust supply is diminished to zero. The total mass and the concentration of dust, in the domain of interest, decrease according to the simulated deposition velocity. When more and larger and smaller particles are deposited due to the relatively larger deposition velocity (See Figure 4.1). The number concentration of remaining medium-sized particles become prominent (See Figure 5.4). This is the accumulation effect of medium-sized particles during negligible dust supply.

On the following day, dust flux increases for all size ranges of particles. This dust supply are the same for all particles sizes, regardless for the concentration in the domain or the deposition velocity. This is reasonable as the supply of dust is only depended on the source of dust above the domain, rather than deposition process. Note that, the model calculated deposition velocity does not increases as the flux increases. Only the concentration of dust changes due to the increment of flux. Therefore, the concentration of all size ranges of dust increase as the dust

supply increases. As the distribution of concentration is also dependent on the accumulation effect of medium-sized particles, the final concentration is the result of both the change in dust supply and accumulation effect. The influence of deposition in the day time is similar to that at night, only difference is the larger amount of deposited dust.

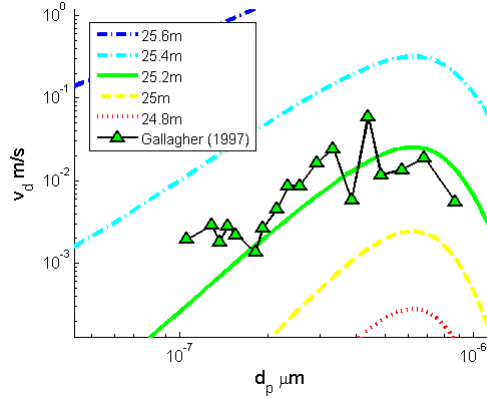


Figure 5.5 Results of  $v_d$  in the simulation with an intermittent flow condition, i.e.,  $u^* = 0.56 \text{ ms}^{-1}$ ;  $d/h=0.85$ , with  $z_w/h = 1.3$

Similar arguments can be applied to the effect of intermittent flux on dust concentration. Strong intermittent flux refers to flux in the day time and weak intermittent flux refers to flux in the night. And their influence to distribution of concentration are similar: medium-sized particle accumulates during weak flux; concentration of all particles increases during strong flux.

In the end, the concentration of medium particles is always larger than particles of other size ranges. But the exact distribution of the concentration is dependent on both deposition process and the magnitude of fluctuation of dust supply. As the flux is not constant through the boundary layer, the flux, the concentration, and the deposition velocity need to be calculated for each height. This is a nonlinear process, as described by the vertical dispersion model. Therefore, the final distribution of size resolved concentration and deposition velocity can only be revealed by the simulation. The  $v_d$  is calculated by eddy correlation method (Equation (4.2)). The simulation result combines both the diurnal effect, the effect of intermittent flux, and potential problem in eddy correlation method.

Figure 5.5 shows the final deposition velocities calculated by the eddy correlation method of Equation (5.11). The value of  $v_d$  increases as  $z$  increases. In Figure 5.5,  $v_d$  versus particle size with  $z_w/h = 1.3$  at 25.2m fit well with the measured experimental data measured. The field of high canopies may consist of a variety of  $\lambda$ , resulting in errors in the measurement of height. Thus, a difference of 0.2 m is possible. The principle trend of the measured  $v_d$  is increasing when the particle size is increasing, reaching a peak around 0.5  $\mu\text{m}$ , and then decreasing. This is consistent with the estimation of particles smaller than 1  $\mu\text{m}$  (Figure 4.3).

This result provides a possible explanation for the discrepancy between the measurement and the previous estimation of  $v_d$  in the natural condition (Figure 4.3), especially for medium-sized particles. The existence of an intense diurnal effect allows more medium-sized particles, to be

accumulated at night, and deposit during the day with larger  $v_d$ . Although at steady state, the deposition velocity is larger for the smallest and largest particles, and most of them deposit with relatively smaller velocities during the night than during the day. Even when the average concentrations of all sizes of particles are assumed to be the same. Thus the observed flux of medium-sized particles is larger than those for other particles. Since the eddy correlation method considers dust concentration to be time-averaged concentration, an overestimation of the flux will result in an overestimation of deposition velocity. Thus, although the results of this simulation contradicted to the laboratory measurements and existing model estimations, they provide results that are close to those from field measurement in the natural condition. The result of the simulation provides an explanation for the intermittent effect and error in the measurement method.

## 5.4 Discussion and Conclusion

The unsteady supply of dust and its influence on the deposition process is simulated and analyzed. By changing the dust supply according to the field measurement, the deposition velocity is estimated for 48 h, based on a framework of vertical dispersion. The result of the simulation reproduces a field measurement and provides an explanation of the phenomenon that the  $v_d$  of medium-sized ( $0.5 \mu\text{m}$ ) particles are larger than smaller particles or larger particles'.

The largest discrepancy between the previous estimation and measurement lies in the medium-sized particles and extends to two orders of magnitude. The consideration of intermittency and the change in the dust supply explain well-known field measurement data for deposition. The largest value of the deposition velocity reaches  $0.7 \text{ ms}^{-1}$ . The concentration may increase at a rate of 5 - 6 times for different particles sizes and this result in a large variability of measurement.

Both the intermittency of the air flow and the use of an eddy correlation method are the causes of error in estimated  $v_d$ . The intermittency in the natural flow can be accurately estimated only when the concentration and the components of the velocity are measured with high frequency instruments simultaneously. The eddy correlation method assumes that the flow is steady with an absence of vertical flow, which is not plausible in natural conditions. The eddy correlation method can estimate the  $v_d$  at close range to the real value. However, even if the transient  $v_d$  is the same as estimated in existing models, the resulting measurement may result in a different pattern due to errors (Figure 4.3). The measurement of deposition in natural condition, usually lasts for a long time and usually includes days and nights. It is impossible to ignore the diurnal changes in meteorological conditions, e.g. the wind speed or the dust flux.

In sum, to improve the correct estimation of the  $v_d$  under natural conditions, it is necessary to consider the intermittency of the dust flux. To improve the measurement of the  $v_d$  under natural conditions, the eddy correlation method is not enough; a simultaneous measurement of the flux and concentration will reduce the error. Only when all of these possible disturbances to the measurement are considered, it is possible to represent realistically the process.

# **6. Conclusion and recommendations**

## **6.1 The wake and the parameter of $\lambda_a$**

The wakes behind the roughness elements are found to be the key link in the path of momentum transfer from the air flow to rough surface. The dimension of the wakes associate the geometry of the surface and drag on surface. In the 2D and 3D simulations of flow over isolated elements, the length of wake are measured. The height-to-length ratio ( $\lambda_w$ ) of the wakes is found to be independent from the height of roughness elements ( $h$ ), and  $\lambda_w$  is a constant when the wake is a full wake. In 3D cases, the wakes are full wake. Therefore, a constant value, i.e.  $\lambda_a$ , can be used in the new drag theory to quantify the condition of flow on surfaces with different roughness densities and wind speeds.

It is also found that, when the distance between elements equals to the length of wake, the strength of shear flow on the element is equivalent to the strength of shear flow on the underlying surface. Thus, when  $\lambda = \lambda_a$ ,  $\lambda_a = \lambda_w$ , and  $F_r = F_s$ . This means that the equilibrium of shear stress on the wake is also applicable to the whole surface, when the whole surface is covered by the wakes. This finding is the key to associate the strength of shear flow with the dimensions of the wakes.

The wake is unique on surface with certain type of roughness element. Therefore,  $\lambda_a$  can be used to distinguish different elements with different  $b/h$ . This feature of  $\lambda_a$  allows the new drag theory to distinguish the measurement on different rough surfaces in the classical wind tunnel experiment of Marshall (1997). This is also the first time that scientists can understand the difference among these measurements.

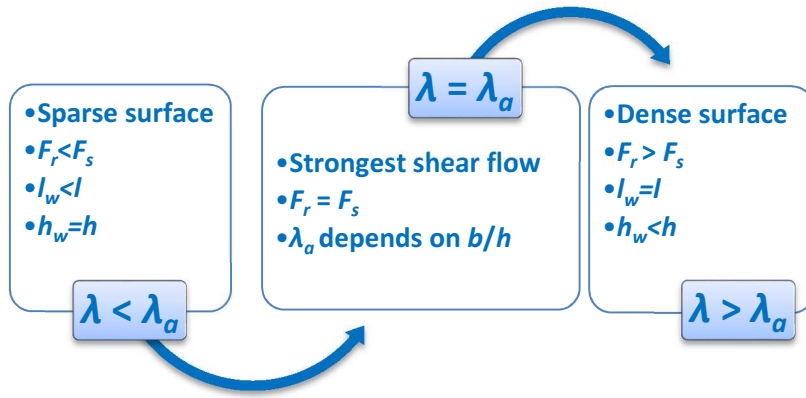


Figure 6.1 Relation among the roughness density, drag and  $\lambda_a$ . (See Chap. 2 and 3)

In the 3D simulations on surface with ridge elements of  $b/h=1$ , the wakes tend to have the similar size approximately 9 times its length ( $L_w = 9b$ ), and  $\lambda_a = h/L_w = 1/9$ . In the experiments on surface with 3D elements,  $\lambda_a$  is dependent on  $b/h$ . These results supported the discovered physical meaning of  $\lambda_a$ .

To sum,  $\lambda_a$  is an important parameter and has multiple physical meanings and applications, as:

- The height-to-length ratio of the wake behind isolated elements;
- The roughness density of the surface with  $F_r = F_s$ ;
- The threshold roughness density, which distinguishes dense and sparse surfaces;
- A function of  $b/h$  of roughness element; and,
- A new parameter in the new drag and drag partition theory.

When the  $\lambda$  exceeds  $\lambda_a$ , the surface turns from a sparse surface to a dense and the wakes are restrained by the distance between the element, and  $\lambda_w = \lambda_a$ . And  $\lambda_a$  is used to quantify the size of the wake and distinguish roughness elements in the 3D simulation. The findings regarding  $\lambda_a$  are listed in Figure 6.1.

Another parameter of  $\lambda_m$ , is defined as the roughness density of the surface which has largest drag. It is expressed as a function of  $\lambda_a$ ,  $\tau_{rr}$  and  $\tau_{s0}$ .

## 6.2 The new drag and drag partition theory

The new drag and drag partition theory is a physical theory, all parameters in its expressions are measurable physical quantities. A physical theory represents the law of nature, and its applications covers a wide ranges of possible conditions.

The new theory is based on the improved understanding of the structure of air flow over rough surfaces. Which includes the new parameter of  $\lambda_a$  and a resistance method. The flow in the canyon layer is analyzed using a resistance method. The relationship among three parameters: the square of the velocity difference between two heights, the momentum flux and resistances to momentum flux are found. When the momentum flux refers to electric current, the square of

velocity difference refers to voltage gradient and a resistance as the resistance, these three parameter can be expressed in a same way as Ohm's law (Equation 3.13).

The resistances are deduced for each parts of the surfaces. A rough surface is divided into the elements and the underlying surface. The novel point of this method is the resistance analogue in the canyon layer. The resistance is used to deduce drag and drag partition. As the resistances are independent from wind speed or drag, they are eliminated during the deduction of the new drag theory and do not appear as empirical parameters.

The new physical model is presented in Section 3.3. The new equations of friction velocity, total shear stresses and shear stress partitions are presented in fractional functions. The friction coefficient is also deduced. The disadvantages caused by the exponential functions, which chosen by previous theories, are avoid. The parameters of  $\lambda$ ,  $\lambda_a$ , and  $u_r$  are considered in the new expressions. The use of  $\lambda_a$  allows the new model to distinguish the drag partitions on surfaces with different elements with different  $b/h$  ratios for the first time (Figure 6.2). The existing theory of drag and drag partition can be considered produces the same result as the new theory, when  $b/h=1$ .

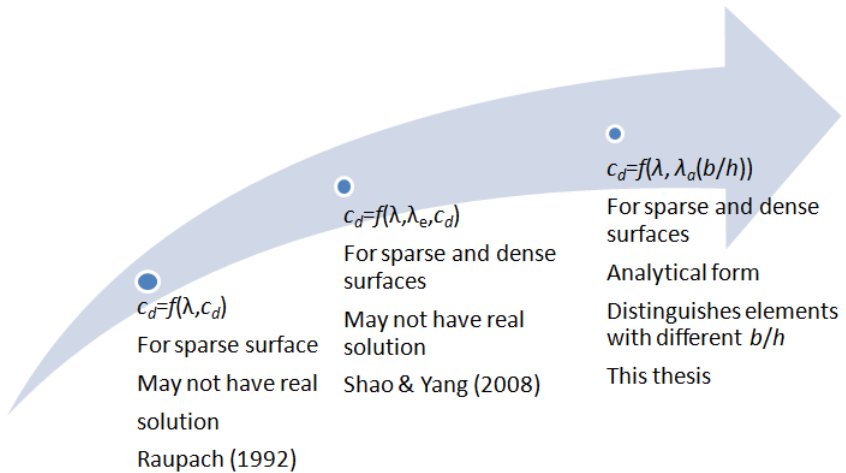


Figure 6.2 The evolution of Drag and Drag partition Theories. (Chapter 3)

The new theory of drag and drag partition is validated by classical experimental data and 3D simulation data. The key contributions of this theory are the improvements to the basic form of the drag partition equation and the introduction of a parameter for the flow condition on surfaces, i.e.,  $\lambda_a$ . With  $\lambda_a$  as a parameter for identical wakes behind certain element shapes, the shape of element can be brought to the expression of drag partition together with a physical meaning. This improvement is critical for extending the drag and drag partition theory to more complex surfaces with different element sizes and shapes.

## 6.3 Deposition velocity on rough surfaces

A new deposition velocity dataset over rough surfaces is acquired, based on 3D simulation of particle laden flow on rough surfaces with regularly distributed elements. The deposition velocity on surfaces with different roughness densities, different particle sizes, under different wind speeds are simulated and categorized. The simulated deposition velocity agrees well with field measurements. A complete dataset for all of these varieties of conditions is listed in a table in the Appendix. Deposition velocity of certain particle size on certain surface under certain wind speeds can be looked up in these tables.

With proper analysis of the momentum transfer from the atmosphere to rough surfaces in previous chapters, the expressions of deposition velocity as functions of wind speed, particle size or roughness densities are proposed. These equations are in simpler terms comparing to previous models and are more suitable for rough surfaces. The main parameters in the deposition model are shown in Figure 6.3.

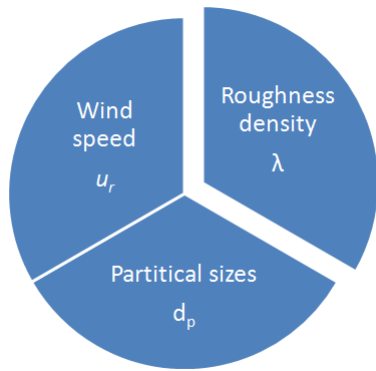


Figure 6.3 The main parameters in the deposition model,  $\lambda$  is the new parameter. (see Chapter 4)

The magnitude of the deposition velocity data on rough surfaces are much larger than on a smooth surface. The typical deposition velocity is  $10^{-4}$  to  $10^{-2} \text{ ms}^{-1}$  on a smooth surface, whereas it is  $10^{-2}$  to  $10^0 \text{ ms}^{-1}$  on rough surfaces. The collection velocity of interception, Brownian diffusion mechanisms cannot reach a magnitude of deposition velocity on a rough surface. Therefore, the shear transportation and gravitational settling are the main mechanism of dry deposition. This result agrees well with field measurements and successfully explains the mechanism of deposition on rough surfaces.

It's worth noting that, the expression of  $v_d$  has the similar form (fractional functions) as in the expression of the new drag and drag partition model. Despite the nonlinearity in the deposition process, it is reasonable that the momentum transfer and mass transfer are physically similar.

## 6.4 The momentum flux and the mass flux

Generally, the fine particles follow the airflow and their diffusivities are assumed equal to momentum diffusivity (Thom, 1971). However, particles with larger inertia will not closely follow the airflow, and their diffusivities are not exchangeable. The relationship between momentum and mass transport are discussed in details in Chapter 4.

The mean value of  $v_d$  for all particle sizes first increase then decrease as roughness density increases. Therefore, the regularities of momentum and mass flux changing with roughness density are similar. The peak of  $u^*/u_h$ ,  $z_0/h$  and  $z_w/h$  also exists in the curve of  $v_d$  versus  $\lambda$  at  $\lambda_m$ . They are all associated by the shear flow in the roughness layer and the dimension of the wake on rough surfaces.

For different particle sizes. On smooth surface, deposition velocity is larger for larger particles, due to the larger inertia (Chamberlain, 1967). On a rough surface, the motion of particles is more complex because of the shear flow induced by the elements. The diagrams of Reynolds stress from the 3D simulation data show pairs of positive and negative regions of Reynold stresses. The responses of large and small particles differ in these regions, which results in different deposition velocities for these particles. The results in Chapter 4 indicate that the difference between larger and smaller particles are larger on sparser surfaces.

A nonlinear system such as a turbulent dispersion in roughness layer and canyon layer does not necessarily have a simple linear expression, especially when many parameters and freedoms are considered. It is the unique contribution of this thesis to deduce the expression of drag as a function of  $u_r$ ,  $\lambda$  and  $\lambda_a$ ; and  $v_d$  as functions of  $u_r$  and  $d_p$ .

## 6.5 Relationship between the 2D and 3D simulation

In this thesis, both 2D and 3D simulations are conducted. The complexities of simulations in this thesis and their aims are shown in Figure 6.. Generally, the components of the flow properties in the streamwise direction are the major components and are much larger than the vertical and spanwise components. When studying the vertical transfer of momentum and mass, the vertical components are inevitable. To focus on these two main components, and to reduce the complexity of the system, it is reasonable to eliminate the transverse components.

The 2D simulation is the best way to study the streamwise and vertical components of flow properties without the spanwise components. It provide correct wind profile, which is critical to determine vertical transfer. And with fewer components, it is easier to deduce a function of these properties and easier to understand the structure of the flow. If the study of wake uses the 3D simulation data, then the spanwise width of the wake must be considered. In this case, much more simulation runs must be conducted to allow for a regression analysis of the dimension of the wakes as a function of wind speed and element shape. And, there is no guarantee for a final result of a linear relationship among these parameters as simple as in Chapter 2. Consequently, the parameters related to the wake in the expression of the drag and drag partition theory would be too complex to be applicable. Therefore, it is important to focus on the streamwise and

vertical components of flow and to use the 2D simulation to analyze the fundamental behavior of wake on rough surfaces.

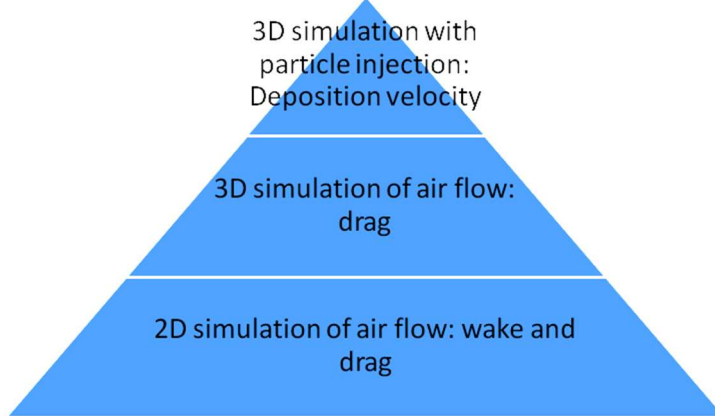


Figure 6.4 The complexities of simulations in this thesis and their aims. The 2D simulation is the fundamental study for air flow, drag and wake over rough surface; 3D simulation is more complicate, and focus on reproducing accurate drag on rough surface; the simulation with particle injection is the most complicated of all, and produces deposition velocity for multiple conditions.

A similar argument can be applied to the choice of ridges as roughness elements. The mutual sheltering of wake is considered critical to the size of the wake and surface drag; however, which type of mutual sheltering is more important, streamwise or spanwise, was not determined. As the streamwise length of the wake is larger than on other directions, this study assumes the streamwise mutual sheltering is the main restrain to the wake size, and the ridges are chosen as the roughness element to eliminate the spanwise mutual sheltering. This is one of the reasons for the simpler simulation results, which are easier to be understood and easier to be parameterized. This is also a guarantee of simple formulas of the new drag and drag partition theory as functions of a wake dimension, i.e.,  $\lambda_a$ .

The trend of parameters of wind profile changing with roughness density shows strong agreement between the 2D and 3D simulation results. The  $d/h$ ,  $z_0/h$  and  $z_w/h$  are similar in the 2D and 3D simulations, whereas  $u_{zw}$  is different between the 2D and 3D simulations. The existence of spanwise components of flow properties in the 3D simulation can be responsible for this difference.

## 6.6 Outlook

A new theory for drag and drag partition and new deposition model are presented. However, in this work, transverse heterogeneity is avoided by using 2D roughness elements of ridges. The spanwise component of the stress and spanwise mutual sheltering can affect the partition of drag, and deposition of particles. Further studies could conduct more simulations or measurements on rough surfaces of different lengths and widths of roughness elements and

with different transverse distances between elements or different length and width of elements. With these additional data, it is possible to deduce a complete model for the momentum and mass transfer for all types of surface conditions.

The deposition of particles on a rough surface suffers from insufficient experimental data, especially data with detailed descriptions of the surface and the wind profile in the roughness layer and canyon layer. New experiments are required to measure the roughness density of the surface and the wind profile close to the surface. The demanding accuracy and expense of these types of experiments will be higher than the existing field or laboratory experiments. But, only in this way the critical parameters of  $d$ ,  $z_w$  and  $\lambda$  can be determined, thereby further improve deposition models.

The study of intermittency of deposition under natural conditions requires even higher frequency of time series data, including wind speed, particle concentration and dust flux. In the future, the study on steady state dust flux will be not enough to estimate deposition in natural condition. An unsteady equation of the dust flux and velocity, as well as a frequency domain analysis are necessary to determine the high frequency responds of deposition velocity to intermittent flux (Brown et al., 2008; Brutsaert, 1975; Chamberlain, 1953).



# References

- Ahmadi, G., and S. J. Chowdhury (1991) A rate-dependent algebraic stress model for turbulence. *Applied Mathematical Modelling* 15: 516-524.
- Bache, D. (1979) Particulate transport within plant canopies—II. Prediction of deposition velocities. *Atmospheric Environment* (1967) 13: 1681-1687.
- Batchelor, G. (1970) *An Introduction to Fluid Dynamics*. Cambridge University Press.
- Belot, Y., A. Baille, and J. L. Delmas (1976) Modele numerique de dispersion des polluants atmospheriques en presence de couverts vegetaux: Application aux couverts forestiers. *Atmospheric Environment* (1967) 10: 89-98.
- Beswick, K., K. Hargreaves, M. Gallagher, T. Choularton, and D. Fowler (1991) Size-resolved measurements of cloud droplet deposition velocity to a forest canopy using an eddy correlation technique. *Quarterly Journal of the Royal Meteorological Society* 117: 623-645.
- Brown, S., W. G. Nickling, and J. a. Gillies (2008) A wind tunnel examination of shear stress partitioning for an assortment of surface roughness distributions. *Journal of Geophysical Research* 113: F02S06.
- Brutsaert, W. (1975) The roughness length for water vapor sensible heat, and other scalars. *Journal of the Atmospheric Sciences* 32: 2028-2031.
- Chamberlain, A. (1953) Aspects of travel and deposition of aerosol and vapour clouds.
- Chamberlain, A. A. C. (2012) Transport of gases to and from grass and grass-like surfaces *Atomic Energy Researchl* 290: 236-265.
- Chamberlain, a. C. (1967) Transport of Lycopodium Spores and Other Small Particles to Rough Surfaces. *Proceedings of the Royal Society A: Mathematical, Physical and Engineering Sciences* 296: 45-70.
- Chamberlain, B. A. C., R. C. Chadwick, H. Physiccr, and M. Division (1966) Transport of iodine from atmosphere to ground.
- Cheng, H., and I. Castro (2002) Near wall flow over urban-like roughness. *Boundary-Layer Meteorology* 0: 229-259.
- Cheng, H., P. Hayden, a. G. Robins, and I. P. Castro (2007) Flow over cube arrays of different packing densities. *Journal of Wind Engineering and Industrial Aerodynamics* 95: 715-740.
- Christensen, J. H. (1997) The Danish Eulerian hemispheric model—A three-dimensional air pollution model used for the Arctic. *Atmospheric Environment* 31: 4169-4191.

## References

---

- Chung, D., and D. I. Pullin (2009) Large-eddy simulation and wall modelling of turbulent channel flow. *Journal of Fluid Mechanics* 631: 281.
- Clifton, A., and M. Lehning (2008) Improvement and validation of a snow saltation model using wind tunnel measurements. *Earth Surface Processes and Landforms* 33: 2156-2173.
- Cowan, I. (1968) Mass, heat and momentum exchange between stands of plants and their atmospheric environment. *Quarterly Journal of the Royal Meteorological Society* 94: 523-544.
- Csanady, G. (1963) Turbulent diffusion of heavy particles in the atmosphere. *Journal of the Atmospheric Sciences* 20: 201-208.
- Davidson, C. I., and Y.-L. Wu (1990) Dry deposition of particles and vapors. *Acidic precipitation*, Springer, 103-216.
- Davies, J. T. (2012) Turbulence phenomena: an introduction to the eddy transfer of momentum, mass, and heat, particularly at interfaces. Elsevier.
- Davis, M. B. (1969) Climatic changes in southern Connecticut recorded by pollen deposition at Rogers Lake. *Ecology*: 409-422.
- Finnigan, J. (2000) Turbulence in plant canopies. *Annual Review of Fluid Mechanics*: 519-571.
- Friedlander, S., and H. Johnstone (1957) Deposition of suspended particles from turbulent gas streams. *Industrial & Engineering Chemistry* 49: 1151-1156.
- Frisch, U. (1995) Turbulence: the legacy of AN Kolmogorov. Cambridge university press.
- Fuchs, N. A. (1964) The mechanics of aerosols. Dover Publications.
- Gallagher, M., and Coauthors (1992) Measurements of aerosol exchange to Heather Moor. *Proc. EUROTAC Symp*, 694-669.
- Gallagher, M. W., K. M. Beswick, J. Duyzer, H. Westrate, T. W. Choularton, and P. Hummelshøj (1997) Measurements of aerosol fluxes to speulderforest using a micrometeorological technique. *Atmospheric Environment* 31: 359-373.
- Garratt, J. (1977) Review of drag coefficients over oceans and continents. *Monthly weather review* 105: 915-929.
- Garratt, J. R. (1994) The atmospheric boundary layer. Cambridge university press, 316 pp.
- Gillies, J. A., W. G. Nickling, and J. King (2007) Shear stress partitioning in large patches of roughness in the atmospheric inertial sublayer. *Boundary-Layer Meteorology* 122: 367-396.
- Ginoux, P., J. Prospero, O. Torres, and M. Chin (2004) Long-term simulation of global dust distribution with the GOCART model: correlation with North Atlantic Oscillation. *Environmental Modelling & Software* 19: 113-128.
- Giorgi, F. (1986) A particle dry-deposition parameterization scheme for use in tracer transport models. ... of Geophysical Research: Atmospheres (1984–2012) 91: 9794-9806.
- Gong, S., L. Barrie, and J. P. Blanchet (1997) Modeling sea-salt aerosols in the atmosphere: 1. Model development. *Journal of Geophysical Research: Atmospheres* (1984–2012) 102: 3805-3818.
- Gong, S., X. Zhang, T. Zhao, I. McKendry, D. Jaffe, and N. Lu (2003) Characterization of soil dust aerosol in China and its transport and distribution during 2001 ACE-Asia: 2. Model simulation and validation. *Journal of Geophysical Research: Atmospheres* (1984–2012) 108.
- Gong, S. L., and L. A. Bartie (1997) Modeling sea-salt aerosols in the atmosphere. 102: 3805-3818.
- Grant, P. F., and W. G. Nickling (1998) Direct field measurement of wind drag on vegetation for application to windbreak design and modelling. *Land Degradation & Development* 9: 57-66.
- Grimmond, C., and T. R. Oke (1999a) Aerodynamic properties of urban areas derived from analysis of surface form. *Journal of Applied Meteorology* 38: 1262-1292.
- Grosch, S., and G. Schmitt (1988) Experimental investigations on the deposition of trace elements in forest areas. *Environmental Meteorology*, Springer, 201-216.
- Hall, D., R. Macdonald, and S. Walker (1996) Measurements of dispersion within simulated urban arrays: a small scale wind tunnel study. Building Research Establishment.
- Holmes, J. D. (2001) Wind loading of structures. CRC Press.

- Holsen, T. M., and K. E. Noll (1992) Dry deposition of atmospheric particles: application of current models to ambient data. *Environmental Science & Technology* 26: 1807-1815.
- Hussein, T., A. Hruška, P. Dohányosová, L. Džumbová, J. Hemerka, M. Kulmala, and J. Smolík (2009) Deposition rates on smooth surfaces and coagulation of aerosol particles inside a test chamber. *Atmospheric Environment* 43: 905-914.
- In, H.-J., and S.-U. Park (2002) A simulation of long-range transport of Yellow Sand observed in April 1998 in Korea. *Atmospheric Environment* 36: 4173-4187.
- Incropera, F. P. (2011) Fundamentals of heat and mass transfer. John Wiley & Sons, 1052 pp.
- Jarvis, P., G. James, and J. Landsberg (1976) Coniferous forest. *Vegetation and the Atmosphere* 2: 171-240.
- Joutsenoja, T. (1992) Measurements of aerosol deposition to a cereal crop. Choularton, T., éditeur, Measurements and modelling of gases and aerosols to complex terrain. *Nat. Envir. Res. Counc.*, UK 45.
- Kastner-Klein, P., and M. W. Rotach (2004) Mean flow and turbulence characteristics in an urban roughness sublayer. *Boundary-Layer Meteorology* 111: 55-84.
- Kim, J. (1989) On the structure of pressure fluctuations in simulated turbulent channel flow. *Journal of Fluid Mechanics* 205: 421-451.
- Kouznetsov, R., and M. Sofiev (2012) A methodology for evaluation of vertical dispersion and dry deposition of atmospheric aerosols. *Journal of Geophysical Research* 117: D01202.
- Kreutzkam, B., C. Wieland, and H. Spiethoff (2012) Improved numerical prediction of ash formation and deposition using a novel developed char fragmentation model. *Fuel* 98: 103-110.
- Lai, a. C. K. (2002) Particle deposition indoors: a review. *Indoor air* 12: 211-214.
- Le, H., P. Moin, and J. Kim (1997) Direct numerical simulation of turbulent flow over a backward-facing step. *Journal of Fluid Mechanics* 330: 349-374.
- Leonardi, S., P. Orlandi, R. Smalley, L. Djenidi, and R. Antonia (2003) Direct numerical simulations of turbulent channel flow with transverse square bars on one wall. *Journal of Fluid Mechanics* 491: 229-238.
- Leuning, R., and P. M. Attiwill (1978) Mass, heat and momentum exchange between a mature eucalyptus forest and the atmosphere. *Agricultural Meteorology* 19: 215-241.
- Lighthill, J. (1975) Mathematical Biofluidynamics. SIAM.
- Liu, B. Y. H., and J. K. Agarwal (1974) Experimental observation of aerosol deposition in turbulent flow. *Journal of Aerosol Science* 5: 145-155.
- Liu, C. K., S. Klein, and J. Johnston, 1966: An experimental study of turbulent boundary layer on rough walls.
- Lorenz, R., and C. Murphy Jr (1989) Dry deposition of particles to a pine plantation. *Boundary-Layer Meteorology* 46: 355-366.
- Luo, J.-p., Z.-m. Lu, and Y.-l. Liu (2009) Simulation of Lagrangian dispersion using a Lagrangian stochastic model and DNS in a turbulent channel flow. *Journal of Hydrodynamics, Ser. B* 21: 767-773.
- Macdonald, R. W., R. F. Griffiths, and D. J. Hall (1998a) A comparison of results from scaled field and wind tunnel modelling of dispersion in arrays of obstacles. *Atmospheric Environment* 32: 3845-3862.
- Macdonald, R. W., R. F. Griffiths, and D. J. Hall (1998b) An improved method for the estimation of surface roughness of obstacle arrays. *Atmospheric Environment* 32: 1857-1864.
- Mahowald, N., and Coauthors (1999) Dust sources and deposition during the last glacial maximum and current climate: A comparison of model results with paleodata from ice cores and marine sediments. *Journal of Geophysical Research* 104: 15895.
- Mahrt, L. (1989) Intermittent of atmospheric turbulence.
- Marshall, J. (1971) Drag measurements in roughness arrays of varying density and distribution. *Agricultural Meteorology* 8: 269-292.

## References

---

- McLaughlin, J. B. (1989) Aerosol particle deposition in numerically simulated channel flow. *Physics of Fluids A: Fluid Dynamics* 1: 1211.
- Mulhern, P., and J. Finnigan (1978) Turbulent flow over a very rough, random surface. *Boundary-Layer Meteorology* 15: 109-132.
- Musick, H., and D. Gillette (1990) Field evaluation of relationships between a vegetation structural parameter and sheltering against wind erosion. *Land Degradation & Development* 2: 87-94.
- Nickovic, S., G. Kallos, A. Papadopoulos, and O. Kakaliagou (2001) A model for prediction of desert dust cycle in the atmosphere. *Journal of Geophysical Research: Atmospheres* (1984–2012) 106: 18113-18129.
- Nikora, V., K. Koll, I. McEwan, S. McLean, and A. Dittrich (2004) Velocity Distribution in the Roughness Layer of Rough-Bed Flows. *Journal of Hydraulic Engineering* 130: 1036-1042.
- O'Loughlin, E. M. (1965) Resistance to flow over boundaries with small roughness concentrations. Dissertation.
- O'Loughlin, E. M., and V. S. Annambhotla (1969) Flow phenomena near rough boundaries. *Journal of Hydraulic Research* 7: 231-250.
- Owen, P. (1969) Pneumatic transport. *Journal of Fluid Mechanics* 39: 407-432.
- Owen, P., and W. Thomson (1963) Heat transfer across rough surfaces. *Journal of Fluid Mechanics* 15: 321-334.
- Paradisi, P., R. Cesari, a. Donateo, D. Contini, and P. Allegrini (2012) Scaling laws of diffusion and time intermittency generated by coherent structures in atmospheric turbulence. *Nonlinear Processes in Geophysics* 19: 113-126.
- Peters, K., and R. Eiden (1992) Modelling the dry deposition velocity of aerosol particles to a spruce forest. *Atmospheric Environment. Part A. General Topics* 26: 2555-2564.
- Petroff, A., A. Maillat, M. Amielh, and F. Anselmet (2008) Aerosol dry deposition on vegetative canopies. Part I: Review of present knowledge. *Atmospheric Environment* 42: 3625-3653.
- Prandtl, L. (1963) The essentials of fluid dynamics. Blackie & Son Limited.
- Raupach, M., A. Thom, and I. Edwards (1980) A wind-tunnel study of turbulent flow close to regularly arrayed rough surfaces. *Boundary-Layer Meteorology* 18: 373-397.
- Raupach, M. R. (1992) Drag and drag partition on rough surfaces. *Boundary-Layer Meteorology* 60: 375-395.
- Ruijrok, W., C. Davidson, and W. Nicholson (1995) Dry deposition of particles. *Tellus B*.
- Schlichting, H. (1936) Experimentelle untersuchungen zum rauhigkeitsproblem. *Archive of Applied Mechanics*.
- Schlichting, H., and K. Gersten (2000) Boundary-layer theory. Springer, 812 pp.
- Sehmel, G., and W. Hodgson (1978) Model for predicting dry deposition of particles and gases to environmental surfaces.
- Sehmel, G. A. (1980) Particle and gas dry deposition: A review. *Atmospheric Environment* (1967) 14: 983-1011.
- Seinfeld, J. H., and S. N. Pandis (2012) Atmospheric chemistry and physics: from air pollution to climate change. John Wiley & Sons.
- Sellers, P. J., and Coauthors (1997) Modeling the Exchanges of Energy, Water, and Carbon Between Continents and the Atmosphere. *Science* 275: 502-509.
- Shao, Y. (2008) Physics and modelling of wind erosion. Vol. 37, Springer, 375 pp.
- Shao, Y., and Y. Yang (2005) A scheme for drag partition over rough surfaces. *Atmospheric Environment* 39: 7351-7361.
- Shao, Y., and Y. Yang (2008) A theory for drag partition over rough surfaces. *Journal of Geophysical Research* 113: F02S05.
- Shao, Y., and Coauthors (2003) Northeast Asian dust storms: Real-time numerical prediction and validation. *Journal of Geophysical Research: Atmospheres* (1984–2012) 108.
- Shaw, R. H., and A. Pereira (1982) Aerodynamic roughness of a plant canopy: a numerical experiment. *Agricultural Meteorology* 26: 51-65.
- Shuttleworth, W. J., and Coauthors (1984) Eddy correlation measurements of energy partition for Amazonian forest. *Quarterly Journal of the Royal Meteorological Society* 110: 1143-1162.

- Simiu, E., and R. H. Scanlan (1996) Wind effects on structures. Wiley.
- Sini, J.-F., S. Anquetin, and P. G. Mestayer (1996) Pollutant dispersion and thermal effects in urban street canyons. *Atmospheric Environment* 30: 2659-2677.
- Slinn, S. a., and W. G. N. Slinn (1980) Predictions for particle deposition on natural waters. *Atmospheric Environment* (1967) 14: 1013-1016.
- Slinn, W. (1977) Some approximations for the wet and dry removal of particles and gases from the atmosphere. *Water, Air, and Soil Pollution* 7: 513-543.
- Slinn, W. (1982a) Predictions for particle deposition to vegetative canopies. *Atmospheric Environment* (1967) 16: 1785-1794.
- Stier, P., and Coauthors (2005) The aerosol-climate model ECHAM5-HAM. *Atmospheric Chemistry and Physics* 5: 1125-1156.
- Stone, B. M., and H. T. Shen (2002) Hydraulic resistance of flow in channels with cylindrical roughness. *Journal of Hydraulic Engineering* 128: 500-506.
- Stull, R. B. (1988) An introduction to boundary layer meteorology. Vol. 13, Springer.
- Tanaka, T. Y., and M. Chiba (2006) A numerical study of the contributions of dust source regions to the global dust budget. *Global and Planetary Change* 52: 88-104.
- Tegen, I. (2003) Modeling the mineral dust aerosol cycle in the climate system. *Quaternary Science Reviews* 22: 1821-1834.
- Thom (1967) The exchange of momentum, mass, and heat between an artificial leaf and the airflow in a wind-tunnel: 44-55.
- Thom, A. (1972a) Momentum, mass and heat exchange of vegetation. *Quarterly Journal of the Royal Meteorological Society* 98: 124-134.
- Thom, a. S. (1971) Momentum absorption by vegetation. *Quarterly Journal of the Royal Meteorological Society* 97: 414-428.
- THOM, A. S. (1972b) Momentum, mass and heat exchange of vegetation: 124-134.
- Thom, R. (1975) Structural stability and morphogenesis, 1975. Trans. by D. Fowler. Reading, Mass.: Benjamin.
- Uematsu, M., and Coauthors (2010) Atmospheric transport and deposition of anthropogenic substances from the Asia to the East China Sea. *Marine Chemistry* 120: 108-115.
- Uno, I. (2003) Regional chemical weather forecasting system CFORS: Model descriptions and analysis of surface observations at Japanese island stations during the ACE-Asia experiment. *Journal of Geophysical Research* 108: 8668.
- Uno, I., and Coauthors (2006) Dust model intercomparison (DMIP) study over Asia: Overview. *Journal of Geophysical Research* 111: D12213.
- Volkov, K. N. (2004) Influence of Turbulence on the Deposition of Particles from a Gas-Dispersed Flow on the Wall. *Journal of Engineering Physics and Thermophysics* 77: 894-903.
- Walcek, C. J., and G. R. Taylor (1986) A theoretical method for computing vertical distributions of acidity and sulfate production within cumulus clouds. *Journal of the Atmospheric Sciences* 43: 339-355.
- Walter, B., C. Gromke, and M. Lehning (2012) Shear-stress partitioning in live plant canopies and modifications to Raupach's model. *Boundary-Layer Meteorology* 144: 217-241.
- Wang, Q., and K. Squires (1996) Large eddy simulation of particle deposition in a vertical turbulent channel flow. *International Journal of Multiphase Flow*.
- Waraghai, A., and G. Gravenhorst (1989) Dry Deposition of Atmospheric Particles to an Old Spruce Stand. *Mechanisms and Effects of Pollutant-Transfer into Forests*, Springer, 77-86.
- Welty, J. R., C. E. Wicks, G. Rorrer, and R. E. Wilson (2009) Fundamentals of momentum, heat, and mass transfer. John Wiley & Sons.
- Wesely, M. L., and B. B. Hicks (2000) A review of the current status of knowledge on dry deposition 34.
- Wesely, M. L., D. R. Cook, and R. L. Hart (1985) Sulfur Dry Deposition Over Grass. *JOURNAL OF GEOPHYSICAL RESEARCH* 90: 2131-2143.

## References

---

- Wiman, B. L. B., and G. I. Ågren (1985) Aerosol depletion and deposition in forests—A model analysis. *Atmospheric Environment* (1967) 19: 335-347.
- Wooding, R., E. Bradley, and J. Marshall (1973) Drag due to regular arrays of roughness elements of varying geometry. *Boundary-Layer Meteorology* 5: 285-308.
- Yang, Y., and Y. Shao (2008) Numerical simulations of flow and pollution dispersion in urban atmospheric boundary layers. *Environmental Modelling & Software* 23: 906-921.
- Zender, C. S. (2003) Mineral Dust Entrainment and Deposition (DEAD) model: Description and 1990s dust climatology. *Journal of Geophysical Research* 108: 4416.
- Zhang, J., and A. Li (2008) CFD simulation of particle deposition in a horizontal turbulent duct flow. *Chemical Engineering Research and Design* 86: 95-106.
- Zhang, L., and Z. He (2013) Development of a parameterization scheme for calculating dry deposition velocity of fine, coarse and giant particles. *Atmospheric Chemistry and Physics Discussions* 13: 31289-31310.
- Zhang, L., S. Gong, J. Padro, and L. Barrie (2001) A size-segregated particle dry deposition scheme for an atmospheric aerosol module. *Atmospheric Environment* 35: 549-560.

## List of important symbols

$A$	Sheltering area of the wake
$A_f$	Frontal area of all elements on a surface, $A_f = nbh$
$A_s$	Total horizontal projection area of elements on a surface, $A_s = nb^2$
$b$	Width and length of roughness elements
$c$	Constant in chapter 3, in the expression of drag partition theory
$c_d$	Friction coefficient
$C$	Concentration of particle
$C_d$	Drag coefficient
$C_c$	Cunningham correction factor
$C_s$	Drag coefficient for the underlying surface
$C_r$	Drag coefficient for the roughness element
$c_w$	Ratio of $(z_w - d)/(h - d)$
$D$	Zero-plane displacement
$d_c$	Collector diameter
$d_L$	Diameter of larger collectors
$d_p$	Diameters of particles;
$d_S$	Diameter of smaller collectors
$E_b$	Collection efficient of Brownian diffusion
$E_{im}$	Collection efficient of impaction
$E_{in}$	Collection efficient of interception
$F$	Total momentum flux (in Chapter 3); Particle flux (in Chapter 4 and 5)

## List of symbols

---

$F_s$	Momentum flux to the roughness element
$F_r$	Momentum flux to the underlying surface
$h$	Height of roughness element.
$l$	Distance occupied by each element; length from the front of an element to the front of adjacent element.
$l_w$	Reattachment length, length of the back vortex behind an element.
$L_w$	Length of the wake, for a full wake, $L_w = l_w + b$ ; for a half wake, $L_w = l_w$ ;
$N$	Number of elements on a rough surface
$r_a$	Resistance of aerodynamic layer to the deposition flux
$r_b$	Resistance of roughness layer to the deposition flux
$r_{bh}$	$r_{bh} = b/h$
$r_r$	Ratio of $\tau_r$ to $\tau$
$r_s$	Ratio of $\tau_s$ to $\tau$
$R$	Efficiency of rebound.
$R_C$	Non-dimensional Resistance to momentum flux in canyon layer.
$R_r$	Non-dimensional Resistance to vertical momentum flux due to the roughness element.
$R_s$	Non-dimensional Resistance to vertical momentum flux due to the underlying surface.
$S$	Total area of a rough surface
$S_c$	Schmidt number.
$S_t$	Stokes number.
$u$	Free stream velocity.
$u_h$	Velocity at the top of the roughness element
$u_{ha}$	Threshold velocity at the top of the roughness element
$u_r$	Reference velocity
$u_{zw}$	Velocity at the top of roughness layer
$u^*$	Friction velocity
$v_d$	Deposition velocity
$v_g$	Gravitational settling velocity
$V$	Sheltering volume of the wake
$z$	Height from the underlying surface
$z_0$	Roughness length

$z_w$  Thickness of the roughness layer

**Greeks**

$\beta$   $\beta = C_s / C_r$

$\varepsilon$  Collection efficiency

$\kappa$  von Karman constant

$\lambda$  Roughness density; front area index

$\lambda_a$  Threshold roughness density.

$\lambda_m$  The Roughness density of the surface with the maximum drag.

$\mu$  Dynamic viscosity

$\rho$  The density of air

$\rho_p$  The density of particle

$\tau$  Shear stress

$\tau_s$  Shear stress on underlying surface

$\tau_r$  Shear stress on roughness element

$\Delta U^2$  Square of velocity gradient

$\Delta U_C^2$  Square of velocity gradient across the canyon layer

# Appendix

The table of deposition velocity, i.e.,  $v_d$ , measured in 3D simulation of particle laden flow. This table consists data acquired on 11 rough surfaces with different  $\lambda$ , under 6 different  $u_r$ , and for 15 different  $d_p$ .

$\lambda$	$d_p \mu\text{m}$	$u_r=1 \text{ ms}^{-1}$	$5 \text{ ms}^{-1}$	$10 \text{ ms}^{-1}$	$15 \text{ ms}^{-1}$	$20 \text{ ms}^{-1}$	$25 \text{ ms}^{-1}$
$\lambda = 0.5$	0.1	0.002401	0.005298	0.011273	0.016296	0.021574	0.023772
	0.8	0.002453	0.005366	0.01138	0.016428	0.021685	0.02384
	1.51	0.002599	0.00551	0.01158	0.016654	0.021887	0.023961
	2.22	0.002746	0.005659	0.011737	0.016874	0.022033	0.024027
	2.93	0.00297	0.005857	0.011905	0.016981	0.022014	0.023886
	3.64	0.003033	0.005982	0.012023	0.017008	0.021843	0.023585
	4.34	0.003045	0.006082	0.012161	0.016949	0.021631	0.023271
	5.05	0.00297	0.006147	0.012308	0.016905	0.021437	0.022984
	5.76	0.003211	0.006365	0.012464	0.016862	0.021344	0.022882
	6.46	0.003493	0.006634	0.012653	0.016839	0.021262	0.022808
$\lambda = 0.4$	7.17	0.003828	0.006951	0.012881	0.016895	0.021292	0.022881
	7.88	0.003986	0.007189	0.013175	0.017021	0.021372	0.02294
	8.59	0.004525	0.007654	0.013521	0.017222	0.021518	0.023075
	9.29	0.005031	0.008111	0.013845	0.017461	0.021692	0.02327
	10	0.005468	0.00849	0.014053	0.017616	0.021778	0.0234
	0.1	0.002668	0.005995	0.0126	0.017622	0.022876	0.024853
$\lambda = 0.4$	0.8	0.002712	0.006068	0.012718	0.017797	0.023068	0.025046
	1.51	0.00284	0.006221	0.01293	0.018086	0.023402	0.02539

	2.22	0.003022	0.00643	0.013137	0.018382	0.023684	0.025687
	2.93	0.003236	0.006666	0.013351	0.018607	0.02383	0.025797
	3.64	0.003372	0.006895	0.013558	0.01876	0.023811	0.02572
	4.34	0.003468	0.007101	0.013786	0.018823	0.023723	0.02557
	5.05	0.003571	0.007318	0.014021	0.018877	0.023638	0.025444
$\lambda =$	5.76	0.003878	0.007603	0.014237	0.018922	0.023631	0.025429
0.4	6.46	0.004223	0.007904	0.014464	0.019	0.023663	0.025446
	7.17	0.004563	0.008205	0.014724	0.019132	0.023777	0.025545
	7.88	0.004751	0.008444	0.01501	0.019306	0.023894	0.02561
	8.59	0.005215	0.008852	0.015329	0.019525	0.024053	0.025742
	9.29	0.005706	0.009315	0.015692	0.019822	0.024252	0.025913
	10	0.006139	0.009701	0.015962	0.020043	0.024392	0.026042
	0.1	0.00313	0.007288	0.014309	0.019456	0.02427	0.026222
	0.8	0.003174	0.007384	0.014475	0.019691	0.024553	0.026535
	1.51	0.003313	0.007554	0.01473	0.02008	0.02505	0.027084
	2.22	0.00354	0.007833	0.015056	0.020514	0.025522	0.0276
	2.93	0.003768	0.008135	0.015407	0.020953	0.025918	0.027977
	3.64	0.003971	0.008476	0.015764	0.021281	0.026089	0.028113
$\lambda =$	4.34	0.004126	0.008785	0.016099	0.021481	0.026153	0.028169
0.33	5.05	0.004348	0.00911	0.016406	0.021607	0.026164	0.028187
	5.76	0.004652	0.009438	0.016692	0.021722	0.026225	0.028262
	6.46	0.005029	0.009777	0.016969	0.021847	0.026311	0.02833
	7.17	0.005404	0.010113	0.017266	0.022029	0.026477	0.02848
	7.88	0.005728	0.010433	0.017577	0.022242	0.026633	0.028585
	8.59	0.006138	0.010795	0.017885	0.022495	0.026843	0.028758
	9.29	0.006602	0.01124	0.01825	0.022797	0.027038	0.028906
	10	0.006966	0.011588	0.018527	0.023037	0.027201	0.029045
	0.1	0.003324	0.008154	0.014776	0.019331	0.02338	0.025639
	0.8	0.00341	0.008292	0.014983	0.019594	0.023687	0.02597
$\lambda =$	1.51	0.003582	0.008495	0.015264	0.020012	0.024244	0.026621
0.3	2.22	0.00384	0.008829	0.015678	0.020557	0.02485	0.027282
	2.93	0.004085	0.009212	0.016153	0.021156	0.025403	0.027834
	3.64	0.004353	0.009651	0.016681	0.021653	0.025736	0.028087
	4.34	0.004553	0.010049	0.017159	0.021973	0.025889	0.028191

## Appendix

---

	5.05	0.004837	0.010445	0.017584	0.022162	0.025973	0.028253
	5.76	0.005136	0.010828	0.018005	0.022377	0.026093	0.028326
	6.46	0.005501	0.011199	0.018396	0.022604	0.026267	0.02843
$\lambda =$	7.17	0.005869	0.011554	0.018764	0.022848	0.026481	0.028589
0.3	7.88	0.006259	0.01194	0.019121	0.023068	0.026653	0.028738
	8.59	0.006696	0.012325	0.019434	0.023277	0.026844	0.028931
	9.29	0.007179	0.012779	0.019822	0.02357	0.027064	0.029115
	10	0.007518	0.013093	0.020099	0.023808	0.02726	0.029279
	0.1	0.003091	0.008002	0.014309	0.019276	0.023002	0.025331
	0.8	0.003188	0.008145	0.014549	0.019545	0.023322	0.025652
	1.51	0.003353	0.008364	0.01493	0.020075	0.023997	0.026364
	2.22	0.00353	0.008655	0.01545	0.020819	0.024855	0.027222
	2.93	0.003713	0.009071	0.016135	0.021729	0.02573	0.028025
	3.64	0.003927	0.009557	0.01689	0.022546	0.02638	0.028511
$\lambda =$	4.34	0.00414	0.010057	0.017602	0.023179	0.026806	0.028803
0.27	5.05	0.004444	0.010554	0.018251	0.023642	0.027114	0.029001
	5.76	0.004756	0.011041	0.01885	0.024047	0.027378	0.029185
	6.46	0.005176	0.011558	0.019399	0.024376	0.027571	0.029306
	7.17	0.005648	0.012091	0.019921	0.024703	0.027796	0.029501
	7.88	0.00619	0.012656	0.020419	0.024971	0.027958	0.029647
	8.59	0.006718	0.01317	0.020882	0.025244	0.028182	0.029861
	9.29	0.007231	0.013666	0.02131	0.025511	0.028372	0.030024
	10	0.007567	0.013993	0.021599	0.025727	0.02854	0.030172
	0.1	0.002578	0.007008	0.012821	0.018037	0.021913	0.024405
	0.8	0.002664	0.007132	0.013043	0.018282	0.022234	0.024744
	1.51	0.002775	0.007313	0.013425	0.018819	0.022967	0.02554
	2.22	0.002863	0.007575	0.014004	0.019723	0.024044	0.026648
	2.93	0.002976	0.007965	0.014789	0.020862	0.025244	0.027793
$\lambda =$	3.64	0.003152	0.008497	0.015748	0.022046	0.026337	0.028721
0.2	4.34	0.003415	0.009081	0.016679	0.023035	0.027143	0.029319
	5.05	0.003794	0.009751	0.017628	0.023911	0.027819	0.029807
	5.76	0.004219	0.010419	0.018504	0.02466	0.028342	0.030139
	6.46	0.004713	0.011099	0.019319	0.025283	0.02875	0.030383
	7.17	0.005256	0.011791	0.020072	0.025827	0.029097	0.030621
	7.88	0.005853	0.01249	0.020755	0.026255	0.029353	0.030822

$\lambda =$	8.59	0.006494	0.013194	0.021412	0.026645	0.029595	0.031026
0.2	9.29	0.007079	0.013788	0.021962	0.026975	0.029806	0.031171
	10	0.007476	0.014179	0.022319	0.027211	0.029957	0.031266
	0.1	0.002314	0.006366	0.012031	0.017548	0.021463	0.023766
	0.8	0.002371	0.006464	0.012216	0.017771	0.021774	0.024118
	1.51	0.002431	0.006601	0.012576	0.018288	0.022505	0.024917
	2.22	0.002436	0.006819	0.013163	0.019258	0.023677	0.026134
	2.93	0.002515	0.007195	0.01404	0.020584	0.025156	0.027562
	3.64	0.002689	0.007787	0.015185	0.022098	0.026657	0.028915
$\lambda =$	4.34	0.002974	0.00847	0.016357	0.023481	0.027902	0.029932
0.17	5.05	0.003354	0.009275	0.017605	0.024796	0.028977	0.03075
	5.76	0.003791	0.010086	0.018778	0.025943	0.029839	0.031339
	6.46	0.004336	0.010923	0.019877	0.026906	0.030535	0.031796
	7.17	0.004941	0.011775	0.020902	0.027742	0.031081	0.032127
	7.88	0.0056	0.012597	0.0218	0.028413	0.03151	0.032401
	8.59	0.00628	0.013432	0.022682	0.029002	0.031855	0.03261
	9.29	0.00693	0.014148	0.023411	0.029444	0.032139	0.032789
	10	0.007373	0.014634	0.023901	0.029737	0.032313	0.032883
	0.1	0.00218	0.005384	0.010751	0.016061	0.020393	0.022564
	0.8	0.002227	0.005477	0.010939	0.016264	0.02068	0.022884
	1.51	0.002252	0.005562	0.011231	0.016698	0.021337	0.023617
	2.22	0.002238	0.005729	0.011773	0.017602	0.022463	0.024772
	2.93	0.002302	0.006009	0.012552	0.01886	0.023993	0.026292
	3.64	0.002472	0.006502	0.013636	0.0204	0.025687	0.02787
$\lambda =$	4.34	0.002743	0.007089	0.014751	0.021863	0.027177	0.029175
0.13	5.05	0.003097	0.007814	0.015979	0.0233	0.028486	0.030223
	5.76	0.003528	0.008605	0.017205	0.024622	0.029573	0.031001
	6.46	0.004043	0.00941	0.018376	0.025768	0.030506	0.031645
	7.17	0.004621	0.010254	0.019444	0.026737	0.031196	0.032098
	7.88	0.005266	0.011067	0.020366	0.027499	0.031731	0.032464
	8.59	0.005991	0.011948	0.021289	0.028181	0.032137	0.03271
	9.29	0.006732	0.012732	0.02208	0.028693	0.032497	0.032953
	10	0.007243	0.013276	0.02261	0.029016	0.0327	0.033082
$\lambda=0.1$	0.1	0.002168	0.004285	0.008249	0.012037	0.015326	0.016767

## Appendix

---

	0.8	0.002202	0.004343	0.008377	0.012168	0.015517	0.016973
	1.51	0.002203	0.004391	0.008573	0.012445	0.015952	0.017465
	2.22	0.002163	0.004457	0.008902	0.013016	0.016679	0.018191
	2.93	0.002185	0.004623	0.009402	0.013839	0.017703	0.019225
	3.64	0.002303	0.004924	0.010105	0.014873	0.01888	0.020326
	4.34	0.002478	0.005311	0.010861	0.015917	0.019978	0.021322
$\lambda =$	5.05	0.00271	0.005765	0.011696	0.016959	0.021003	0.02217
0.1	5.76	0.002991	0.006291	0.012568	0.017989	0.021962	0.02296
	6.46	0.003355	0.006856	0.013451	0.019022	0.023053	0.023989
	7.17	0.003768	0.007506	0.014424	0.020239	0.024368	0.025317
	7.88	0.004319	0.008301	0.015606	0.021722	0.025988	0.026931
	8.59	0.005056	0.009405	0.017175	0.023528	0.027772	0.028594
	9.29	0.006145	0.010868	0.019048	0.025434	0.029557	0.030223
	10	0.006982	0.011988	0.020404	0.02673	0.030705	0.031269
	0.1	0.002024	0.002954	0.005173	0.007472	0.009884	0.011007
	0.8	0.002053	0.002979	0.005232	0.007519	0.009988	0.01113
	1.51	0.002066	0.00301	0.005338	0.007652	0.010234	0.011431
	2.22	0.002068	0.003034	0.005505	0.007949	0.010627	0.011799
	2.93	0.002079	0.003105	0.005731	0.008339	0.011131	0.012324
	3.64	0.002117	0.003199	0.006022	0.008838	0.011736	0.012894
$\lambda =$	4.34	0.002179	0.003343	0.006348	0.009382	0.012338	0.013454
0.033	5.05	0.002282	0.003514	0.006753	0.009974	0.013	0.014019
	5.76	0.002447	0.003775	0.007237	0.010634	0.01373	0.014693
	6.46	0.002657	0.004089	0.007806	0.011477	0.014877	0.015992
	7.17	0.002925	0.004543	0.008648	0.012881	0.016746	0.018125
	7.88	0.003387	0.005321	0.010072	0.015054	0.01943	0.02099
	8.59	0.004155	0.00666	0.012254	0.017963	0.022561	0.024068
	9.29	0.005559	0.008749	0.01513	0.021217	0.025727	0.027045
	10	0.006696	0.010395	0.017233	0.023441	0.027768	0.028956

## Acknowledgements

First of all, I would like to give my gratitude to my supervisor Prof. Dr. Yaping Shao, who helped me to choose this challenging research topic, provided me with an excellent working environment, and introduced me to leading scientists in our field. Without his support, I would not even believe that I could complete such tough task, and finished my study with significant achievements. I would also like to give my gratitude to my previous supervisor Prof. Dr. Xiaojing Zheng, who inspired, motivated and guided me to this research area. She is the one who has always believed in my ability, encouraged me to achieve a higher goal, and taught me how to work as a scientist.

This work is funded by Chinese Scholarship Council (CSC), German Research Foundation (DFG), and Graduate School of Geosciences (GSGS) of the University of Cologne. I am grateful for their financial support. And I heartily appreciate Prof. Dr. Xiaojing Zheng and Prof. Dr. Yaping Shao for their help on applying for fundings. I must thank our secretary Dagmar Janzen, as she had helped me with countless paper works. And also thank Dr. Karin Boessenkool for her help from GSGS.

I would like to thank Dr. Martina Klose, for her help on translating the abstract into german. I would like to thank Prof. Dr. Wanping Li, Prof. Dr. Yaping Shao, Prof. Dr. Michael Kerschgens, Sven Ulbrich, Dr. Paul Chi Yan Tsui, Dr. Andrian Chappel, Dr. Nicholas Webb, and Edmund Ilimoan Yamba, for proofreading my thesis and flourishing my work with indepth advises. I would like to thank Prof. Dr. Wanping Li, Prof. Dr. Yaping Shao, Dr. Shaofeng Liu, and Dr. Jan Schween for their time on discussion for my work.

I would like to thank all the rest of our working group and colleagues from my institute. Especially our 'coffee group', Sven Ulbrich, Dr. Martina Klose, Dr. Patrick Ludwig, Dr. Melanie Karremann, Fanni Dóra Kelemen, Dr. Sabine Lennartz-Sassinek, Stefanie Neske, Larisa Seregina, Roderick van der Linden, Robert Schuster, Rabea Haas, and Dr. Claudia Frick. The time that we shared together means a lot to me.

I would like to thank my parents, as their love is always my source of power. They know my deepest wishes, even when they were 10,000 kilometers away. They share with me the best they have and never ask for anything in return. I appreciate their support more than anything I ever had.

My special thanks are for my wife. During the last five years, we shared only one and half year under one roof. Thousands words can not express my apologies for her. Here, I dedicate this work to my wife, and wish her happy to see that it is finally completed.

## **Erklärung**

Ich versichere, dass ich die von mir vorgelegte Dissertation selbständig angefertigt, die benutzten Quellen und Hilfsmittel vollständig angegeben und die Stellen der Arbeit – einschließlich Tabellen, Karten und Abbildungen –, die anderen Werken im Wortlaut oder dem Sinn nach entnommen sind, in jedem Einzelfall als Entlehnung kenntlich gemacht habe; dass diese Dissertation noch keiner anderen Fakultät oder Universität zur Prüfung vorgelegen hat; dass sie - abgesehen von unten angegebenen Teilpublikationen - noch nicht veröffentlicht worden ist sowie, dass ich eine solche Veröffentlichung vor Abschluss des Promotionsverfahrens nicht vornehmen werde. Die Bestimmungen dieser Promotionsordnung sind mir bekannt. Die von mir vorgelegte Dissertation ist von Prof. Dr. Y. Shao betreut worden.

Köln, 2015

Zhuoqun Li

UNIVERSITÄT ZU KÖLN  
INSTITUT FÜR GEOPHYSIK UND METEOROLOGIE  
Zhuoqun Li

---



Pohlig Str.3  
50969 Köln  
Tel.: ++49 (0)221 470-6233  
Fax: ++49 (0)221 470-5198  
Email: zli010@uni-koeln.de

**Persönliche Daten:**

Vorname und Nachname: Zhuoqun Li  
Geburtsdatum: 21. Juni. 1983;  
Nationalität: China  
Familienstand: Verheiratet

**Schulische/Akademische Laufbahn:**

01. 2010 - Wissenschaftlicher Mitarbeiter (Stipendiat) an der *Universität zu Köln*, Institut für Geophysik und Meteorologie bei Prof. Dr. Yaping Shao
09. 2007 - 12. 2010 Studium Technische Mechanik an der *Lanzhou University*, School of civil engineering science and mechanics (kontinuierlichen Studium der Master und Doktor) bei Prof. Dr. Xiaojing Zheng
09. 2002 - 07. 2006 Studium Informationen Ingenieur an der *Huazhong University of Science and Technology*, Department of electronics and information engineering. Abschluss als Bachelor (B.ENG.)
09. 1996 - 07. 2002 Gymnasium, *Middle school attached to Huazhong University of Science and Technology*, Abschluss mit der Allgemeinen Hochschulreife.

**Aktuelle Publikationen**

- Zhuoqun Li, Zhang Jie, Huang Ning etc., A Review on Modeling and Monitoring of Dust Dry Deposition, *Journal of desert research*, 2011, V31(3): 639-648
- Zhuoqun Li, Xiaojing Zheng. Wind-tunnel Measurements of Lift-off Particles of Blown Sand Based on PIV, *ICSTDC (International Conference on Science and Technologies for Desertification Control)*, 2009

**Berufliche Tätigkeit**

- 01.2010 - 01.2013 Wissenschaftlicher Mitarbeiter an der Universität zu Köln

**Sprachkenntnisse:**

Englisch: Fließend, Deutsch: Mittel (CEF B1), Chinesisch: Muttersprache